

Radiator Stack PEM Fuel Cell Architecture, System Modeling and Flow Field Design

by


MICHAEL EDWARD PASTULA
B.Eng., University of Victoria, 1995

A Thesis Submitted in Partial Fulfillment of the
Requirements for the Degree of

MASTER OF APPLIED SCIENCE

in the Department of Mechanical Engineering

We accept this thesis as conforming
to the required standard



Dr. Z. Dong, Supervisor, (Department of Mechanical Engineering)



Dr. X. Li, Departmental Member, (Department of Mechanical Engineering)



Dr. M. Nahon, Departmental Member, (Department of Mechanical Engineering)



Dr. D. Harrington, External Examiner, (Department of Chemistry)

© MICHAEL EDWARD PASTULA, 1997
University of Victoria

All rights reserved. This thesis may not be reproduced in whole or in part, by
photocopy or other means, without the permission of the author.

Supervisor: Dr. Zuomin Dong

Abstract

High cost is currently a barrier to PEM fuel cell commercialization. Therefore, changes must be made to existing designs in terms of architecture, materials or manufacturing methods. Traditionally, PEM fuel cells are water-cooled. However, ultimately all of the fuel cell's waste heat needs to be rejected to the surrounding air. This thesis focuses on the feasibility of alternative direct air-cooled designs. Thus, combining the previously separate fuel cell and radiator devices. This leads to a larger stack design, but offers the benefits of increased system simplicity, and potentially improved reliability and lower cost. Air-cooled systems eliminate an intermediate cooling medium, have fewer components, and with effective integration, can use materials well-suited for heat rejection. Both ambient air and tandem, or dual, air systems were examined. Performance goals for the new Radiator Stack Architectures (RSA) developed by *Next-Generation Fuel Cells for Transportation* (NGFT) were based on the best existing PEM fuel cell technology, New Electric Car II (*NECARII*), jointly developed by Daimler Benz and Ballard Power Systems in 1995.

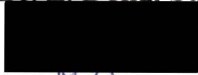
System modeling efforts examined the functional performance of six air-cooled architectures. Modeling and experiments concluded that low-grade heat produced by the fuel cell stacks described, could be rejected, with acceptable parasitic losses using a variable speed fan. The TERS97 design, a focus of much work, was found to have volumetric and gravimetric power densities 37 percent and 19 percent lower, respectively, than *NECARII*.

A method of rapidly prototyping gas delivery plates was also explored using CAD/CAM and screen printing or CNC machining as target manufacturing methods. The feasibility of the rapid prototyping method was proven through two programs, one which examined general flow field design, and another which generated various computer models for Ballard Power Systems' MK-5 stack design.

Examiners:



Dr. Z. Dong, Supervisor, (Department of Mechanical Engineering)



Dr. X. Li, Departmental Member, (Department of Mechanical Engineering)



Dr. M. Nahon, Departmental Member, (Department of Mechanical Engineering)



Dr. D. Harrington, External Examiner, (Department of Chemistry)

Table of Contents

| | |
|---|-----------|
| ABSTRACT | II |
| TABLE OF CONTENTS | V |
| LIST OF TABLES..... | VIII |
| LIST OF FIGURES..... | IX |
| NOMENCLATURE | XI |
| 1. INTRODUCTION | 1 |
| 1.1 INTRODUCTION TO PROTON EXCHANGE MEMBRANE FUEL CELLS | 2 |
| 1.2 PEM FUEL CELLS FOR TRANSPORTATION..... | 6 |
| 1.2.1 PEM Fuel Cells for Automobiles | 6 |
| 1.2.2 PEM Fuel Cell Advantages over Other Types of Fuel Cells..... | 6 |
| 1.2.3 PEM Fuel Cell Advantages over Internal Combustion Engines..... | 7 |
| 1.2.4 Future Challenges for PEM Fuel Cells | 8 |
| 1.3 REVIEW OF PREVIOUS WORK | 9 |
| 1.4 MOTIVATION FOR RADIATOR STACK ARCHITECTURE | 12 |
| 1.5 OBJECTIVE | 12 |
| 1.6 METHODOLOGY | 13 |
| 1.6.1 Evaluation of Air-Cooled Designs | 13 |
| 1.6.2 Flow Field Design..... | 15 |
| 1.7 RESEARCH CONTRIBUTIONS | 15 |
| 1.8 THESIS OUTLINE..... | 16 |
| 2. DEVELOPMENT OF RADIATOR STACK ARCHITECTURES..... | 17 |
| 2.1 DESIGN 1: TUBE BUNDLE HEAT EXCHANGER PEM FUEL CELL..... | 17 |
| 2.1.1 Possible Tube Cross-Sections | 20 |
| 2.1.2 Design Improvement..... | 21 |
| 2.2 DESIGN 2: AMBIENT AIR FLAT AND WAVEBOARD PANEL RADIATOR STACK DESIGNS | 22 |
| 2.2.1 Flat Panel Design | 22 |
| 2.2.2 Waveboard Design..... | 24 |
| 2.3 DESIGN 3: TANDEM AIR DESIGNS | 24 |
| 2.4 ALTERNATE FIN DESIGNS..... | 26 |
| 2.5 AMBIENT AIR VERSUS TANDEM AIR DESIGN EVALUATION | 28 |
| 2.5.1 Air Supply | 28 |
| 2.5.2 Air Humidification | 30 |
| 2.5.3 MEA Performance | 31 |
| 2.5.4 Heat Removal..... | 33 |
| 2.5.5 System Considerations | 33 |

| | |
|---|-----------|
| 2.5.6 Summary | 34 |
| 2.6 DESIGN 4: TRI-STREAM EXTERNALLY MANIFOLDED RSA DESIGN (TERS96) | 35 |
| 2.7 DESIGN 5: TRI-STREAM EXTERNALLY MANIFOLD RSA DESIGN (TERS97) | 38 |
| 2.7.1 TERS97 Prototype..... | 39 |
| 2.8 DESIGN 6: TRI-STREAM INTERNALLY MANIFOLDED RSA DESIGN | 39 |
| 2.9 ARCHITECTURE SUMMARY | 40 |
| 3. PERFORMANCE MODEL OF PEM FUEL CELLS | 42 |
| 3.1 STACK MODEL | 42 |
| 3.2 POLARIZATION CURVES | 43 |
| 3.2.1 Operating Temperature | 44 |
| 3.2.2 Tandem Air Polarization Curve..... | 44 |
| 3.2.3 Ambient Air Polarization Curve | 45 |
| 3.2.4 Summary | 45 |
| 3.2.5 Resistivity Modeling..... | 46 |
| 3.3 REACTANTS..... | 47 |
| 3.3.1 Reactant Air Stream..... | 47 |
| 3.3.2 Reactant Hydrogen Stream..... | 48 |
| 3.3.3 Air Properties Variation With Temperature | 49 |
| 3.4 HUMIDIFICATION | 49 |
| 3.5 COOLING REQUIREMENTS AND MECHANISMS | 51 |
| 3.6 COOLING PANELS | 55 |
| 3.6.1 Cooling Air Pressure Drop Analysis..... | 56 |
| 3.7 DISCHARGE AIR TEMPERATURE | 56 |
| 3.8 PARASITIC LOADS..... | 57 |
| 3.8.1 Air Compression | 58 |
| 3.8.2 Cooling Fan..... | 58 |
| 3.8.3 Humidification Water Pump | 58 |
| 3.8.4 Module Efficiency | 59 |
| 3.9 CALCULATION OF WEIGHT | 59 |
| 3.9.1 Materials of Construction | 60 |
| 4. PERFORMANCE MODELING SPECIFICS OF RADIATOR STACK DESIGNS..... | 61 |
| 4.1 TUBE BUNDLE HEAT EXCHANGER PEM FUEL CELL..... | 61 |
| 4.1.1 Tube Configurations | 61 |
| 4.1.2 Resistivity..... | 63 |
| 4.1.3 Heat Transfer..... | 64 |
| 4.1.4 Pressure Drop..... | 64 |
| 4.1.5 Fins | 65 |
| 4.2 COOLING PANEL ANALYSIS OF TRI-STREAM EXTERNAL MANIFOLD RSA DESIGN (TERS97)..... | 67 |
| 4.2.1 Cooling Panel Analysis..... | 67 |
| 4.2.2 Test Apparatus | 69 |
| 4.2.3 Heat Transfer..... | 70 |
| 4.2.4 Validation of Flow Conditions..... | 73 |
| 4.2.5 Pressure Drop..... | 75 |
| 4.2.6 Cooling Panel Temperature Gradients..... | 77 |
| 4.2.7 Surface Roughness..... | 79 |
| 4.3 SYSTEM ANALYSIS OF TRI-STREAM EXTERNAL MANIFOLD RSA DESIGN (TERS97) | 80 |
| 4.4 MODELING OF THE BALLARD - DAIMLER BENZ NECARII SYSTEM..... | 83 |
| 4.4.1 System Analysis..... | 84 |
| 4.5 SUMMARY OF POWER DENSITIES FOR DESIGNS..... | 86 |
| 4.5.1 Cooling System | 87 |

| | |
|---|------------|
| 4.5.2 Reactant Supply System | 87 |
| 4.5.3 Stack (Electro-Chemical Engine)..... | 88 |
| 4.5.4 Control and Drive Systems | 88 |
| 4.5.5 Miscellaneous | 89 |
| 4.5.6 System Power Densities | 89 |
| 4.5.7 Conclusions..... | 89 |
| 4.6 SOFTWARE IMPLEMENTATION OF THE PEM FUEL CELL PERFORMANCE MODEL..... | 90 |
| 4.6.1 Function Modules of the Program..... | 90 |
| 4.6.2 Program Structure Flowchart..... | 91 |
| 4.6.3 Comments on Program Use..... | 92 |
| 5. FLOW FIELD DESIGN FOR REACTANT DELIVERY PLATES..... | 93 |
| 5.1 INTRODUCTION TO FLOW FIELD DESIGN | 93 |
| 5.1.1 Screen Printing Manufacturing Technique..... | 93 |
| 5.2 FLOW FIELD PRELIMINARIES | 94 |
| 5.2.1 Mass Transfer Issues..... | 94 |
| 5.2.2 Water Management..... | 95 |
| 5.2.3 Water Removal Mechanisms..... | 96 |
| 5.3 FLOW FIELD MODEL FORMULATION | 97 |
| 5.3.1 Inputs | 97 |
| 5.3.2 Pressure Drop..... | 98 |
| 5.4 FLOW FIELD PLATE DESIGNS | 100 |
| 5.5 PRESSURE DROP VALIDATION..... | 102 |
| 5.5.1 Test Apparatus | 102 |
| 5.6 PRESSURE DROP RESULTS | 105 |
| 5.6.1 Hydrogen Flow Field Plate | 106 |
| 5.6.2 Air Flow Field Plate | 108 |
| 5.6.3 Summary | 109 |
| 5.7 DEVELOPMENT OF FLOW FIELD ALTERNATIVES | 112 |
| 6. RAPID PROTOTYPING OF HYDROGEN AND AIR DELIVERY PLATES..... | 115 |
| 6.1 MOTIVATION FOR RAPID PROTOTYPING | 115 |
| 6.2 COMPUTER-AIDED FLOW FIELD DESIGN | 116 |
| 6.2.1 Design Process..... | 116 |
| 6.2.2 Model Creation..... | 119 |
| 6.3 INTERFACE TO AUTOMATED STENCIL MAKING..... | 120 |
| 6.4 SUMMARY OF RAPID PROTOTYPING FOR FLOW FIELD DESIGN..... | 120 |
| 6.5 PROTOTYPE SOFTWARE DESIGN TOOL | 121 |
| 6.5.1 Input Variables | 121 |
| 6.5.2 Comments on Program Use..... | 122 |
| 6.5.3 Program Summary..... | 123 |
| 7. CONCLUDING REMARKS | 124 |
| 7.1 RECOMMENDATIONS FOR FUTURE WORK | 127 |

List of Tables

| | |
|--|-----|
| Table 1.1: Air-Cooled Design Goals | 14 |
| Table 3.1: Values Of Electrode Kinetic Parameters for Tandem Air Designs | 45 |
| Table 3.2: Values Of Electrode Kinetic Parameters for Ambient Air Designs | 45 |
| Table 3.3: Heat Capacities of Selected Mediums @ 300 K [35] | 48 |
| Table 4.1: Comparison of Two Design Extremes without Fins..... | 66 |
| Table 4.2: Comparison of Initial Design and Actual Fin Dimensions..... | 68 |
| Table 4.3: Cooling Panel Experimental and Initial Model Pressure Drop Results..... | 76 |
| Table 4.4: Cooling Summary | 87 |
| Table 4.5: Reactant Supply Summary | 88 |
| Table 4.6: Fuel Cell Stack Summary | 88 |
| Table 4.7: System Power Densities | 89 |
| Table 4.8: Program Routines and Their Function..... | 90 |
| Table 4.9: Program Sub-routines and Their Function | 91 |
| Table 5.1: Fuel Cell Operating Parameters..... | 101 |
| Table 5.2: Design Parameters for Ballard MK-5 and TERS97..... | 102 |
| Table 5.3: Flow Field Data for Pressure Drop Testing | 105 |
| Table 5.4: Pressure Drop Results Confirming Gas Cross-over | 110 |

List of Figures

| | |
|--|----|
| Figure 1.1: Typical Cross-Sectional View of a PEMFC..... | 3 |
| Figure 2.1: Tube Bundle Heat Exchanger Design [13]..... | 18 |
| Figure 2.2: Tube Cross-Sections..... | 19 |
| Figure 2.3: Top View of Tube Arrangement | 20 |
| Figure 2.4: Inner / Outer Electrode Tube..... | 20 |
| Figure 2.5: Design Improvement to Increase Voltage | 21 |
| Figure 2.6: Flat Panel Radiator Stack Architecture Sub-Stack [14] | 22 |
| Figure 2.7: Partial Cross Section of the Ambient RSA Design | 23 |
| Figure 2.8: Partial Cross Section of the Tandem Air Design | 25 |
| Figure 2.9: Possible Tandem Air Fin Design..... | 25 |
| Figure 2.10: New Fin Design..... | 26 |
| Figure 2.11: All Metal Fin Design..... | 27 |
| Figure 2.12: Utilizing Tandem Air Supply | 28 |
| Figure 2.13: Utilizing Low Pressure Reaction Air | 29 |
| Figure 2.14: Humidity Ratio versus Temperature for Oxidant Stream..... | 31 |
| Figure 2.15: Effect of Pressure on Performance for a PEM Fuel Cell..... | 32 |
| Figure 2.16: Adiabatic Discharge Temperature versus Pressure Ratio..... | 34 |
| Figure 2.17: Externally Manifolder RSA (TERS96) | 36 |
| Figure 2.18: Top View of Hexagonal TERS96 | 36 |
| Figure 2.19: Manifolding Concepts [8] | 38 |
| Figure 2.20: Tri-Stream External Manifolder RSA Design (TERS97)..... | 39 |
| Figure 2.21: Internally Manifolder Tri-Stream RSA Design | 40 |
| Figure 2.22: General Fuel Cell System Schematic for Tandem Air Designs | 41 |
| Figure 3.1: Resistance Modeling for RS Architectures | 47 |
| Figure 3.2: Water Saturation in Air versus Pressure (for various temperatures) | 51 |
| Figure 3.3: Thermodynamic Approach for Calculating Cooling Load..... | 53 |
| Figure 4.1: Standard Pitches for Shell and Tube Heat Exchangers | 62 |
| Figure 4.2: Tube Parameterization..... | 62 |
| Figure 4.3: Tube Resistivity Model | 63 |
| Figure 4.4: Parameterization of Cooling Panel..... | 68 |
| Figure 4.5: Schematic of Cooling Panel Test Apparatus..... | 69 |
| Figure 4.6: Temperature Measurement Locations in Relation to the Aluminum Block.... | 70 |

| | |
|---|-----|
| Figure 4.7: Comparison of Initially Predicted and Exper. Outlet Air Temperature | 72 |
| Figure 4.8: Plot of Nusselt Number (Exp.) versus Re (Model) | 73 |
| Figure 4.9: Comparison of Improved Model and Experimental Outlet Air Temperature | 74 |
| Figure 4.10: Nusselt Number versus Cooling Air Flow Rate..... | 75 |
| Figure 4.11: Cooling Panel Pressure Drop vs. Cooling Air Mass Flow | 77 |
| Figure 4.12: Cooling Panel Temperature Gradient for Rejecting 169.4 W | 78 |
| Figure 4.13: Average Temperature Difference (T_5-T_2) for Various Cooling Powers | 79 |
| Figure 4.14: Energy Flows as a Function of Current Density | 81 |
| Figure 4.15: Performance Of Ancillaries In TERS97..... | 82 |
| Figure 4.16: Energy Flows as a Function of Current Density | 84 |
| Figure 4.17: Performance Of Ancillaries In BD95 | 86 |
| Figure 4.18: System Modeling Flowchart | 91 |
| | |
| Figure 5.1: Modes of Water Transport in a PEM Fuel Cell..... | 95 |
| Figure 5.2: Flow Field Plate Cross-Section | 97 |
| Figure 5.3: Flow Field Designs for TERS97 Stack | 101 |
| Figure 5.4: Hydrogen Flow Field Plate..... | 103 |
| Figure 5.5: Schematic of Pressure Drop Testing Arrangement | 104 |
| Figure 5.6: Calibration Curve for Motorola MPX50DP..... | 105 |
| Figure 5.7: Hydrogen Flow Field Plate at 167 kPa _a | 106 |
| Figure 5.8: Hydrogen Flow Field Plate at 308 kPa _a | 107 |
| Figure 5.9: Air Flow Field Plate at 167 kPa _a | 108 |
| Figure 5.10: Air Flow Field Plate at 308 kPa _a | 108 |
| Figure 5.11: Effect of Clamping Pressure on Pressure Drop for Hydrogen Flow Field..... at 308 kPa _a and 3.52 SLPM | 111 |
| Figure 5.12: Second Generation Flow Field Designs | 112 |
| Figure 5.13: Waved Flow Field Concept..... | 113 |
| Figure 5.14: Concept of Changing Channel Width | 114 |
| Figure 5.15: Imparting Flow Obstacles | 114 |
| | |
| Figure 6.1: Sample Flow Field Plate Parameterization | 117 |
| Figure 6.2: Flow Field Design Methodology..... | 119 |
| Figure 6.3: Rapid Production of Stencils for Screen Printing | 121 |

Nomenclature

A - area (m^2)

a - constant

a^* - duct aspect ratio

b - Tafel slope, constant

C - channel

c - specific heat capacity ($\text{J}/(\text{kg K})$)

D - diameter (m)

E - voltage potential (V)

F - Faraday's Constant (96 485 C/mole)

f - Darcy friction factor

G - Gibb's Free Energy ($\text{J}/\text{mol K}$), mass flow velocity ($\text{kg}/(\text{m}^2\text{s})$)

H - enthalpy (J/kg)

h - convection heat transfer coefficient ($\text{W}/\text{m}^2\text{K}$)

I - current (A)

j - current density (A/cm^2)

K - ratio of specific heats (c_p/c_v), wall conduction parameter

k - conductive heat transfer coefficient (W/mK)

L - length (m)

M - molar mass (kg/kmol)

m - mass (kg), mass transport coefficient, mean

N - number of

n - mass transport coefficient, number of electrons in elementary reaction

Nu - Nusselt number

P - pressure (kPa), perimeter (m), power (W)

Pr - Prandtl number

Q - heat (J), volumetric flow rate (m^3/s)

R - resistance (Ω), rib

Ra - Raleigh number

r - radius (m)

\bar{R} - universal gas constant (8.314 J/mol/K)

Re - Reynolds number

s - distance (m)

sf - safety factor

T - temperature ($^{\circ}\text{C}$, K)

t - thickness (m)

u - velocity (m/s)

V - volume (m^3)

W - work (J),

w - wall, humidity ratio (kg water/kg gas)

X - distance (m)

x - molar fraction (mole/mole)

Z - correction factor

Greek Symbols

α - absorptivity

ε - average roughness height (m), emissivity

Δ - delta

λ - stoichiometry

η - overpotential (V), efficiency

ϕ - relative humidity

ψ - dimensionless bend loss coefficient

ρ - density (kg/m^3), resistivity ($\Omega \text{ m}$)

μ - absolute viscosity ($\text{kg}/(\text{m s})$)

ν - kinematic viscosity (m^2/s)

Subscripts

a - anode, air

act - activation

c - cathode, channel

cs - cross-section

d - diagonal direction

e - electrical, equivalent

f - fan

hyd - hydraulic

i - inner

jt - Joule-Thomson

L - longitudinal direction

m - mean

mem - membrane

module - device and electric drive

o - reference value

r - reversible

s - smooth

sat - saturation

T - total

t - transverse direction, tube

w - wall, width

Superscripts

. - time derivative

- - average

* - normalized

m, n - constant

Acknowledgments

This work has been made possible through funding from a collaboration between British Gas Investments Canada, the National Science and Engineering Research Council of Canada (NSERC), and Ballard Power Systems.

I would like to thank my supervisor, Dr. Zuomin Dong, for his consistent support over the course of this work. For their contributions to this thesis, I would also like to thank the members of the Radiator Stack Architecture research group which include Dr. Dong, Gary Wang, Dr. Simader, Ken Kratschmar, Lida Chang, Martin Perry, Patricia Crane, and Walter Merida. Many thanks to the remainder of the NGFT program for the great working environment.

Finally, appreciation to my family and Susan for encouragement.

Chapter 1

Introduction

An age of fuel cell dominance in some areas of energy conversion is likely to occur within the foreseeable future. First discovered in 1839 by Sir William R. Grove, fuel cells remained in hiding until the Gemini space missions [8]. This is where the fuel cell found its first true application.

A fuel cell is an electrochemical device which converts the chemical energy of a fuel directly into electrical energy with the aid of an oxidant. Many types of fuel cells exist, and it is customary to classify them by the electrolyte used. The common classifications, with the associated electrolyte, include: alkaline (normally KOH), phosphoric acid, molten carbonate (mixture of Li_2CO_3 and K_2CO_3), solid oxide (yttria-stabilized zirconia) and proton exchange membrane (PEM) (solid polymer such as Nafion[®]). Each type of fuel cell has a unique set of operating conditions that generally defines application suitability.

Fuel cells have been identified as energy conversion candidates for uses ranging from large-scale power plants to lap-top computers. Automotive transportation, a large transport sector with great energy requirements, is well-suited to PEM fuel cells. Currently, the internal combustion engine is employed for this application, using gasoline

and diesel as fuel. This contributes to the environmental problems of air pollution, ground level ozone, and production of greenhouse gases and toxic substances [61]. Fuel cells satisfy society's new objectives for better transportation technologies, specifically those with zero or ultra-low emissions, high efficiency, flexible fuels and quiet operation.

1.1 Introduction To Proton Exchange Membrane Fuel Cells

A proton exchange membrane fuel cell, or PEMFC uses hydrogen and oxygen (in air) as fuel and oxidant. Hydrogen fuel is not yet a common energy currency, but can be derived from hydrogen-containing fuels such as methanol, natural gas, or even water. Hydrogen is often used by the petrochemical industry. For terrestrial applications, the reacting oxygen is found in atmospheric air. The hydrogen and oxygen react by the following equation



Of all the types of fuel cells, PEM fuel cells are perhaps the most elegant in terms of system design and mode of operation. Figure 1.1 shows a typical cross-section of a PEM fuel cell. Current membranes are solid, hydrated sheets of a sulfonated fluoropolymer that are similar to Teflon[®]. To be used in a fuel cell, this membrane is sandwiched between two platinum impregnated porous electrodes which have been made hydrophobic by coating with an appropriate compound. This assembly is heat-pressed to form a single unit called a membrane-electrode assembly (MEA). Besides maintaining ionic charge neutrality, the electrolyte membrane prevents gas cross-over by physically containing each gas. When dry, the proton exchange membrane is usually 50 to 200 μm thick. If wet, it could easily be over 200 μm thick such as Nafion 117.

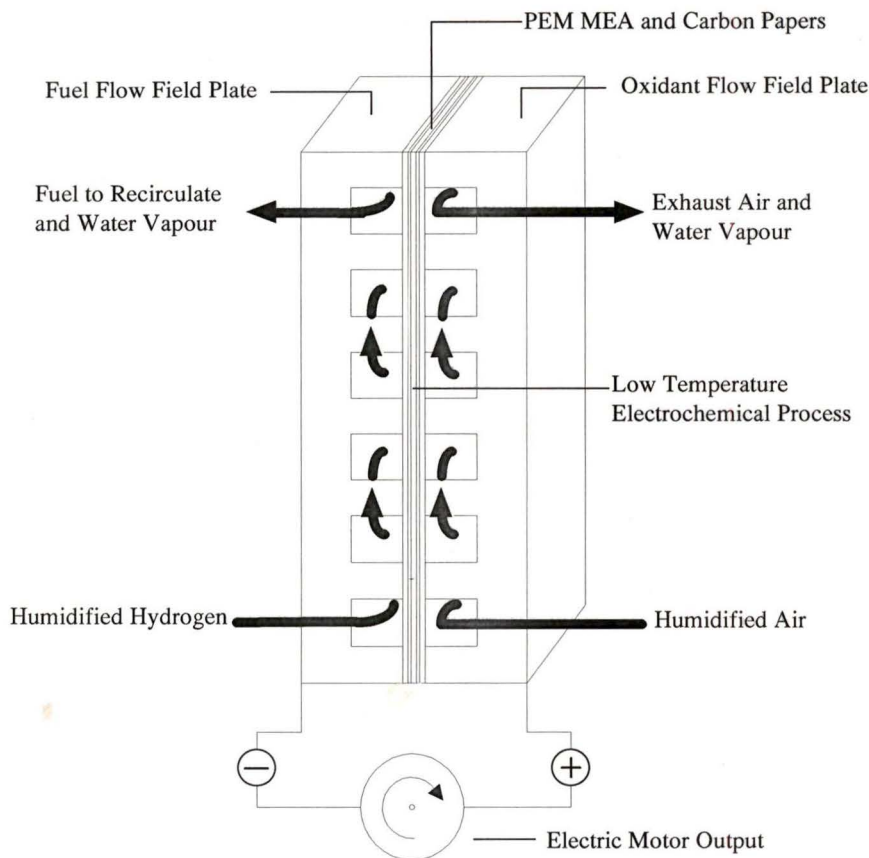


Figure 1.1: Typical Cross-Sectional View of a PEMFC

A cell is the basic building block of a fuel cell. Typical single cell hardware consists of a MEA, carbon papers and oxidant and hydrogen delivery plates. Additional stack components for a plate and frame arrangement include cooling plates, end plates, bus plates and a humidification section (when internal humidification is utilized). The MEAs are placed between reactant delivery plates. The plate material is generally graphite, graphite composite, or metal, and has embossed, machined or molded grooves which distribute gas over the electrode surface.

To maintain high membrane water content, required for high proton conductivity, both reactants are humidified. Hydrated hydrogen gas is fed into the channels of the fuel flow field plate. At the anode, the platinum catalyst aids in the electrochemical reaction



The protons migrate through the membrane to the cathode catalyst layer. At this location the protons react with the oxygen by the following reaction



Three types of reaction overpotentials lower fuel cell efficiency. First, the slow reaction at the oxygen electrode creates the need for an equilibrium shift to increase the exchange current. This shift, called the *activation overpotential*, causes a logarithmic drop in efficiency even at very small currents. With typical power loads, *ohmic overpotential* becomes important. This leads to an additional linear drop in voltage due to the electrical resistance of the membrane, electrodes, and graphite plates. Ultimately, the limiting power output of the stack is dictated by *mass transport limitations*. In the high current density regime, the necessary high inflow of reactants and removal of products demanded cannot be met.

1.1.1.1 History

The first PEM fuel cell used in an operational system was the General Electric 1 kW Gemini power plant built for the Gemini space missions. The performance and lifetime of these units was limited due to the polystyrene sulfonic acid membrane used at that time [8]. This fuel cell system provided auxiliary electric power, as well as potable water, for astronauts.

The original idea of using an organic cation exchange membrane polymers in fuel cells was conceived by William T. Grubs in 1959. Early work in this area was carried out by the General Electric Company. The earliest membranes were made by condensation of

phenosulfonic acid and formaldehyde. These membranes were brittle, cracked when dried, and rapidly hydrolyzed to sulfuric acid.

Perhaps the single most significant advancement in membrane technology was the replacement of these polystyrene sulfonate based membranes with perfluorinated membranes. This change led to substantially improved durability, longevity, and performance. The perfluorinated membranes, such as Nafion 117, were originally developed for the chlor-alkali industry. These polymers are generally unaffected by both strong acids and oxidants and are highly conductive to hydronium ions when hydrated. The new membrane had a three-fold effect on the performance in the late 1960s. This was attributed to minimal anion adsorption of the perfluorinated sulfonic acid anions on the platinum electrocatalyst and greatly enhanced oxygen reduction kinetics [8]. Secondly, the substitution of the hydrogen atoms by the highly electronegative fluorine significantly increases the conductivity of the electrolyte. Thirdly, the CF_2 groups, which substituted the CH_2 groups in the polymer acids, are not susceptible to electrochemical oxidation.

Until the last ten years, only small advances had been accomplished in PEM fuel cell performance. Rapid advances in performance have occurred only recently. These improvements, together with increasing environmental concerns with conventional power generating techniques, are responsible for sparking renewed interest. Ballard Power Systems, a world leader in PEM technology, has successfully integrated their system into city transit buses [44,48,49]. In conjunction with Daimler Benz of Germany, Ballard's stacks have been used in a mini-vans with the successful *NECAR* and *NECARI* projects [47]. Other PEM fuel cell development efforts are underway in Europe and Japan, each with significant government monetary support.

1.2 PEM Fuel Cells for Transportation

1.2.1 PEM Fuel Cells for Automobiles

The main motivation to make PEM fuel cell technology a useful source of motive power is the desire for a zero emission vehicle (ZEV). Ideally, fuel cells could be used to power transportation devices ranging from buses to automobiles, and submarines to surface ships. An automotive power plant is the target area for the Next-Generation Fuel Cell for Transportation (NGFT) group at the Institute for Integrated Energy Systems (IESVic), University of Victoria.

In order to commercialize PEM fuel cells, issues such as vehicle performance, vehicle technicalities, fuel availability, purchase price and operating costs must all be addressed. Performance issues include rapid start-up, fast response to changes in power demand, fuel economy, driving range and acceleration. Technicalities induced by the mobile platform include surviving prolonged vibration and temperatures below 0°C (normal melting point of water), as well as reliable operation under all environmental conditions. Currently, the internal combustion engine satisfies these operational requirements. Alternatives can only be justified if emissions can be greatly reduced and non-fossil primary energy sources can be used, at least partially, as an energy source. The scenario considered in this thesis is one in which high pressure gaseous hydrogen is used as fuel.

1.2.2 PEM Fuel Cell Advantages over Other Types of Fuel Cells

Of the various types of fuel cells, PEM fuel cells are the most suitable for automotive applications. At present, other types of fuel cells have drawbacks which are difficult to overcome. The advantages of using a solid acid electrolyte membrane are numerous. The membrane is simpler and more compact than other types of electrolyte, and low temperature operation is possible. PEM fuel cells are also able to sustain operation at high current densities. These attributes lead to a fast start capability and the ability to make a light, compact stack. The solid electrolyte removes any corrosive fluid spillage

hazard, and has low sensitivity to orientation. PEM fuel cells have a long list of advantages [8] which include: high efficiency, insensitivity to small differential pressures, no carbonate formation, long life, potable liquid product water, application versatility, wide range of suitable power outputs, simple design, and good manufacturability with potential for various component materials.

The ability of the PEM fuel cell to function at ambient temperature and pressure increases reliability, decreases complexity, and therefore reduces cost for certain applications. In addition, creep of the gelled electrolyte is usually negligible, and corrosion is minimal since pure water (rather than acid leach) is the only reaction product.

Competition is another reason for recent interest in PEM fuel cells. Fears of not joining in early with this technology, that has great potential, has pushed most automotive makers to develop their own fuel cell programs. The automotive industry, by bringing its mass production expertise to this issue, is helping to advance the technology.

1.2.3 PEM Fuel Cell Advantages over Internal Combustion Engines

Fuel cell vehicles share several advantageous attributes with battery-powered and internal combustion (IC) powered vehicles. Characteristics such as low or even zero tailpipe emissions, low noise, modularity and reasonable shape flexibility, liken to battery-powered vehicles. Fuel and air intakes, exhaust pipes, available waste heat for space heating, relatively high energy density and rapid refueling evoke comparisons with internal combustion systems.

The making of a PEM fuel cell stack is potentially much simpler than IC engines due to simpler geometry and fewer parts. PEM fuel cell power systems are generally more efficient than IC engines over the complete operating range. PEM fuel cell systems typically operate at 40 to 60 percent efficiency depending on the operating current density. This is significantly higher than IC engines which are usually less than 30

percent efficient, and most efficient near full-load. The contrary is true for fuel cells, which are most efficient at partial load. This characteristic of fuel cells makes them ideal for a typical transportation load cycle.

The conversion process in a fuel cell occurs at a much lower temperature than in a heat engine. Thus, NO_x formation, as well as hydrocarbon and CO emissions, are non-existent. Another advantage is no moving parts, thereby eliminating wear, wear-associated maintenance costs, and the need for lubricating oil.

1.2.4 Future Challenges for PEM Fuel Cells

Significant challenges lie ahead in the commercialization of PEM fuel cells. The biggest challenge is cost reduction. Partnership for a New Generation of Vehicles (PNGV) has set technical and cost targets. Performance targets are achievable, but the system cost target (excluding fuel processor or hydrogen storage system) of \$30/kW [60] is a great challenge considering current costs are at least 50-75 times higher [52]. The stack is the current focus for cost reduction, although the system, and its integration are also important. Major reductions in current stack costs are required for the three major components of the stack. These include gas delivery, or flow field plates, electro-catalyst, and membrane. Specific requirements of these components are:

- good mass production suitability for gas delivery plates,
- minimization of platinum (or the development of new catalysts) for electrodes, and
- inexpensive and environmentally friendly membranes that must satisfy a multitude of requirements.

Work is currently underway in all of these areas in many research institutions [8,14,22,43] around the world.

There are also important technical disadvantages:

- The inherent drawback of low temperature operation is low quality waste heat. Low quality heat requires a large cooling system.

- The major contaminate for PEM fuel cells is carbon monoxide (CO). Only a few parts per million (*ppm*) of CO can be tolerated with the platinum catalysis at 85°C. CO in the gas stream is preferentially adsorbed on the platinum catalyst surface and blocks access of the reactant to the catalyst sites.
- A complicated and critical issue of the membrane is the necessity to maintain a high water content. This sustains acceptable ion conductivity.

Despite being the ideal fuel cell fuel, difficulties with hydrogen make petroleum-based fuels worthy of consideration at least temporarily. The most notable problem is a lack of hydrogen infrastructure. This leads to high fuel costs. For hydrocarbon fuels, direct on-board reforming, along with gas scrubbing, is required to provide hydrogen. Compressed hydrogen leads to large storage tanks, and liquid hydrogen requires as-yet undeveloped technology. Of all the hydrocarbon fuels that are liquid at room temperature, methanol is the easiest to convert to hydrogen [60]. A liquid fuel gives the option of using some of the existing network of filling stations. Natural gas is an option, but gasoline is not as suitable due to high carbon content. An additional concern is on-board storage.

1.3 Review of Previous Work

Modeling of PEM fuel cells has grown over the last ten years. However, much of this work only looks at a single cell. System and stack modeling has been done to a lesser degree. No previous work on high performance air-cooled PEM fuel cells was found in literature.

At the University of Victoria, researcher of the Next-Generation Fuel Cell for Transportation (NGFT) program have modeled the PEM fuel cell system. Cownden [11] constructed a system performance model for Ballard Power Systems' Phase I bus which utilizes Ballard MK-5 stacks as a power plant. This model simulates the operation of all system components including the fuel cell, air compression, hydrogen supply and cooling subsystems. The output from the model includes gross and net system power, as well as

fuel cell and system efficiency. In addition to first law analysis, a second law exergy analysis was also performed. This model is specific to Ballard's Phase I bus and as such, empirical data and actual performance correlations were used directly in the model. This limits flexibility when examining a smaller air-cooled system.

Also within the NGFT program, Ronne and Podhorodeski [52] built a manufacturing cost model of a generic PEM fuel cell system. This was done to identify cost barriers and analyze parameter sensitivity. This model, and Cownden's work were integrated by Xue and Dong [79]. Using optimization techniques, a transportation fuel cell system was examined. Additionally, Pasquill and Nahon [32] undertook analysis to examine the feasibility of different PEMFC test platforms. The platforms examined include a car, van, runabout, and stationary dynamometer test bed. This study uncovered estimates for cost, mass and volume for various fuel cell sub-systems for different fuel cell power plant sizes.

At Canada's Royal Military College (RMC) in Kingston, Ontario, Amphlett *et al.* [2] modeled Ballard Power Systems' MK-4 stack design using a combination of mechanistic and empirical models followed by comparisons with experimental results. Next, Amphlett [1] examined Ballard's MK-5 stack in terms of transient response. This included an electrochemical, steady-state thermal and a transient thermal model. The electrochemical model is a semi-empirical model developed at RMC. Their thermal model, with the lack of radiation losses, is similar to the thermal management model found in Chapter 3 of this thesis.

Related to cell modeling, Nguyen and White [33] of the University of South Carolina presented a water and heat management model for PEM fuel cells. The purpose of the model was to evaluate various humidification designs. The model is thorough and accounts for water transport across the membrane by electro-osmosis and diffusion, and also latent heat of vaporization for water in the flow channels as an energy balance

consideration. This provides evidence that the anode stream, as well as the cathode stream, when using air, must be humidified. However the 10 *cm* channels are unrealistically short, and only show entrance effects for most practical designs. The channels are short, likely because of computational resources. Moreover, their model does not account for pressure drops in the flow channels, and has no system components. Springer, Zawodzinski and Gottesfeld [59] presented an isothermal, one-dimensional, steady state model for a complete polymer electrolyte fuel cell with a Nafion[®] membrane. This model is based on a single cell structure. Nguyen's and Springer's models are necessary when examining the intricacies of a single cell. While examining an entire system, these models are no longer essential, as an empirical cell formulation can be used.

A concise, empirical model for cell performance was developed by Kim [22] at Texas A&M University. Kim's model breaks the polarization curve into a lumped set of parameters for electrochemistry, ohmic losses and concentration losses. The model is used as a basis for polarization curves in this thesis. This approach is feasible when an empirical model of a single cell is desired. However, the influences of different operating pressures, temperatures and stoichiometries on the polarization curve must be considered independently from the model.

Cooling is important due to the characteristics of air-cooling. Anahara [8] provides a detailed discussion of cooling methods for phosphoric acid fuel cells. Anahara analyzes water, dielectric (oil) and air cooling methods for phosphoric acid fuel cells on a qualitative and historic basis. The discussion is historic in that some details of existing phosphoric designs are considered. The information was applied on a general basis in this thesis to examine various cooling techniques and mechanisms in PEM fuel cells.

1.4 Motivation for Radiator Stack Architecture

Traditionally, PEM fuel cells are cooled by circulating water. The water passes through the stack, increasing in temperature and internal energy. Then, a stainless steel radiator is used to reject the heat to the environment. Heat rejection is important due to narrow suitable operating parameters for high performance. The waste heat from PEMFC is low-grade heat as the temperature difference between the operating stack and environment may be as low as 40°C.

Air is known to be a poor coolant due to its thermal mass. However, ultimately all of the fuel cell's waste heat needs to be rejected to the surrounding air. Therefore, considering the overall system, it seems logical to complete the heat transfer in the stack. This reduces the number of heat transfer steps, and eliminates the intermediate cooling medium. Water-cooled designs require a large high-cost stainless steel radiator to minimize contamination of the water that is recycled to the stack. Due to the small temperature difference, and stainless steel's low thermal conductivity, the radiator must be larger than traditional automobile radiators made of copper or aluminum. With air-cooled designs, the large external radiator can be eliminated, and with effective integration, the stainless steel material may be replaced with ideal materials that are not considered "fuel cell friendly." These desirable materials include those with high thermal and electrical conductivity, and good manufacturability. The integration of radiator and power plant leads to a simpler and compact fuel cell system.

1.5 Objective

High cost is currently a barrier to PEM fuel cell commercialization. Therefore, changes must be made to existing designs in terms of architecture, materials or manufacturing methods. This thesis studies the feasibility and functional performance of six new air-cooled Radiator Stack Architectures as possible alternatives. A modeling tool is used to understand how different configurations and parameters change performance. A system approach is used for the analysis, with experimental work to verify key model findings.

Traditionally, PEM fuel cells are water-cooled. However, combining the previously separate fuel cell and radiator devices may improve functional performance through increased system simplicity, and potentially improved reliability and lower cost. Both ambient air and tandem, or dual, air systems are considered as possible solutions. Performance goals for the new Radiator Stack Architectures (RSA) were based on the best existing PEM fuel cell technology. The ultimate basis for comparison is system power density. This is a critical criterion for the integration of the fuel cell system into today's automobile.

The gas delivery plate for the PEM fuel cell stack is the second most important cost contributor next to the MEA. Thus, cost and manufacturing complexity reduction is critical to the future development of the technology. A method of rapid prototyping gas delivery plates to reduce testing and manufacturing costs was explored using CAD/CAM and screen printing or CNC machining as target manufacturing methods. A computer tool was developed to prove feasibility.

1.6 Methodology

1.6.1 Evaluation of Air-Cooled Designs

The air-cooled fuel cell designs are examined based on stack and system models. Parametric implementation allows for analysis with a variety of stack dimensions. As mentioned, the critical criterion for success is system gravimetric and volumetric power densities. The design goals are shown in Table 1.1.

Table 1.1: Air-Cooled Design Goals

| <i>Parameter</i> | <i>Goal</i> |
|----------------------------------|-------------|
| Gross Power Output | 64 kW |
| System Volumetric Power Density | 160 W/l |
| System Gravimetric Power Density | 150 W/kg |

These goals are based on the performance of the *NECARII* system. A gross output of 64 kW is large enough to power a compact automobile. The system power density targets are approximate values for the *NECARII* system. Currently, these targets are achieved at an unacceptable production cost.

System modeling was used to validate design operation, and allow for the correct sizing of cooling and mass flow components. Global optimization of the RSA designs on a performance and cost basis is future work to be carried out based upon these models to identify optimum parameters and improve results.

Thermal and water management, and high system efficiency are important to successful fuel cell operation. Cooling is a significant factor, and the cooling requirements and cooling mechanisms are examined in detail. The parasitic energy consumption of the complete fuel cell system is an important consideration. Although the efficiency of single cells is theoretically high, the additional energy required for ancillary equipment must be taken into account to evaluate overall effectiveness. The system performance model was implemented in FORTRAN codes.

The *NECARII* system is also modeled as a benchmark for comparison. Similar performance characteristics are used for common components such as the air compressor used to supply the oxidant gas stream. This allowed for a detailed comparison between the designs, and has shown where improvements can be made to aid air-cooled fuel cell system development.

1.6.2 Flow Field Design

With the new air-cooled stack designs, flow fields were required. Flow field design is critical to performance since it influences power distribution across the membrane surface and, if neglected, can lead to the inadequate catalyst utilization and hot spot formation with potential for leakage paths. Over the past ten years, flow field modeling has yielded insights that have led to significant advances in stack power density.

As complete computer modeling of a single cell is a demanding task, even with excellent computer facilities, the addition of experimental testing improves cost-effectiveness. A procedure and model are presented in this thesis, that can be used to rapidly prototype many different flow field patterns. This process can then be used to provide necessary design information for plate manufacturing using screen printing or CNC machining. A pressure drop model based on pipe flow was developed to aid the design process. Experimental validation was attempted to validate the model.

1.7 Research Contributions

This thesis focuses on the feasibility of alternative direct air-cooled designs. Thus, combining the previously separate fuel cell and radiator devices. Both ambient air and tandem, or dual, air systems were examined. System modeling efforts examined the functional performance of six new air-cooled architectures. Available literature on air-cooled fuel cells is not abundant, especially in the area of PEM fuel cells. The thesis provides direction on modeling this, as well as other types of PEM fuel cell systems. The advantages of using the air-cooled option are presented. On a system basis, air-cooled designs are simpler, but thermal management in stack design becomes a greater challenge. The complete understanding of the operation of a fuel cell is a highly complicated affair, both in terms of electrochemistry and mechanical engineering. This modeling effort undertaken by no means examines all mechanisms taking place in the fuel cell. However, the model focuses on a mass and energy balance approach, considering the stack and ancillary equipment.

The *NECARI* and its dual MK-7 power plant are evaluated on a system basis to set a benchmark for the air-cooled designs. A complete list of details and characteristics for the system is unavailable, so the system is analyzed using “reverse engineering” and assumptions. This approach uncovers some of the targets for the air-cooled designs.

A method of rapidly prototyping gas delivery plates is also explored using CAD/CAM and screen printing or CNC machining as target manufacturing methods. New, potentially patentable, concepts in channel designs are also shown. The RSA design team is currently investigating the feasibility of screen printing hydrogen and air delivery plates.

1.8 Thesis Outline

This thesis is presented in seven chapters. Chapter 1 focused on an introduction to proton exchange membrane fuel cells. The need for cleaner technologies, why PEM fuel cells are ideal candidates for automobiles and the advantages of the air-cooled architecture are discussed. Chapter 2 presents six new air-cooled stack designs. A discussion of ambient air fuel cells and tandem air designs is included, as well as the reasons for choosing tandem air systems for high power density automotive systems. Chapter 3 presents the model basis used to evaluate the designs. Chapter 4 presents some modeling specifics, and test results for two air-cooled designs. A summary of system power densities is included for the designs presented.

Chapters 5 and 6 are focused on flow field design and the rapid prototyping of the design and manufacturing of reactant delivery plates. Chapter 5 presents flow field preliminaries and the pressure drop model used for the design process. Pressure drop test results for the flow field designs for the final air-cooled design (TERS97) are also shown. Chapter 6 examines the motivation for rapid prototyping and explains an implementation created for Ballard Power Systems’ MK-5 design. Chapter 7 contains the concluding remarks.

Chapter 2

Development of Radiator Stack Architectures

This chapter focuses on design highlights of the Radiator Stack Architecture development. In September 1995, the first Radiator Stack Architecture (RSA) was developed with the objective to introduce air-cooled fuel cell designs that afforded better functional performance through improved system integration and less manufacturing efforts. Currently, the cost of the fuel cell stack is one of the critical factors preventing commercialization. To overcome this barrier, new designs must be suitable for mass production manufacturing methods. The guiding principles in development were design for manufacturing (DFM) and concurrent engineering with the goal of satisfying power density constraints with low manufacturing costs. The design process was approached from a system perspective, rather than solely examining the stack.

Approximately eighteen designs have been created by the RSA group. The development and understanding of the fuel cell was a learning process. This may be evident in the improvement of the designs presented chronologically.

2.1 Design 1: Tube Bundle Heat Exchanger PEM Fuel Cell

The Tube Bundle Heat Exchanger design is similar in architecture to a shell and tube heat exchanger. In this heat exchanger, some of the internal energy of the hot fluid is passed through conductive metal tube walls to increase the internal energy of the cold fluid. In

this similar fuel cell design, the hot and cold fluids are replaced with hydrogen and air. The tube walls that initially facilitated the conduction of heat, are now made of membrane electrode assemblies (MEAs). Each tube is protected with porous graphite on inner and outer surfaces which act as cathode and anode electrodes. In traditional plate and frame fuel cell designs, a cell consists of two sculpted bipolar plates separated by a proton exchange membrane. With the tube bundle design, a cell consists of several tubes. From a current perspective, this is likened to arranging cells in a parallel arrangement. Each tube helps supply a common voltage and contributes to the total current. A representation of the design is shown in Figure 2.1.

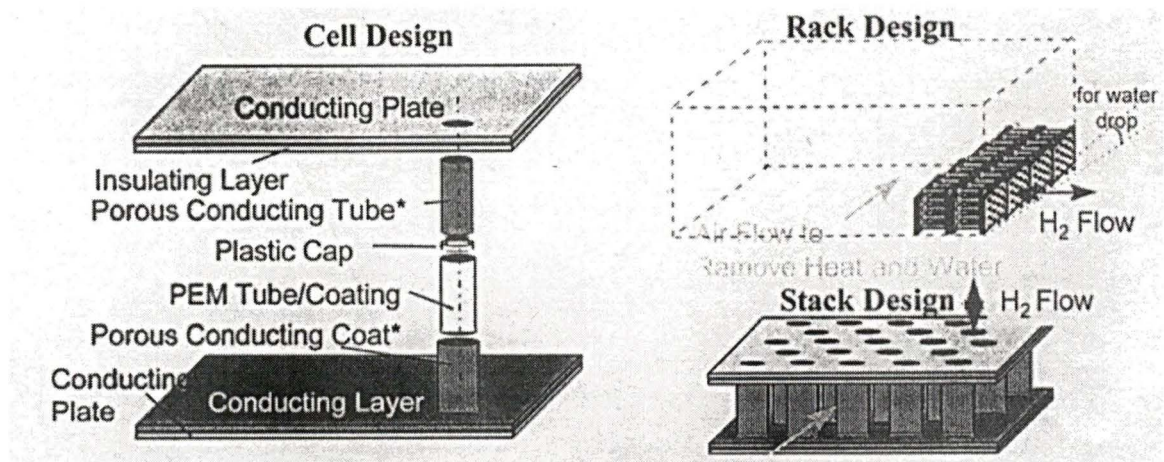


Figure 2.1: Tube Bundle Heat Exchanger Design [13]

The initial design invention memo[13] outlined a manufacturing process to produce the required tube cross section shown in Figure 2.2(a).

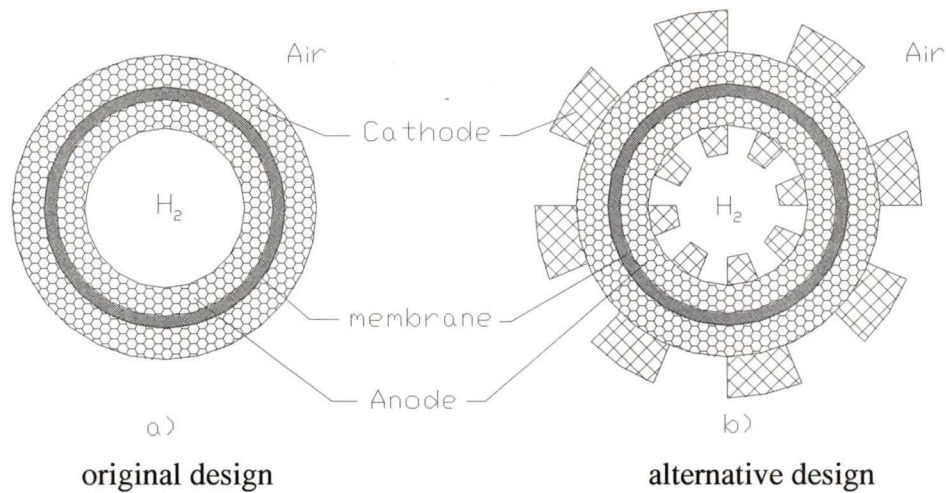


Figure 2.2: Tube Cross-Sections

The centre of the tube contains the cylindrical shell MEA. Porous graphite cylinders surround the MEA on both the inner and outer walls, and allow for: diffusion of reactants to the MEA, structural strength, current conduction, and MEA protection. The design requirements for the porous graphite are high porosity and good electrical conductivity. The high porosity is required to evenly distribute reactants to the MEA. High conductivity is required in terms of low bulk resistivity, and also low contact resistances at interfaces to minimize ohmic power losses.

With the stack design, low pressure ambient air is used as oxidant and coolant. The air is propelled over the tube bundles by a fan. The tubes are arranged in a manner to optimize heat transfer, while still maintaining an acceptable pressure drop. From a geometry point of view, for a fixed horizontal area, the number of tubes is proportional to $1/D_o^2$ (tube spacing changing accordingly), where D_o is the outer tube diameter. The active area is proportional to the tube diameter (at membrane) and the number of tubes. Thus, from a current perspective, it is desirable to have a large number of very small diameter tubes. However, this leads to manufacturing difficulties due to its physical size, and high fan power requirements due to high pressure drop. A possible tube arrangement is shown in Figure 2.3

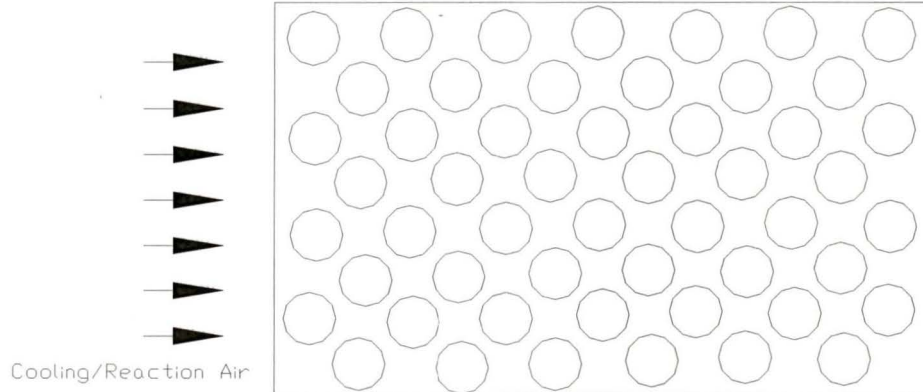


Figure 2.3: Top View of Tube Arrangement

Shell and tube heat exchangers are a mature technology. In heat exchangers as well as PEM fuel cells, heat exchange is paramount for successful operation. Thus, due to similarities in the designs, existing knowledge of the shell and tube heat exchangers was exploited.

2.1.1 Possible Tube Cross-Sections

The tube design, as shown in Figure 2.2 (a), offers manufacturing ease, but has inherently high ohmic power losses due to long thin electrodes and use of double edge collection. Current is conducted *along* the anodes and cathodes through relatively long current paths. Figure 2.2 (b) shows a different tube cross section that offers an increased electrode current carrying area. This decreases the overall tube resistance, and thus, power losses. Improved structural integrity is another advantage of the modified design. The inner and outer electrodes would appear as follows

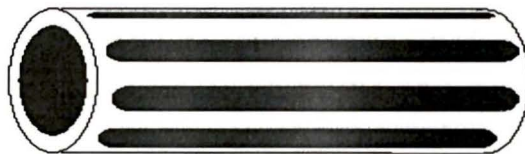


Figure 2.4: Inner / Outer Electrode Tube

Figure 2.4 depicts a cylindrical graphite tube with machined slots that allow reactant gas access to the MEA. Manufacturing of these electrodes is not as simple as previously outlined. Another option to keep the previous design, is to increase the conductivity of the electrode material. This could be done by impregnated the graphite electrode material with a highly conductive material. However, an acceptable material with good corrosion resistance, high thermal and electrically conductivity, and structural integrity, has yet to be found.

2.1.2 Design Improvement

At a selected current density, fuel cells deliver a characteristic voltage defined by a polarization curve. In automotive fuel cell applications, a power conditioning system is used to transform the raw electrical output into an acceptable input for the electric motor and ancillary equipment. However, even power conditioning systems have minimum, or maximum, input requirements for current or voltage. Thus, stack designs must meet these requirements. With the architecture presented, it is inseparably a high current, low voltage design. Figure 2.5 shows a method of increasing voltage by incorporating two or more sets of active areas in series. Thus, the total output voltage is increased accordingly. This modification adds manufacturing and sealing complexity.

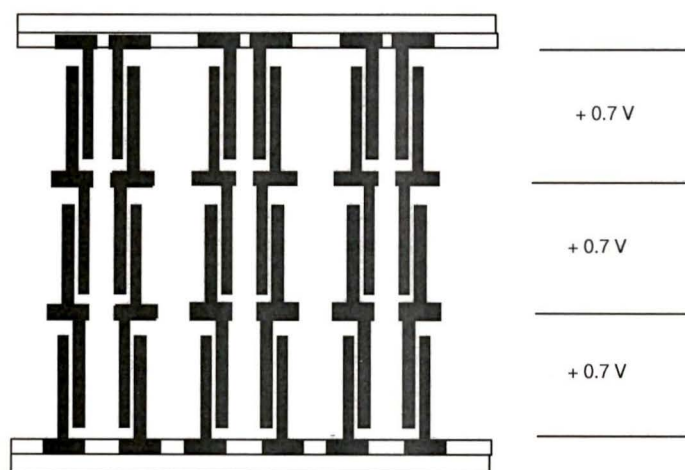


Figure 2.5: Design Improvement to Increase Voltage

2.2 Design 2: Ambient Air Flat and Waveboard Panel Radiator Stack Designs

2.2.1 Flat Panel Design

In December 1995, a new design was introduced. The tubes in the tube bundle design, were replaced with new panel elements. The build-up of current and voltage remained the same. These panel elements were considered radiator elements, hence the term radiator stack. A representation of an assembled sub-stack is shown in Figure 2.6. These elements are assembled in series to form a stack.

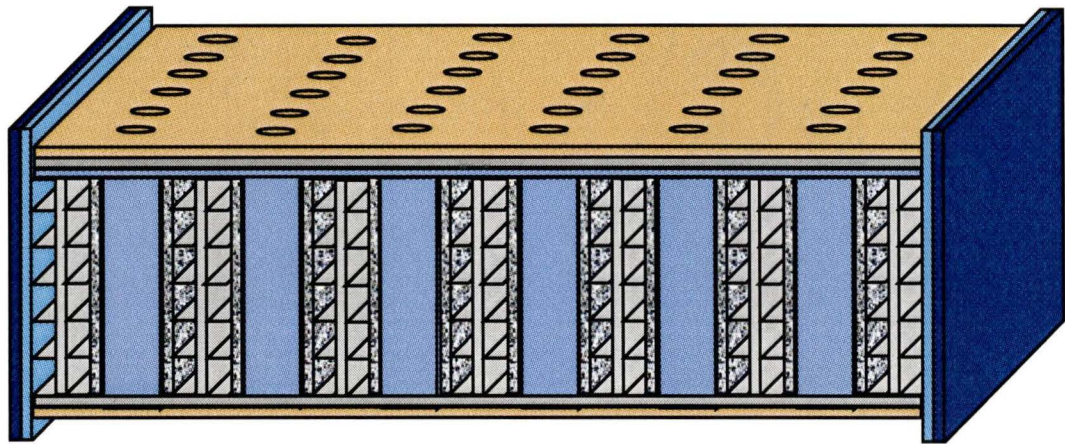


Figure 2.6: Flat Panel Radiator Stack Architecture Sub-Stack [14]

A detailed partial cross section of a sub-stack is shown in Figure 2.7.

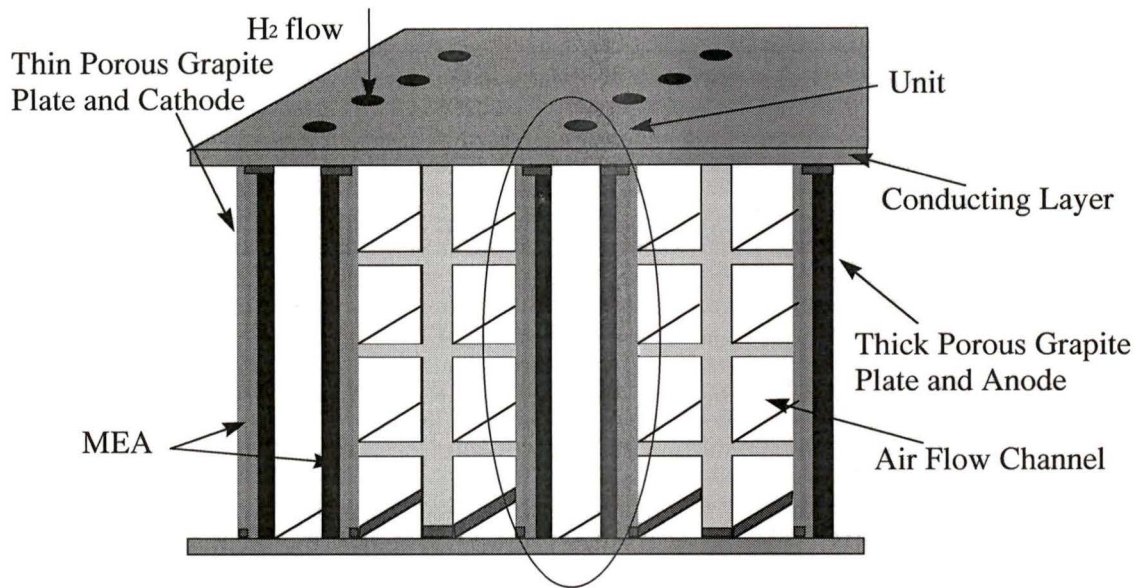


Figure 2.7: Partial Cross Section of the Ambient RSA Design

As with the Tube Bundle design, low pressure air is used as oxidant and coolant. The mass flow is set by the cooling requirements, which leads to high oxidant stoichiometry. Normally, the operating current density and desired stoichiometry, set the air mass flow rate.

The conducting layer provides electrical contact to adjacent cells, and defines the extremities of the sub-stack. Contained within these conducting layers are the units. In the vertical direction (Figure 2.7), units can be broken into an active height that contain the MEA, and a non-active height required for electrical insulation, sealing and manufacturing allowances. Conductive cooling fins are located between radiator elements. Each cooling fin conducts current away from the thin porous graphite sheet on the each cathode of the units, and helps cool the sub-stack by heating low pressure air which is propelled through the available channels by a fan. A graphite sheet is in contact with the anode to collect current.

The sub-stack structural integrity is upheld by plastic cartridge elements (shown as “units” in Figure 2.7). Each cartridge is made of hard plastic, an electrical insulator, that

is able to tolerate fuel cell conditions. Each cartridge holds graphite rods in place, allows for MEA sealing against each membrane, and helps with electrical isolation of components and stack assembly.

2.2.2 Waveboard Design

The waveboard design is very similar to the flat plate design. The only significant change is that the panel profile now follows a wave. The benefit is an increase in active area for the same flat panel footprint. The waveboard shape can be specified by a sine wave. An amplitude equal to zero corresponds to the flat plate design. The main disadvantage of the waveboard design is added manufacturing complexity.

2.3 Design 3: Tandem Air Designs

Successful stack designs for automobiles must be capable of meeting power density requirements. With higher pressure reactants, improved polarization curves, and higher operating current densities are attainable.

The main difference with tandem air designs is the utilization of pressurized reactant air. The two designs presented are the Flat Panel Tandem and Waveboard Tandem Air Designs. Large volumetric flows of ambient cooling air are still present. Thus, two independent air streams are supplied to each stack. Figure 2.8 shows a representation of part of the cell cross-section. Large air channels are provided for the cooling air, while small channels are used for the pressurized reactant air. Hydrogen flows in the vertical directions as shown.

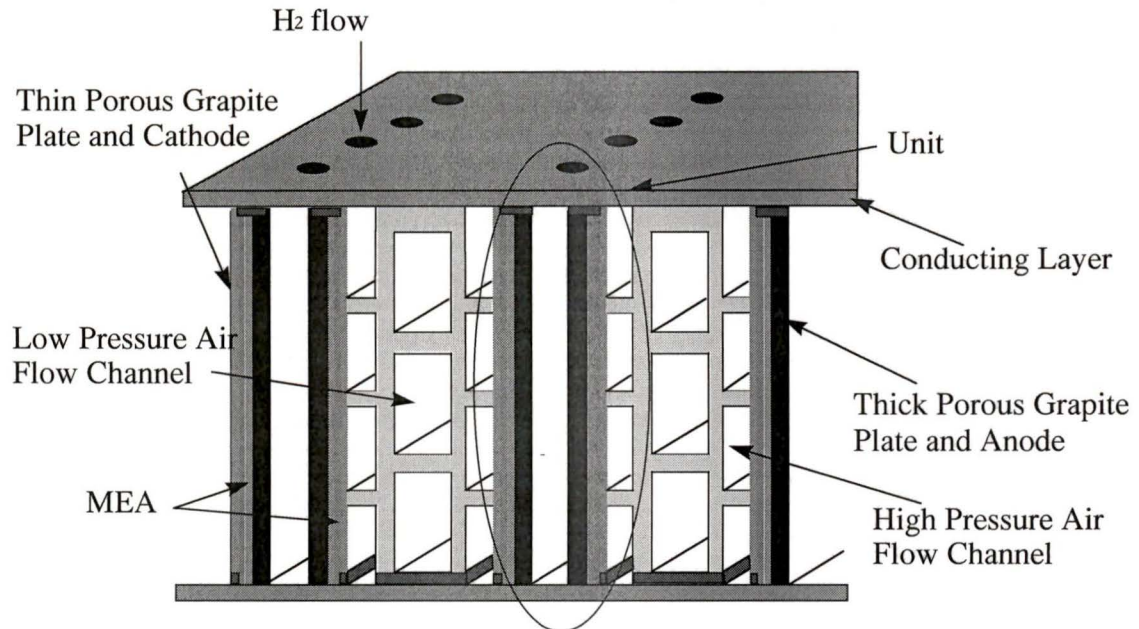


Figure 2.8: Partial Cross Section of the Tandem Air Design

The interior fin is now more complicated than with the ambient arrangements. Again, the waveboard design increases active area with added manufacturing complexity. The fin elements serve three purposes. They contain and direct high pressure and low pressure gases, and as with ambient designs, conduct heat and electricity, and lastly increase cooling area. A sample cross-section of a fin element may appear as follows

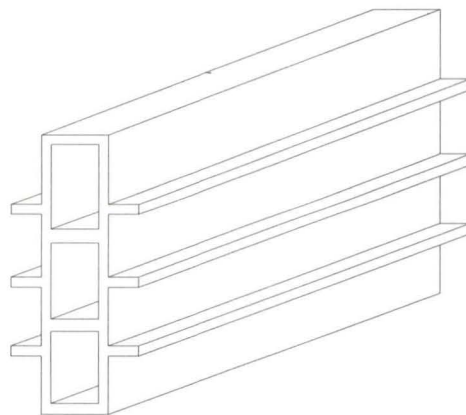


Figure 2.9: Possible Tandem Air Fin Design

The fin dimensions are key to each of its functions. Extrusion is the manufacturing method of choice for this component. This view does not show the manifolding which is required to independently supply the two air systems.

2.4 Alternate Fin Designs

Up to this point, the fin has had a small contact area with carbon paper on the cathode. Due to problems collecting current through such an area, and concerns about contact resistance, a design change was made. Manufacturing of the new component involves stamping a thin stainless steel sheet into a trapezoidal cross-section. This stamped sheet is then welded to a centre support sheet in the case of the ambient designs, or centre structure for the tandem air designs. This is shown in Figure 2.10.

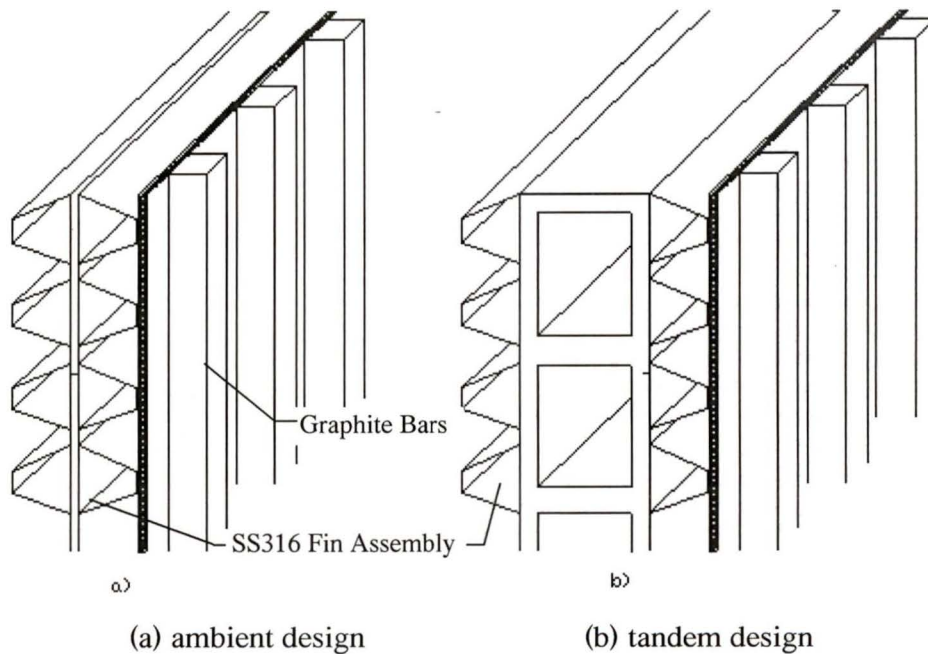


Figure 2.10: New Fin Design

The trapezoidal cross-section can then be optimized to find appropriate dimensions for the metal thickness and channel sizes. The issue of using stainless steel in the fuel cell, in terms of corrosion, was to be evaluated through single cell testing.

As metal was now used on the cathode, it is logical to introduce symmetry for the anode to reduce production. This modification also allowed for easier isolation of the two air streams. The proposed manufacturing material is sheet stainless steel (SS316L). Each fin is comprised of four sheets, two cut and stamped, and two flat, only cut with welded edges.

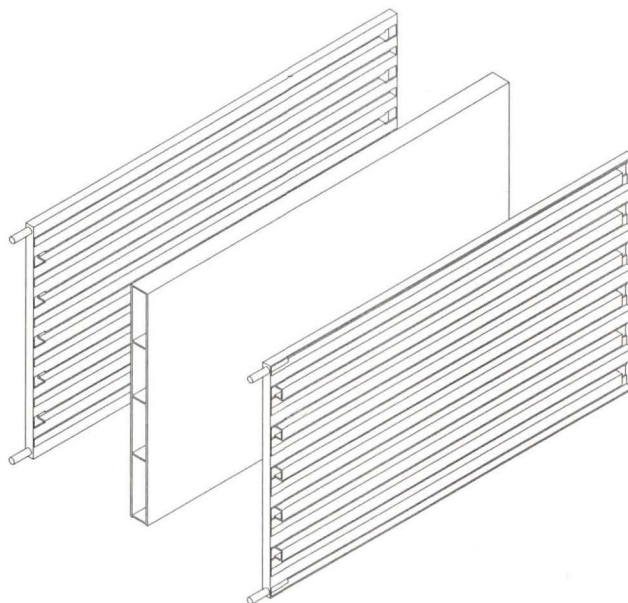


Figure 2.11: All Metal Fin Design

As shown in Figure 2.11, the high pressure reaction air follows the corrugations of a metal folded sheet over the active area. Flat sheets are formed into trays and act as backing plates, help with gas containment, and conduct current in the vertical direction. Conductive paste is used to fasten, and electrically connect the two components. Small notches are cut in the folded metal sheet to allow the reactant gas to pass from one channel to the next.

2.5 Ambient Air versus Tandem Air Design Evaluation

At this point, a focus was required for future work. The basic decision was whether to continue with the pressurized or ambient air designs. A brief comparison of the two alternatives, and the rationale for the judgment follow.

2.5.1 Air Supply

The two schematics presented in Figures 2.12 and 2.13 represent *two options for air supply* for the Radiator Stack Architectures when utilizing air cooling. Figure 2.12 shows a detailed tandem air system.

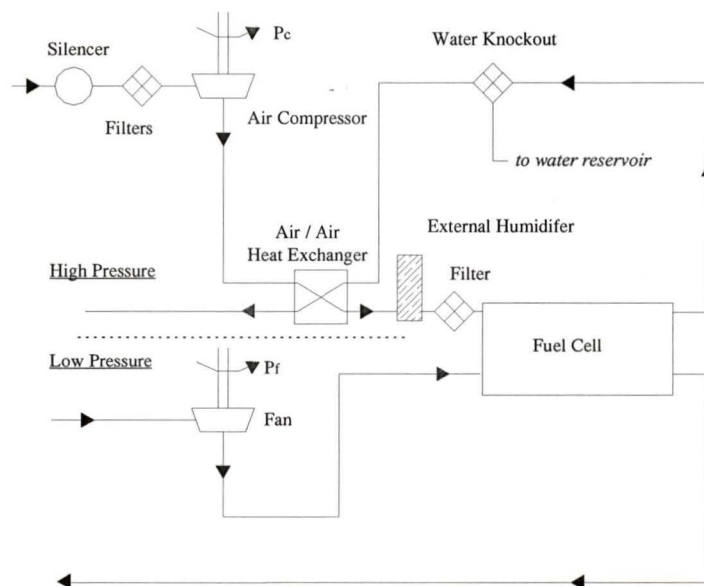


Figure 2.12: Utilizing Tandem Air Supply

It is important to note that for the high pressure system, a compressor is required in addition to a cooling fan. For the high pressure system, an energy recovery turbo-expander has not been included. This is due to the extra cost of the component, and the

size of the gains expected when utilizing significant pressure drops for water management. The high pressure system provides the humidified reaction air while the low pressure system satisfies cooling. Figure 2.13 shows the ambient air equivalent. In the figure, the humidified air is used for both the reaction and cooling.

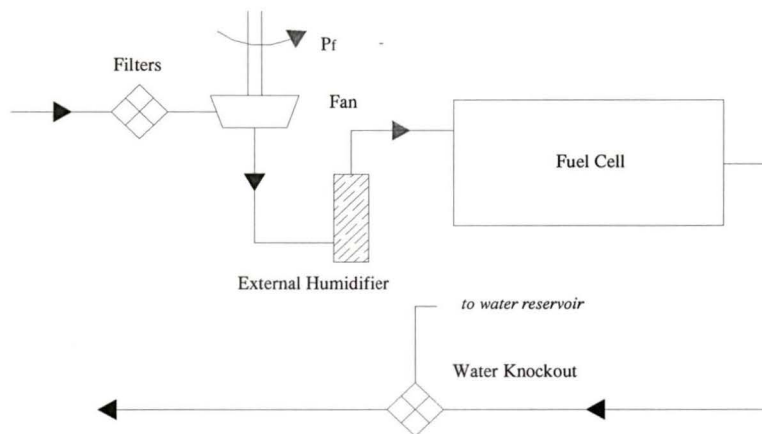


Figure 2.13: Utilizing Low Pressure Reaction Air

With the tandem air system, the amount of reaction air is set by the current density and stoichiometry, while the amount of cooling air is determined by the cooling conditions. In the ambient air case, the amount of air is determined solely by the cooling requirements, except at very low current densities. Due to air's low thermal mass, the reactant air must be supplied at a high stoichiometry to satisfy cooling requirements. As a result, issues to address for the ambient air designs are ensuring adequate humidification, and minimizing fan power load. For this design, it is beneficial to only humidify the reacting portion of the air. However, with the designs presented, this cannot be achieved without modifications.

For the tandem air designs, the large parasitic losses associated with the air compressor must be balanced with improved stack output. As air is the oxidant in both cases, a through-flow design is always necessary to prevent oxygen depletion. In general, this feed mode helps to reject heat, remove reaction products and inerts.

2.5.2 Air Humidification

A key to good performance is the maintenance of high water content in membranes. Usually membrane water content is maintained by humidifying both reactant streams. The water content in the gas streams is important. If the gas is too humid, water may condense at cool points in the stack and result in electrode flooding, and poor reactant diffusion. Conversely, if the air is too dry, the membrane electrode assemblies can dehydrate resulting in decreased proton conductivity and degraded performance, or cell failure.

The saturation pressure of water is only a function of temperature. Thus, for high pressure systems the ratio of water to air, on a mass basis, is much lower due to the more significant partial pressure of air (partial pressure of H₂O vapour constant assuming equal temperatures). The humidity ratio as a function of temperature for the oxidant stream is shown for the two systems in Figure 2.14 (generated using Equation 3.9).

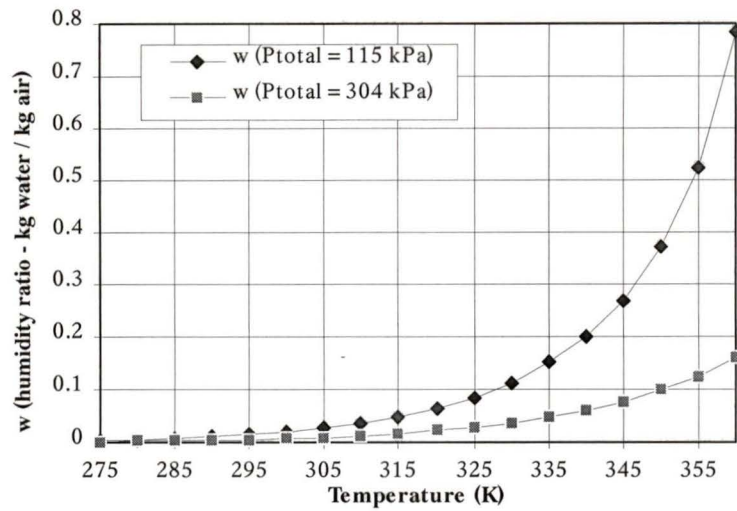


Figure 2.14: Humidity Ratio versus Temperature for Oxidant Stream

The low pressure system requires a greater amount of water for the air and hydrogen streams, and thus requires larger humidifiers.

2.5.3 MEA Performance

Temperature and pressure of operation have a significant effect on cell performance [26,56]. The following two polarization curves are representative of the expected results for an ambient air (115 kPa_a reactants) versus a pressurized system (304 kPa_a reactants). Improved performance occurs at high pressures due to improved reactant diffusion and higher reactant concentrations.

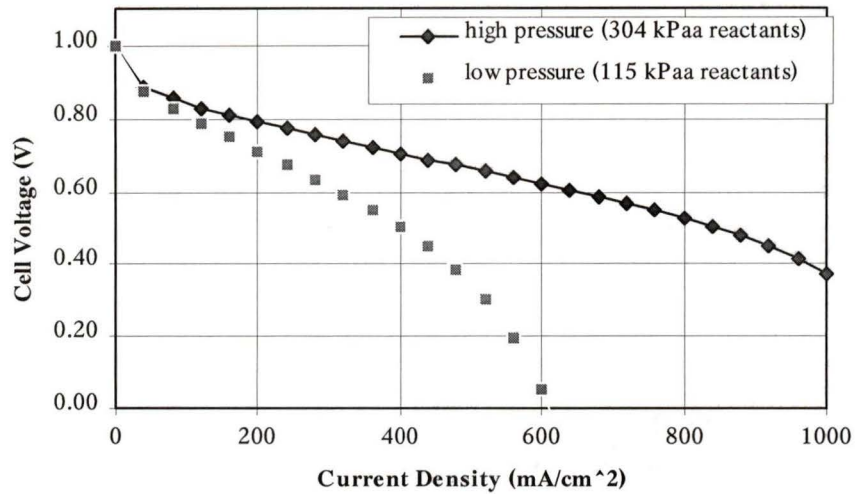


Figure 2.15: Effect of Pressure on Performance for a PEM Fuel Cell (80°C, *standard* electrodes)

PEM fuel cells operate most effectively at a temperature of 75 to 90°C with pressures up to 500 kPa_a. In the case of the ambient air system, no pre-heating is done to the reacting air stream. Thus, air enters the stack at ambient temperature and pressure which has significant performance implications. For additional information on polarization curves, see Section 3.2

A method of improving performance and reliability for the ambient designs, although with increased complexity, is to separate the low pressure stream into reactant and cooling streams. Then, the reaction stream can be pre-heated. The options available for pre-heating are counter-flow heat exchange with exhaust cooling or reactant air streams. However, the thermal mass of the exiting hydrogen stream is small and this is not considered a good choice. Another option is to circulate the reactant streams in a non-reacting portion of the stack prior to entering the reaction channels. This is done in some high temperature tubular solid oxide fuel cell designs [8]. The burning of hydrogen fuel is an option, but is very poor from an efficiency standpoint.

2.5.4 Heat Removal

The removal of heat is very important to steady state performance. Air is a poor coolant due to its low density and specific heat. However, ultimately all of the fuel cell's heat needs to be rejected to the surrounding air. Therefore, it seems logical to complete the heat transfer in the stack and eliminate intermediate heat transfer steps.

The cooling mechanism are similar with both designs. The cooling air stream (forced convection) and evaporative cooling are the active cooling mechanism, while radiation and natural convection are passive mechanisms. In both cases large volumes of low pressure air are required for cooling.

2.5.5 System Considerations

With the tandem air system, a compressor is required to supply the reaction air. When air is compressed it increases in temperature. The relationship between compression ratio and adiabatic discharge temperature is shown in Figure 2.16. Full load performance characteristics of an *Opcon Autorotor twin-screw* type compressor were attained [11]. For a pressure ratio of 2.5, and considering an isentropic efficiency of 50 to 60 percent which is typical of an *Opcon Autorotor* compressor, the discharge temperature was found to range between 413 K (140°C) and 428 K (155°C) depending on compressor speed, considerably higher than the adiabatic assumption.

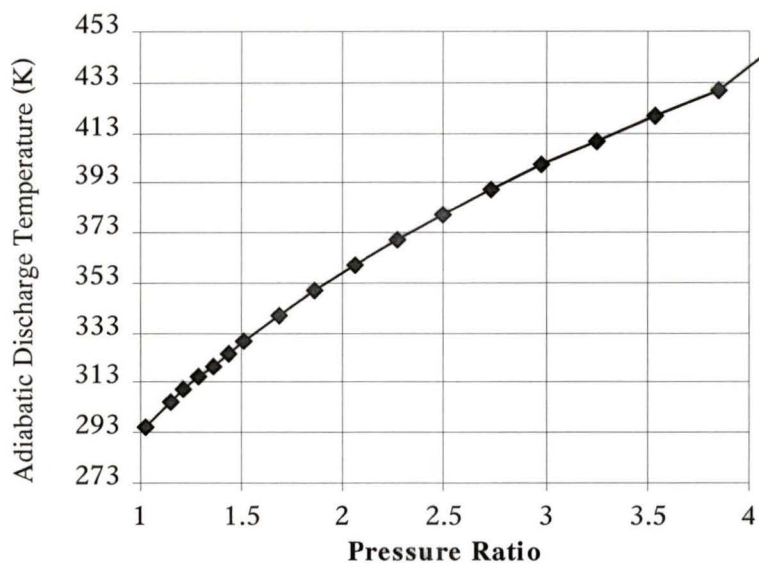


Figure 2.16: Adiabatic Discharge Temperature versus Pressure Ratio
(inlet air at 20°C, 101.3 kPa)

This increase in temperature is a benefit in terms of PEM reaction conditions as it can be cooled to the desired temperature (easier to cool than warm with available flow streams). However, this comes with a loss in system efficiency, and is an added drawback in terms of heat rejection. The compression, combined with cooling mechanisms, can be used to control the inlet temperature of the reactant air stream. Obviously, a large drawback is the electrical compressor load.

In the ambient air designs, a fan is used to supply both the reaction air and cooling air due to small pressure rise requirements. Blowers are an option, but are noisy components suitable for greater pressure rise requirements [10].

2.5.6 Summary

It is evident that for a high power density engine, the reaction and cooling air cannot occupy the same channel. For ambient air designs, this is partially due to high air stoichiometries required for cooling. Large air flows, low pressure air, and stack temperature gradients, all increase humidification difficulties. Staged internal

humidification would be required in the reactant channels due to the large air temperature increase. The need for humidification further leads to considering metered water addition at multiple points. This approach adds operational complexity and lowers reliability.

Using an ambient air system has important implications to the polarization curve, and thus to maximum power output and stack power densities. With current PEM technology, systems are not greatly exceeding power density targets. Thus, it seems unrealistic to go to a low pressure, low temperature system with the current technology although high efficiencies are attainable.

Choosing a tandem air system with independent reaction and cooling air streams was a recognized solution to many concerns. With the reaction air as a separate stream, greater control of the reaction gas supply conditions is inherent. The reaction air may then be supplied at a stoichiometry, temperature and pressure as desired.

2.6 Design 4: Tri-Stream Externally Manifolder RSA Design (TERS96)

After discussions with the NGFT materials group at Simon Fraser University [46] and further research into the use of metals with fuel cells, the RSA design group was primed for another change. A new idea came forth that allowed for the complete isolation of metal components from the membranes. A successful change in current collection also occurred. The new design is a plate and frame design that eliminates double edge collection. The stack is comprised of alternating fuel cell(s) and cooling elements. To manufacture the reactant delivery plates, a complementary NGFT research topic, screen printing [41], is used to create the flow field paths. A representation of the design is shown in Figure 2.17.

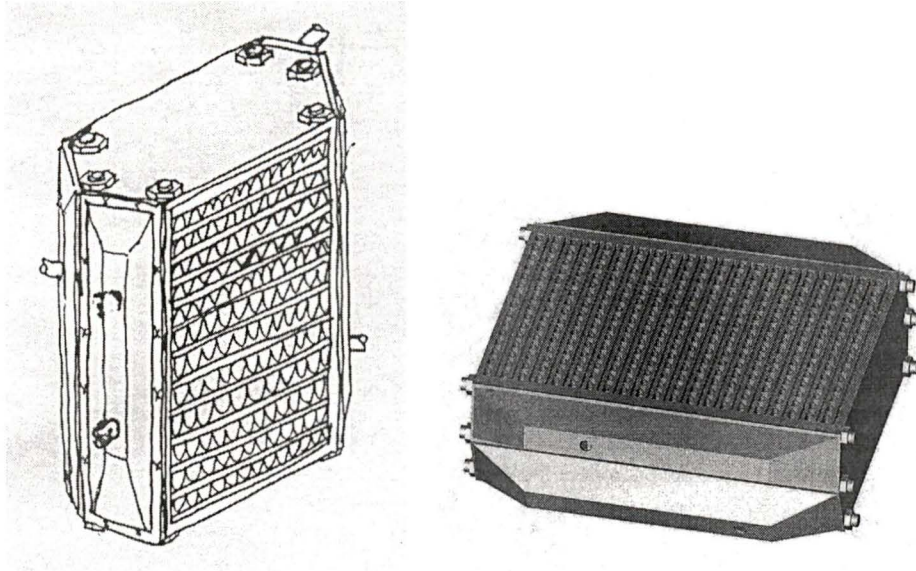


Figure 2.17: Externally Manifolder RSA (TERS96)

The hexagonal shape allows for non-interfering external manifolding and cross flow of fuel, oxidant and cooling air in the stack. The cross-section of the plate, complete with cut outs for six support rods, is shown in Figure 2.18.

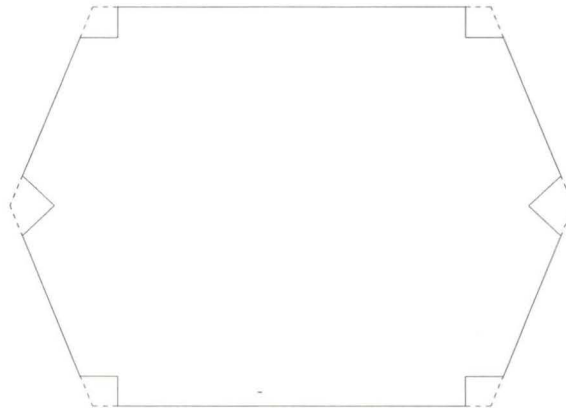


Figure 2.18: Top View of Hexagonal TERS96

The cooling elements are made of copper and completely isolated from membranes. The cooling panels are comprised of a waved copper sheet soldered, or welded, in between two flat copper sheets. The dimensions of the cooling fin are determined by mass transport, structural integrity, and optimization work. A processed cooling plate surface

with controlled roughness can be used to vary local heat transfer capabilities along the panel as it transfers heat to the cooling air stream. A low heat transfer coefficient is desired at the inlet. This is the location with the largest ΔT between the fin and cooling air.

A main concern with external manifolding is sealing [44]. Temperature changes, cyclic stresses and different materials at interfaces, all create difficulties. With the design presented, the cooling panels can serve an additional purpose, and act as a distributed spring system. This allows for compensation for thermal and mechanical stresses, and a near fixed stack length, which makes external manifolding possible.

Six stack support columns located at each corner of the periphery, help form the rigid stack. The columns locate and hold all fuel and oxidant plates in place, and provide a mating surface for external manifolds to be mounted. This externally manifolded design allows for 80 to 90 percent of the stack envelope to be electrochemically active. There are no centre holes in the plates, and only a sealing allowance is required around the outer edge.

Figure 2.19 illustrates the differences between internal and external manifolding.

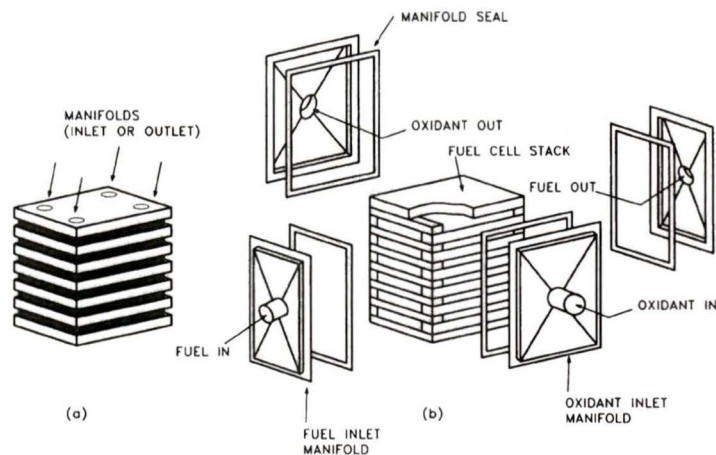


Figure 2.19: Manifolding Concepts [8]
 (a) internal manifolding (b) external manifolding

2.7 Design 5: Tri-Stream Externally Manifold RSA Design (TERS97)

In October 1996, a design change was made to reduce manufacturing costs. The plate shape was altered from a hexagon to a square.

The architecture proposed differs in several respects from traditional plate and frame arrangement. As with the TERS96 design, air cooling panels are interspersed between every cell, or group of cells, which provide a current path for electrons, ensure adequate cooling and maintain stack integrity and rigidity. An illustration of the design is shown in Figure 2.20.

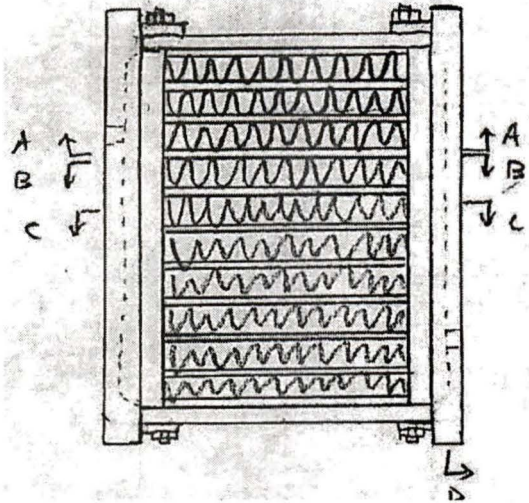


Figure 2.20: Tri-Stream External Manifolder RSA Design (TERS97)

2.7.1 TERS97 Prototype

As a proof of concept for manufacturing and sealing, a prototype was constructed. A physical model was completed in March 1997 to ensure adequate manufacturability. This validated its feasibility. A working model is currently under construction containing four cells. Initial testing was conducted in September and October 1997.

The prototype is based on a power plant sized to give an output of 62.1 kW. The stacks have a near square footprint and an active area of 245 cm². The power plant includes 8 stacks, each containing 75 cells. The stack is held together by 6 non-conducting support columns. These columns, along with the two end plates on each stack, are used as a sealing base for the external manifolds.

2.8 Design 6: Tri-Stream Internally Manifolder RSA Design

As an alternative to Design 5, an internally manifolded design was introduced. This design is shown in Figure 2.21.

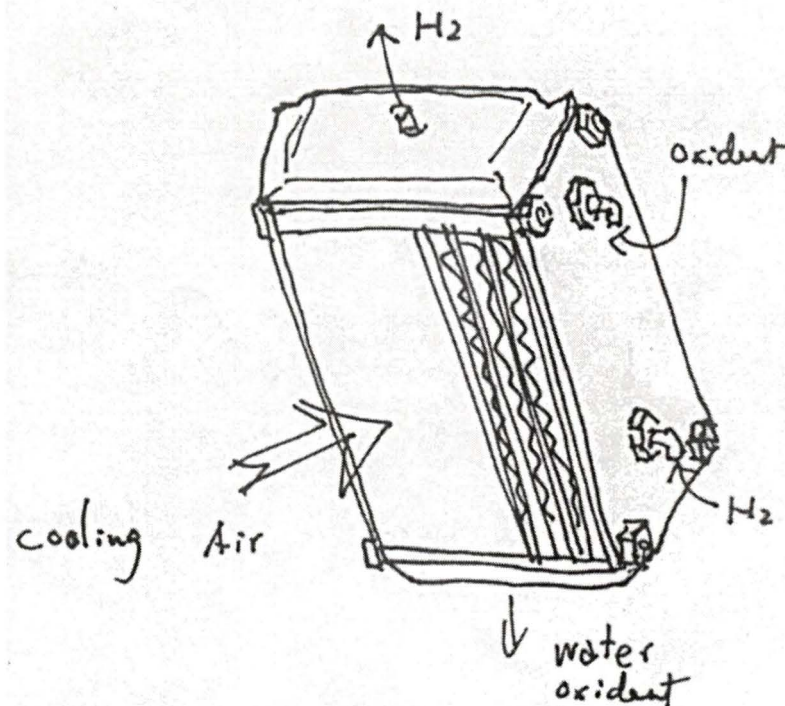


Figure 2.21: Internally Manifolder Tri-Stream RSA Design

This design is similar in manifolding to Ballard's MK-7 design [17]. Design 5 was favored over this design as it as felt to be less complicated in construction, sealing and manifolding.

2.9 Architecture Summary

The scope of work for modeling has been presented. Both ambient and tandem air systems have been considered. Modeling of *all the various systems*, with existing membrane technology, revealed that tandem air systems, with independent reaction and cooling air, are better suited to the high power density automotive application. This along with specific results for Design 5: Tri-Stream Externally Manifold RSA Design (TERS97) led to it being chosen as a focus for experimental work. Chapters 3 and 4 are a summary of the modeling and experimental work performed. The general system is modeled as shown in Figure 2.22.

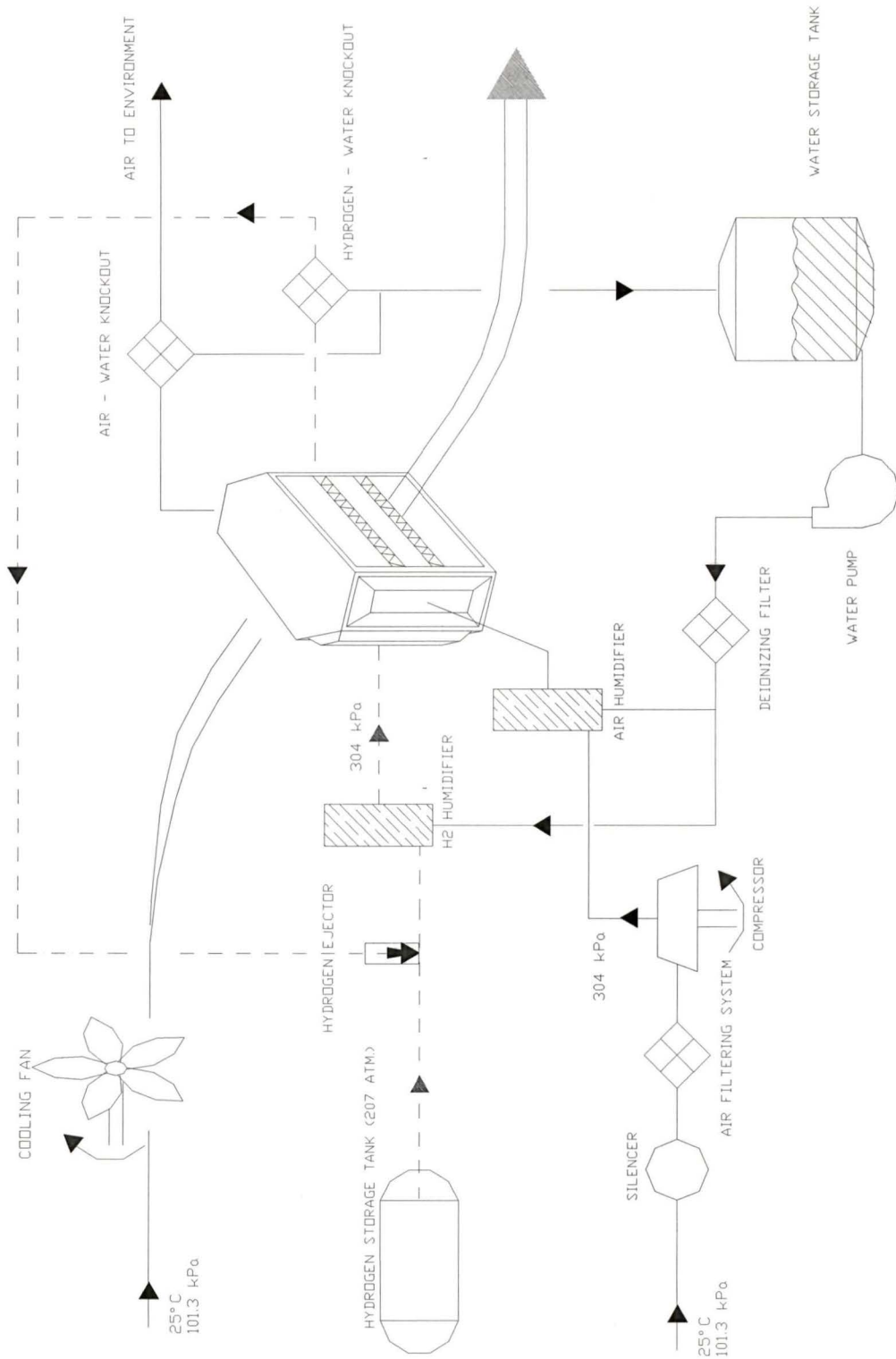


Figure 2.22: General Fuel Cell System Schematic for Tandem Air Designs

Chapter 3

Performance Model of PEM Fuel Cells

Performance modeling of air-cooled proton exchange membrane (PEM) fuel cells was undertaken to evaluate if they are a feasible alternative to more prevalent water-cooled designs. The benefits of air-cooling were outlined in Chapter 1.

The fuel cell reactants, compressed air and pure hydrogen, are externally humidified and supplied using external manifolding in all but Design 6. Both mass and overall thermal energy balances have been included. The thermal characterization includes: the theoretical energy released by the reaction, evaporative cooling effects of the product water, natural convection, radiation, and most importantly, forced convection by the cooling air. Sensible heat has not been included due to the external preparation of the reactants for the fuel cell stack. This leads to a relatively small change in specific internal energy inside the stack. The influence of the parasitic compressor, cooling fan and humidification water pump on system performance are also considered. Performance models of the air-cooled radiator stack designs are implemented as FORTRAN programs.

3.1 Stack Model

The parameterization of the stack design is the first step in a design's evaluation. The key independent variables are identified. The remainder of the dimensions are dependent variables calculated using the independent variables. Obviously, not entire areas can be

active, therefore, contingencies are set aside for sealing, reactant gas manifolding, structural support, manufacturing tolerances and other design issues. This was done for designs 1 through 5, including many of the design modifications.

For each design, dimensions were initially specified using preliminary calculations. For example an outer volume, or target power output, is specified. For the designs examined, a 64 kW gross output was a design target.

3.2 Polarization Curves

Fuel cell polarization curves can be built-up by examining reversible thermodynamic equations, combined with the negative effects of activation, ohmic, and concentration overpotentials. This is generally represented as shown in Equation 3.1

$$E = E_r - \eta_{act} - \eta_{ohmic} - \eta_{concentration} \quad (3.1)$$

where E_r is the reversible voltage, which can be calculated using

$$E_r = \frac{\Delta G^o}{2F} + \frac{\bar{R}T}{2F} \left(\ln(P_{H_2}) + \frac{1}{2} \ln(P_{O_2}) \right) \quad (3.2)$$

This represents the reversible cell potential. This is valid for operation at standard conditions. For other conditions, additional terms are required. Substituting the appropriate values, the reversible cell potential can be shown as follows

$$E_r = 1.229 - 0.85 \times 10^{-3} (T - 298.15) + 4.31 \times 10^{-5} T \times [\ln(P_{H_2}) + \frac{1}{2} \ln(P_{O_2})] \quad (3.3)$$

where P represents pressure, and T , temperature in Kelvin. Rather than use the semi-empirical model shown, *a completely empirical model was used*. An empirical equation proposed by Kim [22] has been shown to fit experimental cell potential for various current densities at several temperatures and pressures. The model is as follows

$$E = E_0 - b \log j - R j - m \exp(n j) \quad (3.4)$$

The exponential term compensates for the mass-transport regions at higher current densities. The terms E_o and b (Tafel parameter) yield the electrode kinetic parameters for oxygen reduction and R represents the resistance, predominantly ohmic and, to a small extent, the charge transfer resistance of the electro-oxidation of hydrogen. All modeling is based on Nafion 117 membranes, with catalyst loadings of 4.0 mg/cm^2 per electrode.

3.2.1 Operating Temperature

An operating temperature of 85°C is used for model results. Most PEM fuel cells using polyfluorinated sulfonic acid membranes have ideal operating temperature range of 75 to 90°C . In general, optimum operating temperature is dependent on the chosen membrane, and also to a lesser extent on the humidification design and air compression system. For air-cooled operation, it is desirable to have a high operating temperature because this facilitates heat rejection.

Normally, a temperature transducer in the oxidant exit stream is used to indicate the stack operating temperature [5]. This temperature closely represents the stack operating temperature, and has a safety benefit in that it will continue to monitor stack temperature in case of coolant circulation loop failure. In the case of the air-cooled designs, due to a changing cooling air temperature, a more accurate operating temperature is defined as the fin temperature at the cooling air exit.

3.2.2 Tandem Air Polarization Curve

As a basis for the polarization curve for tandem air designs, polarization curves were obtained for “standard” fuel cell operation [22,3,71,5] with reactant gas pressures of 304 kPa_a at 85°C , with hydrogen and air stoichiometries of 1.5 and 2.0 respectively. Curve fitting was then performed on the obtained data using Equation 3.4. The curve fitted parameters are shown in Table 3.1.

Table 3.1: Values Of Electrode Kinetic Parameters for Tandem Air Designs

| Parameters | Units | Value of Parameter |
|------------|---------------------------|--------------------|
| E_o | mV | 1,012 |
| b | mV / dec | 0.030 |
| R | $\Omega \text{ cm}^2$ | 3.1e-4 |
| m | mV | 3.0e-4 |
| n | cm^2 / mA | 6.0e-3 |

3.2.3 Ambient Air Polarization Curve

A similar process was done for the ambient air designs. Approximate polarization curves were obtained from references [5,43,24]. Ideally, a polarization curve was desired for operating air and hydrogen pressures of 110 to 120 kPa_a with stoichiometries greater than 50. Unfortunately, the literature contains a limited database of polarization curves, and, as expected, an exact match was not found. Extrapolation was used on the available data. The constant curve-fitted parameters are shown in Table 3.2.

Table 3.2: Values Of Electrode Kinetic Parameters for Ambient Air Designs

| Parameters | Units | Value of Parameter |
|------------|---------------------------|--------------------|
| E_o | mV | 970 |
| b | mV / dec | 0.030 |
| R | $\Omega \text{ cm}^2$ | 4.7e-4 |
| m | mV | 4.0e-4 |
| n | cm^2 / mA | 7.0e-3 |

It is assumed that the membrane remains fully hydrated.

3.2.4 Summary

With both types of designs, the stack at the cooling air inlet experiences more cooling than at the outlets, where the warm air exits. Thus, a temperature gradient in the direction of the cooling air flow is created within the stack. Conduction in stack elements help to lessen this gradient. Deterioration in performance due to this non-isothermally operation

effect has not been included. Significant changes in performance will not occur with small temperature changes. However, the more serious implications are in regards to water management, and are difficult to predict.

In addition, performance change has not been included due to the decrease in reactant pressure and concentration, as the streams pass through the reaction channels.

3.2.5 Resistivity Modeling

Due to dissimilarities in current collection compared to standard plate and frame fuel cell stacks, extra electrical losses are considered. This is true for both the edge collection and plate and frame arrangements considered. It is assumed that the ohmic polarization losses for the basic conducting graphite plates and membrane electrode assembly are accounted for in the base polarization curve. For instance, the additional effects resulting from the presence of copper cooling panels (that the current must pass through) are considered. The model includes a ΔV loss using Ohm's Law considering the *bulk* resistivity and geometry of each component as shown in Equation 3.5.

$$R = \frac{\rho_{material} L}{A_{cs}} \quad (3.5)$$

This extra loss reduces efficiency, and increases the amount of heat to be rejected. The effects of contact resistance are known to be very significant, but are currently neglected at each interface. Contact resistance is known to be a function of the interfacing materials, contact pressure, surface preparation and contact area.

A bipolar fuel cell design offers the advantages of short current collection path and small ohmic losses, even with graphite materials. Designs using double-edge collection or additional material interfaces, have greater design flexibility, however lead to a performance penalty. A sample of how additional resistances are modeled is shown in Figure 3.1.

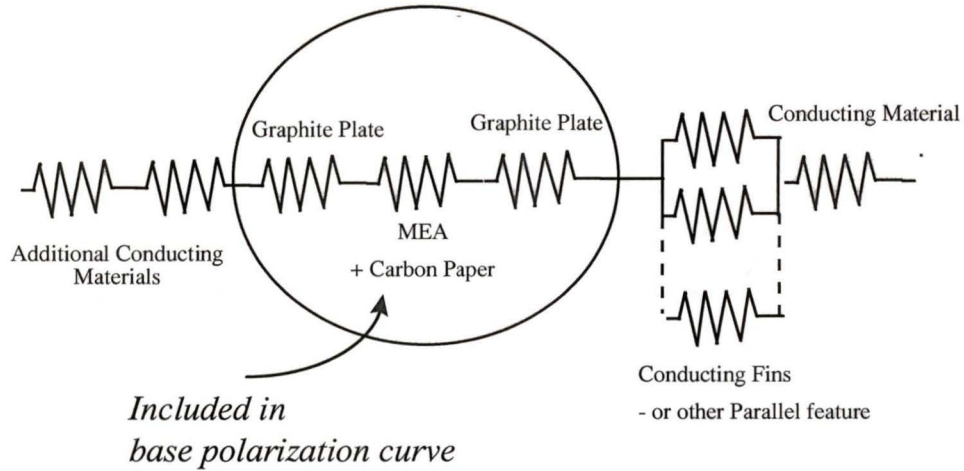


Figure 3.1: Resistance Modeling for RS Architectures

3.3 Reactants

3.3.1 Reactant Air Stream

Oxygen, necessary for the reaction, is obtained from ambient air. Due to the sensitivity of the proton exchange membrane to contaminants, the incoming air stream must pass through a filtering system. Standard air filtering systems consist of a particulate filter which removes particles to a minimum of $1 \mu\text{m}$, a coalescent filter which removes particles to $0.01 \mu\text{m}$, and a carbon filter which removes oil vapors and odours [5]. Additional components required include a mechanical device such as compressor, blower, or fan, along with an external humidifier and mass flow controller. The required air flow rate is a function of the total current

$$m_{air} = \frac{I_T M_{air} N_{cells} \lambda}{4F x_{O_2}} \quad (3.6)$$

Air is supplied to individual MEAs through a number of channels in the flowfields. The channel length and dimensions are important design parameters. To maintain the system

water supply, water is removed from the exiting air stream using a water knock-out device.

A heat capacity and density comparison is shown in Table 3.3 for species commonly found in PEM fuel cells.

Table 3.3: Heat Capacities of Selected Mediums @ 300 K [35]

| <i>Species</i> | Heat Capacity (KJ/kg K) | Density (kg/m ³) |
|-----------------|----------------------------|---------------------------------|
| Air | 1.006 | 1.177 |
| Hydrogen | 14.31 | 0.0819 |
| Water | 4.181 | 998.5 |
| Stainless Steel | 0.46 | 7800 |

Air's low density gives insight into the necessity for high flow rates.

3.3.2 Reactant Hydrogen Stream

Pure hydrogen is supplied from a high-pressure gaseous storage tank. The hydrogen supply system components include an expansion valve, pressure regulator, filter, external humidifier and ejector for recirculation purposes. A water knockout is used on the hydrogen recirculation loop, also to help maintain system water volumes. The required hydrogen flow rate is a function of total stack current

$$m_{H_2} = \frac{I_T M_{H_2} N_{cells} \lambda}{2F} \quad (3.7)$$

The hydrogen is supplied to the MEA through flowfield channels. This system is self-reliant having no major electrical loads. The system operates on the mechanical exergy of the hydrogen gas which is stored at pressures up to 205 atmospheres.

Due to minimal performance improvement with increasing reactant hydrogen pressure, on the order of 20 mV/atm. H₂ [43], hydrogen pressure is maintained at the same pressure

as the reactant air stream. The detriments of having a pressure gradient across the membrane include additional complexity in sealing, increased gas cross-over and reduced cell lifetimes.

Due to the storage temperature and pressure of the hydrogen gas, it has a negative Joule-Thomson coefficient. Thus, the gas temperature increases during an expansion process. The hydrogen gas temperature is expected to increase, up to a maximum of 10°C, during the expansion process. The Joule-Thomson coefficient is defined as

$$\mu_{jt} = \left(\frac{dT}{dP} \right)_h \quad (3.8)$$

and varies as a function of both temperature and pressure. At room temperature, and at low or moderate pressures, the state of most gases fall within the inversion curve. However, when hydrogen is at room temperature, its state falls outside the inversion curve [15]. Although hydrogen depressurization cannot be directly used for cooling, some of the mechanical exergy can be recovered to increase overall system efficiency through use of a turbine. This was not implemented into the model due to system cost and simplicity considerations.

3.3.3 Air Properties Variation With Temperature

The air properties of density, heat capacity, viscosity, and thermal conductivity are important to cooling calculations. As such, air properties are calculated as a linear function of temperature when necessary. The average temperature is used to approximate properties over the temperature difference. The properties are approximated by linear equations over the temperature range 0 to 85°C.

3.4 Humidification

Usually, fuel and oxidant gases require humidification to ensure that membranes are constantly saturated. For humidification, the saturation pressure for water vapour is only a function of temperature, and can be defined using the empirical equation [15]

$$\ln(P_{sat}) = 70.434643 - \frac{7362.6981}{T} + 0.006952085T - 9.0000 \ln T \quad (3.9)$$

where T is temperature in Kelvin, and P_{sat} is the saturation pressure in atmospheres. With the saturation pressure known, the amount of humidification water to be added to each reactant streams can be determined

$$\text{for the air stream: } \dot{m}_{humid. water} = \frac{M_{H_2O}}{M_{air}} \frac{P_{sat}}{P_T - P_{sat}} \dot{m}_{air} (\phi_{air desired} - \phi_{air current}) \quad (3.10)$$

$$\text{for the hydrogen stream: } \dot{m}_{humid. water} = \frac{M_{H_2O}}{M_{H_2}} \frac{P_{sat}}{P_T - P_{sat}} \dot{m}_{H_2} \phi_{H_2 desired} \quad (3.11)$$

Generally, a relative humidity of 90 to 100 percent is used for the reactant streams. Part of the model's usefulness is that it can examine the effects of different input relative humidities for the reactants on the overall water and energy balance.

To maintain water for humidification purposes, water knockouts are required. A tank is used to store the water, and a small humidification pump circulates the water.

The exact relationship between cell deterioration and membrane dry-out and catalyst layer flooding is difficult to predict. As such, the estimated polarization curves assume that adequate membrane water content is maintained. Thus, the effects of flooding and dry-out cannot be analyzed unless a mechanistic model is introduced.

In the case of the ambient air designs, a high reactant and cooling air flow rate gives it a significant ability to absorb moisture. However, air humidification is required if significant current densities are to be attained. Ballard Power Systems has demonstrated an ambient air system that operate at ambient conditions, and utilizes product water solely to maintain membrane water content [43]. Figure 3.2, constructed using Equation 3.9, shows air's ability to absorb water as a function of pressure and temperature.

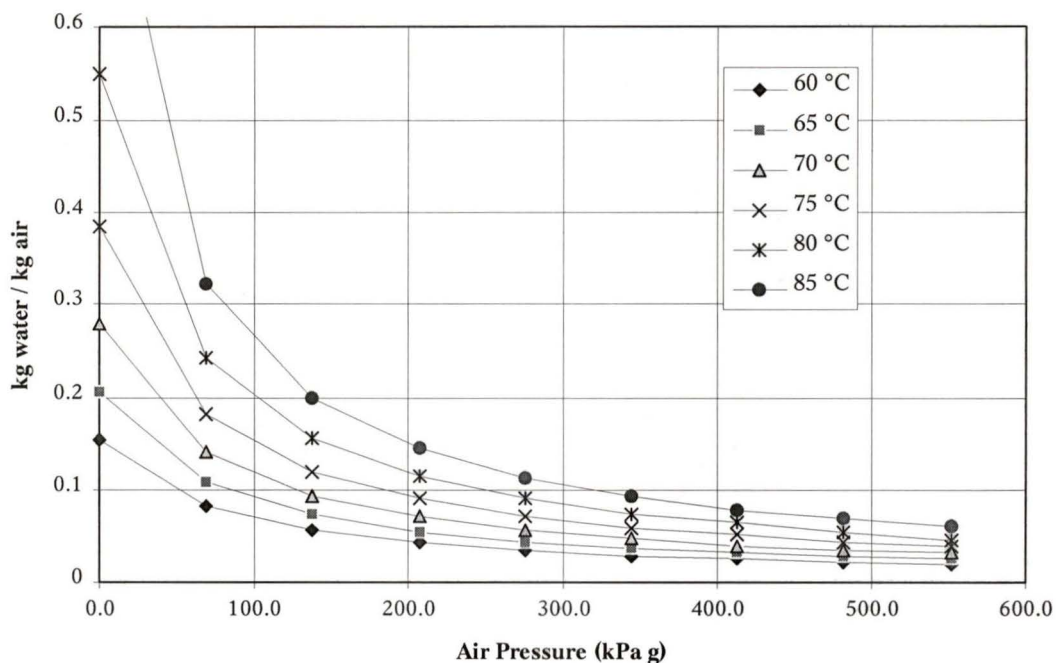


Figure 3.2: Water Saturation in Air versus Pressure (for various temperatures)

One of the advantages of pressurized operation is that significantly smaller quantities of water per unit mass of air are required for saturation. Also, at high pressures, humidification of a smaller volume of air is required. Figure 3.2 shows that, for a given temperature, the humidity ratio varies as P_{sat}/P .

Usually, it is convenient to humidify gases as near as possible to the overall operating temperature and pressure of the fuel cell. For this reason, humidification is sometimes integrated with the active portion of the stack. With the ambient air RSA designs, a temperature gradient is necessary between the incoming air and the fuel cell operating conditions. This causes humidification difficulties.

3.5 Cooling Requirements and Mechanisms

Proper water and heat management are essential for obtaining high power densities. The model includes mass and energy balances to ensure successful operation. As power densities increase, or fuel cell stacks become larger, the need for more compactly

designed active cooling systems increases. Cooling only the stack surface does not ensure overheating. To achieve acceptable temperature gradients, the usual practice is to position a cooling cell between cells, or groups of cells. This causes heat to flow axially through cells, rather than along the plane of the cells. Another option is edge cooling, which relies on high internal conductivity of stack components. Cooling channels are located around the periphery of the stack. Heat is then conducted from active areas to these channels.

Gas cooling is the simplest of all methods of active cooling. The major advantage of air cooling is its simplicity and low cost. If each cell is cooling equally, then there is virtually no ΔT in the direction perpendicular to the flow. However, because the coolant's internal energy increases as it flows across the cells, a ΔT occurs in the flow direction, giving uneven cell performance over the active area. The size and profile of the cooling flow channels are critical as pressure drop is important to fan power consumption. A balance between heat transfer surface area and pressure drop is important.

The cooling requirements of each stack are determined using a simple thermodynamic approach. Stack efficiency may be defined as the gross electrical stack output divided by the energy content of the hydrogen consumed. The model considers the higher heating value (HHV) of the hydrogen as *some* of the product water exits the stack in the liquid state. This approach is illustrated in Figure 3.3.

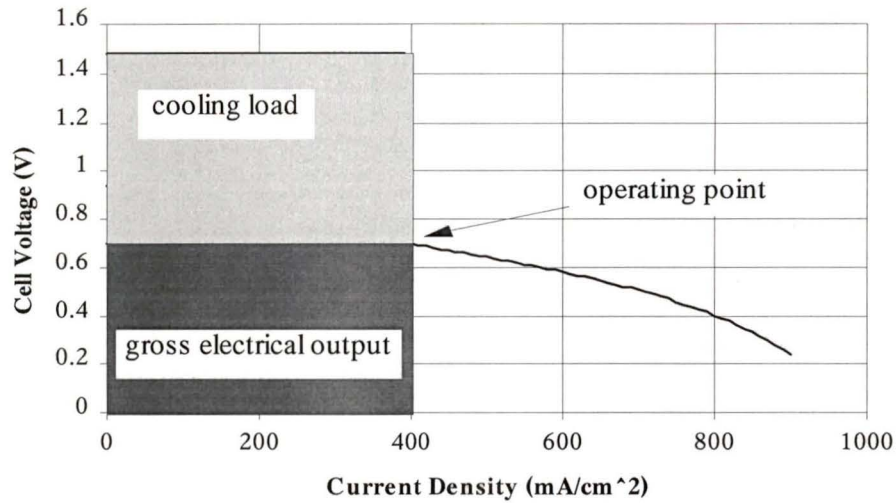


Figure 3.3: Thermodynamic Approach for Calculating Cooling Load

The reversible cell voltage can be determined using

$$E_r = \frac{\Delta G}{nF} \quad (3.12)$$

where ΔG is the Gibbs Free Energy change, n is the number of electrons in the elementary reaction, and F is Faraday's Constant. However, the unattainable maximum output voltage corresponding to 100 percent efficiency, which is useful for cooling calculations can be determined using

$$E_{\max} = \frac{\Delta H_{HHV}}{nF} \quad (3.13)$$

where ΔH is the enthalpy change. Therefore, the amount of cooling can be determined using 3.14, or alternatively 3.15

$$\dot{Q}_{total} = (E_{\max} - V_{cell\ gross}) I_T \quad (3.14)$$

$$\dot{Q}_{total} = \dot{m}_{H_2} \Delta H_{HHV} - P_{gross\ stack} \quad (3.15)$$

where \dot{m}_{H_2} represents the hydrogen consumed in the reaction. For the reaction considered (1.1), 1.48 V represents 100 percent efficiency. This provides a technique for calculating cooling load at various current densities. The cooling load is satisfied by various cooling mechanisms. The mechanisms considered include radiation, natural convection, evaporation of product water, and forced convection using cooling air

$$\dot{W}_{theor.max} - \dot{W}_{e,gross} = \dot{Q}_{radiation} + \dot{Q}_{nat.conv.} + \dot{Q}_{evaporation} + \dot{Q}_{forced.conv.} \quad (3.16)$$

The simplest method to remove heat from a fuel cell is to use purely passive cooling such as radiation and natural convection. Cooling with these methods is dependent on the temperature differential between ambient air and the stack surface, and also stack orientation when considering natural convection. To maintain an acceptable energy balance, and keep the operating temperature constant, the cooling air flow rate must change depending on operating current density.

The net radiation loss is the difference between energy emitted and the energy absorbed

$$Q_{radiation} = A\varepsilon\sigma T_s^4 - A\alpha\sigma T_{amb}^4 \quad (3.17)$$

assuming emissivity equal to absorptivity ($\varepsilon = \alpha$), the equation simplifies to

$$Q_{radiation} = A\varepsilon\sigma (T_s^4 - T_{amb}^4) \quad (3.18)$$

For natural convection, vertical and horizontal surfaces were considered independently. The vertical surfaces were examined [35] using

$$Nu_m^{1/2} = 0.825 + \frac{0.387 Ra_L^{1/6}}{\left(1 + (0.492/Pr)^{1/6}\right)^{8/27}} \quad (3.19)$$

where Nu and Ra are the Nusselt and Raleigh numbers respectively. This applies to both laminar and turbulent flow. For horizontal sections, the heat transfer equation (3.20) was used

$$Nu_m = \eta c Ra^{1/4} \quad (3.20)$$

where c is 0.54 for upper stack surfaces, and 0.27 for lower surfaces. An efficiency (η) of 50 percent was used to reduce the amount of convection due to typical vehicle enclosures. This analysis is similar to that found in other references [1,33]. These passive techniques can be improved by including interior materials with good thermal conductivities, or adding exterior cooling fins.

Two types of active cooling systems are used in the designs. These include forced convection and evaporative cooling. The details for forced convection are given in Chapter 4. For evaporative cooling, due to analysis convention, product water exiting the stack in a vapor form is considered a cooling effect.

3.6 Cooling Panels

It is speculated that most of the waste heat in a PEMFC is generated at the three-phase reaction surface of the cathode. Thus, for a complete 3-D heat transfer analysis, heat conduction from the cathode (or membrane) to the cooling panels must be considered. For simplicity, and due to the high thermal conductivity of the panel, an isothermal assumption is used for panels. A temperature of 85°C is considered.

In the stack design, the cooling panel elements have multiple functionality. Firstly, and most important, is the heat rejection capacity. The cooling panels must reject most of the stack's low-grade heat. Secondly, due to their location in the stack, the panels must serve as a current path for the electrons to pass from cell to cell. This lengthens the current path in the stack, but is acceptable due to the panel's low resistivity. Lastly, these cooling panels serve as deformation compensating elements to account for thermal expansion and pre-load and operating stresses. One of the common difficulties with externally

manifolded stacks is reactant gas sealing. The spring-like ability of the cooling panels ensures reduced stresses at critical sealing points and ensures proper sealing. This triple functionality requires design iterations and optimization to identify a desirable design. The parameterization of the fin element inside the cooling panel includes fin pitch, fin thickness and a shape parameter. By choosing short flow paths and well-designed channels, pressure drops can be maintained at acceptable levels.

3.6.1 Cooling Air Pressure Drop Analysis

The cooling air flow is modeled as flow through ducts of rectangular and triangular cross-sections. The air channel dimensions are important as they influence pressure drop which is critical to fan power consumption and system performance. Pressure drop through a duct can be described by the relation

$$\Delta P = \frac{fL\rho\bar{u}^2(sf)}{2D_{hyd}} \quad (3.21)$$

where f is the Darcy friction factor, L is the duct length, ρ is the air density, \bar{u} is the average duct air velocity, sf is a safety factor, and D_{hyd} is the hydraulic diameter. The safety factor is used to account for additional pressure drops due to entrance and exit effects, ducting and manifolding, and filtering where necessary. It has been shown that the pressure drop through filters is also proportional to the flow rate squared [11].

3.7 Discharge Air Temperature

The outlet temperature of the cooling air as it exits a cooling panel, is a good measure of heat exchanger effectiveness. The outlet air temperature is determined using a logarithmic mean temperature difference (LMTD) method.

$$\dot{Q} = A_{cooling} h_m \Delta T_{lm} = \dot{m} c_p (T_{outlet} - T_{inlet}) \quad (3.18)$$

where \dot{m} is the cooling air mass flow rate, $A_{cooling}$ is the total heat transfer surface, ΔT_{lm} is the temperature difference between the cooling fin wall and channel air, and T_{inlet} and T_{outlet} are the inlet and outlet air temperatures, respectively. ΔT_{lm} can be calculated as shown

$$\Delta T_{lm} = \frac{T_{outlet} - T_{inlet}}{\ln \left(\frac{T_{wall} - T_{inlet}}{T_{wall} - T_{outlet}} \right)} \quad (3.22)$$

The use of a correction factor (F) is often used for various complex heat exchanger geometries. However, this factor has been neglected for this analysis. The temperature of the outlet air is determined using an iterative process. Initially, the outlet air temperature is estimated as the fin temperature, with the outlet air temperature known, the amount of heat rejection can be calculated. This heat rejection is then compared to the remaining cooling load. If the two are not equivalent, the air mass flow rate is recalculated, and a new outlet air temperature determined. As the air mass flow rate affects many other variables such as air flow velocity, flow conditions, pressure drop, heat transfer coefficient and fan power consumption, the process is iterated until convergence occurs.

The average heat transfer coefficient, h_m , is calculated from the Nusselt number (hD/k). The Nusselt number is calculated using various correlations depending on the Reynolds number and fin cross-section. These specific correlations are introduced in Chapter 4.

3.8 Parasitic Loads

As fuel cell efficiency is important, the energy requirements for air compression, cooling system and humidification water pump are considered. The additional losses for a controller and power conditioner are not considered as they are equivalent for all designs.

3.8.1 Air Compression

The air compressor system load can be determined using

$$\dot{W}_c = m c_p T_{in} \left(\left(\frac{P_2}{P_1} \right)^{\frac{\gamma}{\gamma-1}} - 1 \right) \eta_{module}^{-1} \quad (3.23)$$

This adiabatic compression model assumes that air behaves as an ideal gas and has constant specific heats over the temperature range considered. The *module efficiency* compensates for irreversibilities in the compression process and the electric motor.

3.8.1.1 Compressor Discharge Air Temperature

As oxidant air is compressed outside of the stack, it does not provide an additional stack heating load. The reactant air enters the stack at a controlled temperature using an air to air heat exchanger (using either the high pressure or low pressure exiting air as a cold stream), or the air humidifier. Unfortunately, the adiabatic discharge air temperature is much easier to calculate than the actual discharge temperature from a compressor [11]. Actual performance curves for a specific compressor should be used in the detailed design phase to provide more accurate discharge temperature data.

3.8.2 Cooling Fan

Pressure drop through the cooling panel is calculated to determine the required pressure rise requirements for the cooling fan. The pressure rise and calculated volumetric flow rate of the cooling air determine fan power consumption as shown

$$\dot{W}_f = \dot{V} \Delta P \eta_{module}^{-1} \quad (3.24)$$

A minimum power consumption of 50 W is assigned to the cooling fan when operating at low current densities. The module efficiency compensates for both mechanical and electric efficiencies.

3.8.3 Humidification Water Pump

The methodology shown in Section 3.8.2 is used to determine the electrical load for the humidification water pump. A minimum electrical load of 100 W is used. Due to the

elimination of the intermediate coolant in the Radiator Stack designs, the water pump circulates significantly smaller flow rates than in traditional PEM fuel cell designs.

3.8.4 Module Efficiency

The term module efficiency is used to combine the losses of the device and the electric drive motor. The efficiency of the drive motor was taken to be 80 percent. Compressors, fans and pumps generally have a design point where they operate at peak performance. In the case of a fuel cell system, components are called upon to operate at various flow rates. Thus, the module efficiency was allowed to vary according to a quadratic fit of performance data.

$$\eta_{module} = c_1 Q^{*2} + c_2 Q^* + c_3 \quad (3.25)$$

The coefficients $c_1, c_2, \text{ and } c_3$ are specific to each device, and Q^* is a normalized flow rate.

3.9 Calculation of Weight

Important to these modeling efforts is the determination of power densities. The volume of each stack is simple to determine, as it involves multiplying outer stack dimensions. The calculation of weight is a more complicated matter. To calculate weight, the stack is broken down into its major areas. These include

- Cells,
- Conducting/cooling layers
- Supporting frame
- Reactant gas manifolding

A simple volume-density method is used to calculate the weight of various components. The total weight is the sum of the components as shown

$$W_{total} = \sum_{i=1}^N \rho_i V_i \quad (3.26)$$

3.9.1 Materials of Construction

Graphite, the most common material used in PEM fuel cells, is used due to its low density, chemical stability and good electrical conductivity. It is commonly used as a bipolar plate material. Stainless steel has been a candidate for some of the components in the Radiator Stack designs. Stainless steel is a material with good corrosion resistance, reasonable thermal and electrical conductivity, and dimensional stability. The stainless steels [28] (SS316, SS317, SS316L) have bulk electrical resistivities of $740 \text{ n}\Omega \text{ m}$, thermal conductivities of $16.2 \text{ W}/(\text{m K})$, thermal expansion coefficients of $15.9 \text{ }\mu\text{m}/(\text{m K})$, and a density of $7.9 \text{ g}/\text{cm}^3$. Stainless steels have higher coefficients of thermal expansion and lower thermal conductivities than carbon and alloy steels. The thermal conductivities [35] of copper and aluminum are 390 and $200 \text{ W}/(\text{m K})$ respectively. Thus, stainless steel is not an ideal material in this respect, but has much better corrosion resistance because of relatively large amounts (>10 percent by mass) of chromium. The corrosion resistance of stainless steels is believed to result from the presence of a thin oxide film which forms on the metal surface. The chromium helps stabilize the oxide layer. However, it is this oxide layer that is blamed for high contact resistance, and thus poor electrical connections. Due to the density of stainless steels compared to graphite, extensive use of this material quickly increases stack weight. Copper was chosen as the best cooling panel material for the TERS97 design due to its high thermal and electrical conductivity.

A suitable coating on the metal fins may allow for use nearer in proximity to the membranes. Possible coating materials include graphite, conducting plastics and conducting rubbers.

Chapter 4

Performance Modeling Specifics of Radiator

Stack Designs

Modeling of the Radiator Stack Architectures was initiated in November 1995. Early work began considering only the stack, but it was quickly realized that thermo-fluid considerations dictate the size and geometry of many components. Thus, a system approach was required to determine mass flows and implications of stack changes on the overall system. Chapter 3 has laid out a general methodology. Chapter 4 presents some of the unique focuses of the Tube Bundle Heat Exchange design and the Tri-Stream Externally Manifolded RSA(TERS97).

4.1 Tube Bundle Heat Exchanger PEM Fuel Cell

4.1.1 Tube Configurations

The Tube Bundle Heat Exchanger PEM fuel cell design has many similarities with shell and tube exchangers. As such, it was advantageous to use the large body of knowledge available for heat transfer, pressure drop and manufacturing.

Shell and tube heat exchangers were found to come in the following standard pitches [27,35]

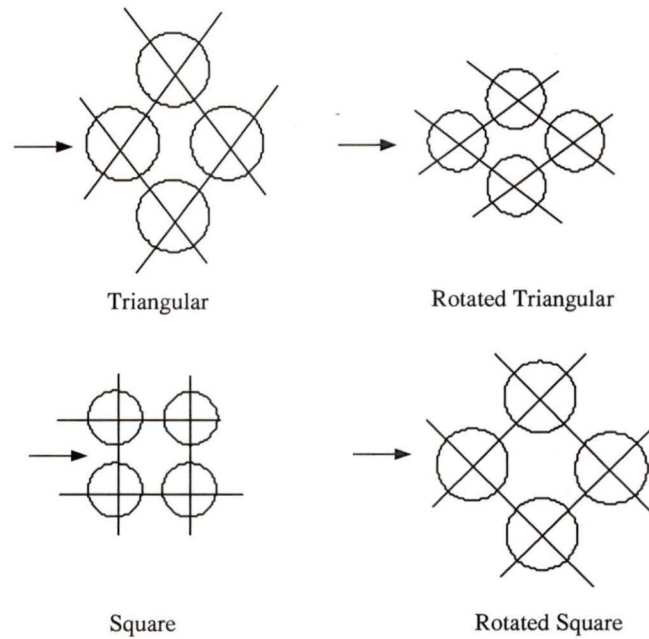


Figure 4.1: Standard Pitches for Shell and Tube Heat Exchangers

Most heat exchangers have a triangular pitch because it gives high heat transfer coefficients. Square pitch gives a lower pressure drop. Standard pitches found were modified due to some operational differences between fuel cell and heat exchange operation. Pitches can be represented by the tube diameter, X_L , X_d and X_t as shown in Figure 4.2.

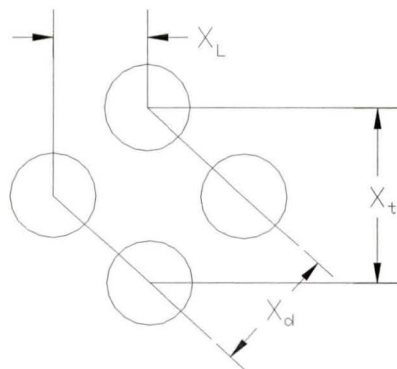


Figure 4.2: Tube Parameterization

X_L is the centre to centre distance between consecutive rows of tubes in the longitudinal direction. X_t is the centre to centre distance between tubes in the same row in the transverse direction. X_d is the same distance in the diagonal direction. Only two of the tube orientation variables need to be specified as

$$X_d^* = \left(\left(\frac{X_t^*}{2} \right)^2 + X_L^* \right)^{\frac{1}{2}} \quad (4.1)$$

These variables were normalized by dividing each by the tube diameter.

4.1.2 Resistivity

The i^2R losses are significant with this design compared to the traditional plate and frame design due to edge collection and the small cross-sectional areas of the tubes.

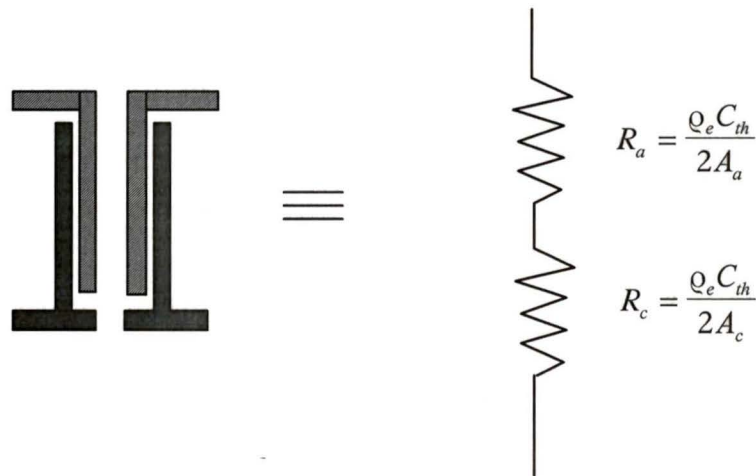


Figure 4.3: Tube Resistivity Model

The total resistance of each tube is calculated using

$$R_T = R_c + R_{mem} + R_a \quad (4.2)$$

where ρ is the electrical resistivity of the electrodes, and A_a and A_c are the cross-sectional areas of the anode and cathode respectively. The areas are calculated as follows

$$A_a = \pi \left(\left(D_{mem} - \frac{t_{mem}}{2} \right)^2 - D_i^2 \right) \quad (4.3)$$

$$A_c = \pi \left(D_i^2 - \left(D_{mem} + \frac{t_{mem}}{2} \right)^2 \right) \quad (4.4)$$

The additional power losses due to the double edge collection can then be approximated based on the geometry and the number of tubes. This was early work, and contact resistance was not known to be a great concern. Only bulk resistivities were considered.

4.1.3 Heat Transfer

Zukauskas reviewed the work of various investigators in the area of heat transfer [35] and proposed the following correlation for the heat transfer coefficient for flow across tube bundles

$$\frac{h_m D_t}{k_{air}} = c_2 Re^{max} Pr^{0.36} \left(\frac{Pr}{Pr_w} \right)^n \quad (4.5)$$

where Pr_w is the Prandtl number evaluated at the wall temperature, and $n=0$ for gases, and $1/4$ for liquids. This is valid for $0.7 < Pr < 500$ and more than 20 rows of tubes. For gases, the properties are evaluated at the film temperature, and the viscosity correction factor is $\left(\frac{Pr}{Pr_w} \right)^n$. The heat transfer coefficient h_m is then used to determine the amount of heat rejected and c_2 is found using correlations with experimental data.

4.1.4 Pressure Drop

Knowledge of the Reynolds number determines the flow characteristics which can be used to predict heat transfer and pressure drop. For tube bundles, the Reynolds number is defined as

$$Re = \frac{\rho_{air} u_{max} D_t}{\mu_{air}} \quad (4.6)$$

The minimum cross-section and the volumetric flow rate determines the maximum flow velocity. The minimum cross-section can occur in two different orientations, either the transverse or the diagonal direction depending on the orientation of the tubes.

Pressure drop due to fluid friction for flow across tube bundles has also been correlated by Zukauskas [35] in the form

$$\Delta P = \frac{f N_{tube\ rows} G_{max}^2 Z}{2 Q_{air}} \quad (4.7)$$

where f is the Darcy friction factor, G_{max} is $Q_{u_{max}}$, $N_{tube\ rows}$, and Z is a correction factor for effects of tube bundle configuration. The maximum mass flow velocity is a key variables in calculating pressure drop.

4.1.5 Fins

Circular fins were examined as a method of increasing the tube cooling surface area. The number of fins per tube is specified using the fin pitch, P_{fin} . The fin pitch is equivalent to a number of fins per unit length.

Fins decrease the minimum cross-sectional area as they occupy space in the tube bundle. However, the tradeoff is improved heat transfer which reduces the amount of air required. Fins are considered because the heat transfer coefficient (h_m) is low. Heat transfer at the fin tips is included. The length of the fins is calculated as a percentage of the distance to the neighboring tubes. For example, a length of 50 percent would extend fins half-way to nearby tubes.

4.1.5.1 Results

The Tube Bundle Heat Exchanger fuel cell designs considered are likely to have entrance, exit and edge effects influencing pressure drop and heat transfer calculations, as the tube height and tube diameter are on the same order of magnitude. The tube height is kept

small to limit current and minimize associated ohmic losses. The following analysis is done neglecting edge effects, although considering their possible influence.

For calculations, the inlet air temperature was assumed to be 25°C, and the tube surface constant at 85°C. Model results indicated that the best heat transfer is obtained when the tubes are packed as close as possible in both the longitudinal and transverse directions. Outlet temperatures of greater than 70°C were obtained with a closed-packed arrangement at the expense of pressure drop. Outlet temperatures of 47°C were obtained with a more modest design.

The designs can be better classified by looking at power densities. Two designs were selected as being representative of two extremes, a design with close-packed tubes, and another with spaced tubes. A 400 mm x 300 mm area footprint was used for the stack comparison. The following table allows for a comparison [36,37].

Table 4.1: Comparison of Two Design Extremes without Fins

| | Spaced Design | Packed Design |
|----------------------------|---------------|---------------|
| Number of tubes | 198 | 989 |
| Outer tube diameter (mm) | 15 | 8 |
| Inner tube diameter (mm) | 5 | 3 |
| X_L | 19.5 | 8.8 |
| X_d | 22.5 | 12.0 |
| Stack Power Density (W/l) | 160 | 400 |
| Stack Power Density (W/kg) | 150 | 320 |

As smaller tube diameters lead to improved power densities, the packed design dimensions were only constrained by manufacturing limitations. The addition of fins to the designs does not influence the amount of power produced, therefore the volumetric power density remains unchanged. However, this weight increase decreases gravimetric

power density. As expected, decreasing the diameter of the tubes by a factor of k , increases both the volumetric and gravimetric power densities by k .

The fins were found to be most effective in the spaced design, as the fins were able to be much larger, due to the increased spacing of the tubes. With the addition of 3 fins per tube, the effective cooling surface area was increased by 60 percent. In this case the outlet temperature was increased from approximately 47°C to 56°C. With packed design, 2 fins were added to shorter tubes. This only increased the effective cooling surface area by 19 percent. Due to tube packing, the fins were substantially shorter. The addition of fins to the packed design increase the outlet air temperature by only 2°C.

In both cases, the addition of fins decreases the amount of air required, and reduces required fan power. A significant decrease in flow velocity is observed with the *spaced design* with fins. With the *packed design*, the addition of small fins did not influence the flow characteristics substantially.

4.2 Cooling Panel Analysis of Tri-Stream External Manifold RSA Design (TERS97)

4.2.1 Cooling Panel Analysis

Two of the greatest concerns with a high performance air-cooled PEM fuel cell stack are ensuring adequate cooling and minimizing temperature gradients over the active cell area. Cooling panels in TERS97 are used to reject heat, but due to their multi-functionality, correct dimensioning is crucial. The cooling panel design was investigated experimentally, in areas of heat transfer and pressure drop, to validate predicted results. Surface roughness was investigated as a method of improving and controlling the local heat transfer coefficient, but no experimental work was done in this area.

The key dimensions of the cooling panel are the fin thickness, fin height and fin wavelength. These are shown in a cooling panel cross-section in Figure 4.4. An additional shape parameter is used for structural analysis to adjust the panel stiffness with vertical loadings. The top and bottom plate thickness, and method of assembly, also effect panels characteristics.

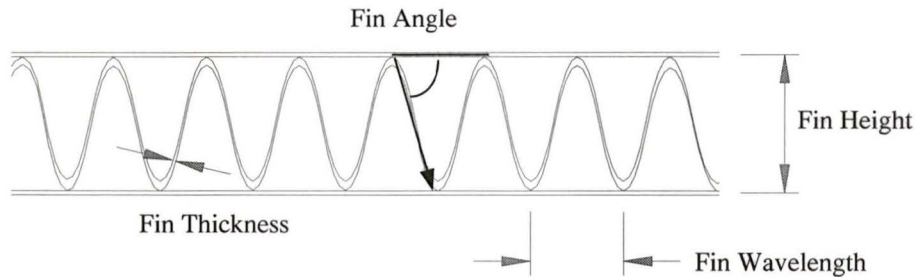


Figure 4.4: Parameterization of Cooling Panel

For simplicity, the channels were modeled as smooth-wall triangular ducts.

Cooling panels were manufactured using copper. Good electrical and thermal contact between the fin and support plates was ensured by soldering the materials together. Due to availability, it was decided to use an existing available radiator fin design with dimensions similar to those desired. A comparison is shown in Table 4.2.

Table 4.2: Comparison of Initial Design and Actual Fin Dimensions

| | Design | Actual |
|----------------|--------|----------|
| Fin Height | 9.5 mm | 8.7 mm |
| Fin Wavelength | 6.5 mm | 5.0 mm |
| Fin Thickness | 0.5 mm | 0.076 mm |
| Fin Angle | 70.1° | 73.8° |

In addition to the slightly different dimensions, the fins had slots (louvers) in the fin walls. The existence of the slots changes the thermo-fluid characteristics compared with the same design with no slots. The ducts now have multiple inlets and outlets along their

length. This makes analysis more complex. The slot frequency was 4 slots per inch. For the analysis, basic relations for non-slotted ducts were altered to account for this difference. Validation of these altered equations was then done by experiments.

4.2.2 Test Apparatus

The testing of a single cooling panel was done in a large air duct. Figure 4.5 shows a schematic of the testing arrangement.

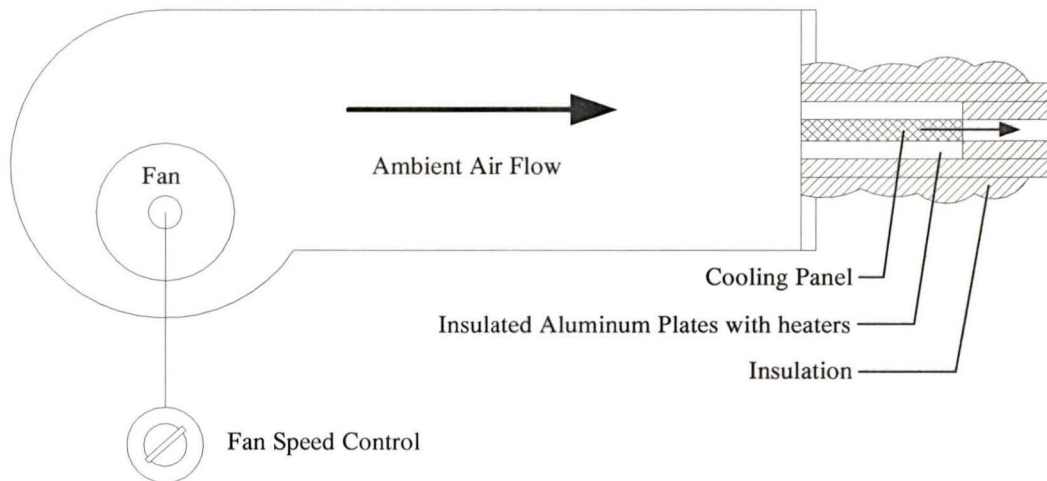


Figure 4.5: Schematic of Cooling Panel Test Apparatus

A variable-speed fan was used to propel ambient air along a 35 cm x 35 cm duct cross section. The exit end of the duct was adapted using a custom end plate. A slot in the end plate allowed a single cooling panel to be inserted. The cooling panel was then sandwiched between two aluminum plates, each containing a variable power cartridge heater. To minimize undesired heat loss to the environment, the complete assembly was well-insulated.

Temperature measurements were taken at various points. The temperatures of interest are the inlet and outlet air temperature, and the temperature profile of the cooling panel at different locations along the direction of flow. Thermocouples were used at locations shown in Figure 4.6 in contact with the cooling panel's upper flat plate surface.

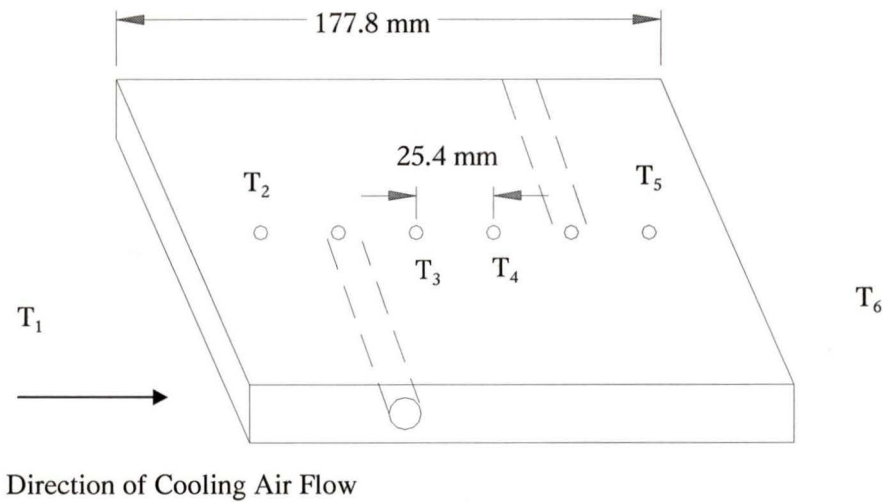


Figure 4.6: Temperature Measurement Locations in Relation to the Aluminum Block

Type K and J thermocouples were used to measure temperature.

A series of tests was conducted on the cooling panel. A test consisted of setting heater power and fan speed (volumetric flow rate), and measuring the dependent variables such as temperatures profiles and pressure drop. Each test was run for at least 30 minutes to ensure that steady-state had been achieved. Assuming no additional heat loss to the surroundings, by energy conservation, the heater power equals the cooling power of the panel.

4.2.3 Heat Transfer

As outlined in Section 3.9, a logarithmic mean temperature difference (LMTD) method was used to calculate the temperature of the exiting air stream. The heat transfer is determined based on the Nusselt number for smooth triangular ducts. For laminar flow, a constant Nusselt number of 4.205 is assumed. This applies to laminar flow in equilateral triangular ducts with 3 rounded corners using the “H-1” boundary condition [21] (isothermal wall). Verification of this assumption was done using the wall conduction parameter (K), where K is defined as

$$K = \frac{k_a s}{k_w t_w} \quad (4.8)$$

and k_a and k_w are the thermal conductivities of the air and wall respectively, s is the distance between the corner and midpoint of the wall, and t_w is the wall thickness. For all the cooling fins considered, $K < 0.002$ which satisfies the H-1 boundary condition.

For turbulent flow, a correlation has been previously curve-fit from available data on Nusselt numbers [21] for fully developed turbulent flow in smooth equilateral triangular ducts. The result is as follows

$$\log Nu = 0.755 \log Re - 1.434 \quad (4.9)$$

This equation gave conservative model results compared with other heat transfer correlations for turbulent flow with more general geometries, so it was retained.

With a smooth triangular duct, the expected transition from laminar to turbulent flow should begin at a Reynolds number of approximately 2000 [21]. This is the critical Reynolds number (Re_c). It was expected that the addition of slots to the fin channels would change the point where transition occurs due to flow disruption. Basically, creating turbulent conditions at lower Reynolds numbers. Thus, the validity of the laminar equations were in doubt over normally expected laminar conditions.

An important parameter which results from the heat transfer analysis is the temperature change of the cooling air across the cooling panel. This temperature change, along with the mass flow rate, effectively determines the amount of cooling taking place. For model validation, the uniform fin temperature was taken as the average experimental panel temperatures.

Due to the expected *simulated* turbulent conditions at Reynolds numbers less than 2000, the turbulent correlation was used for Reynolds numbers greater than 800. The laminar

correlation was used for lower Re. The preliminary results are plotted in Figure 4.7. The maximum temperature difference between experimental and model results was found to be 8.9°C. This occurred at a power setting of 249.7 W, and a cooling flow rate of 4.85 g/s, with an average fin temperature of 86.9°C.

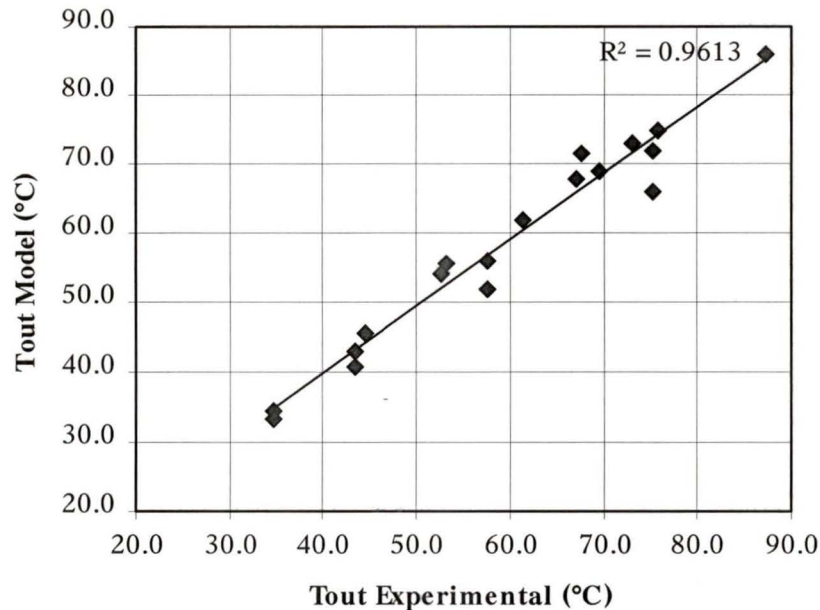


Figure 4.7: Comparison of Initially Predicted and Experimental Outlet Air Temperature

Due to the allowance of both laminar and turbulent flow conditions, an interesting situation exists for cooling with flow rates near the “critical” Reynolds number. Unfortunately, it leads to two solutions, for laminar and the other turbulent. For instance, to maintain 169.4 W of cooling at an average fin temperature of 65.7°C and assuming a transition Re of 800, the two mass flows of 5.23 g/s (Re=782) and 5.98 g/s (Re=897) satisfy conditions. For instances where the model gives two solutions, the turbulent results gave more favourable results although both are plotted in Figure 4.7. Allowing a transition to occur at Re = 800 is a mathematical idealization. However, a transition of this form in a real system likely does exist at some point, and may lead to control difficulties when attempting to maintain a constant fin temperature with varying heat rejection requirements.

4.2.4 Validation of Flow Conditions

For laminar flow conditions, the Nusselt number is expected to be constant. Thus, by examining a plot of experimental Nusselt number versus flow rate, any transition points should be apparent. Figure 4.8 shows a plot of experimental Nusselt number versus model Reynolds number.

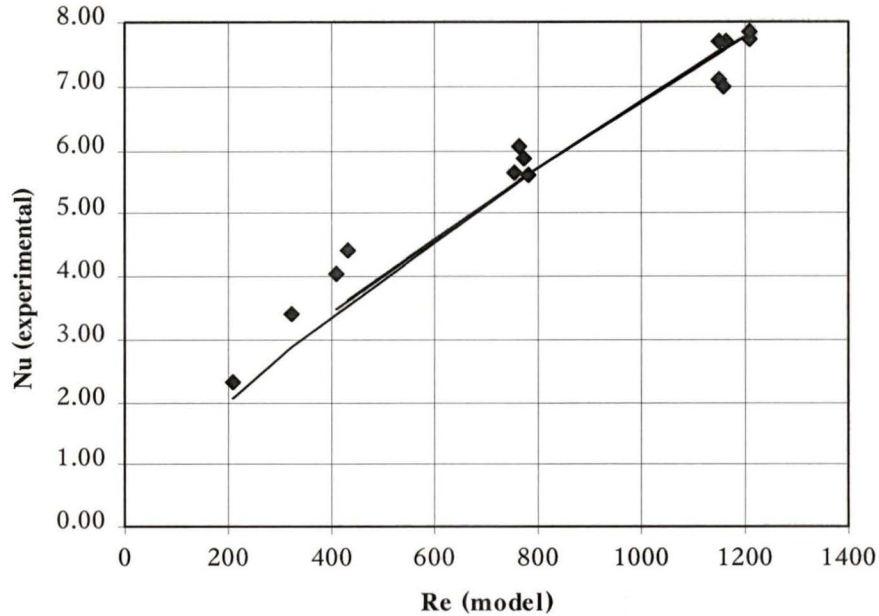


Figure 4.8: Plot of Nusselt Number (Exp.) versus Re (Model)

As shown, the Nusselt number decreases, with decreasing Reynolds number. No sections of the plot appear to be horizontal, thus it can be concluded that using the laminar heat transfer equations is invalid. Thus, the turbulent heat transfer equation (Equation 4.9 as plotted) was then used over the entire flow regime.

This change was found to improve the accuracy of the predictions. The average error between the experimental and model outlet temperatures decreased from 2.1°C to 1.6°C. A comparison of model and experimental outlet temperatures is shown in Figure 4.9.

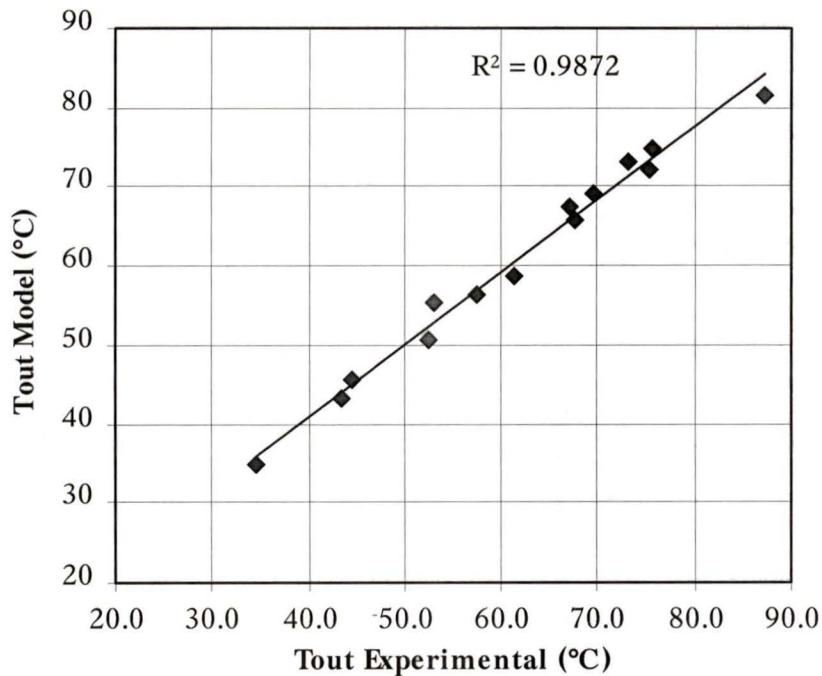


Figure 4.9: Comparison of Improved Model and Experimental Outlet Air Temperature

The maximum temperature difference was reduced from 8.9°C to 5.6°C. Parameterization of Equation 4.9 was attempted using an equation of the same form in an attempt to improve the results.

$$\log Nu = a \log Re - b \quad (4.10)$$

The coefficients a and b were then varied. It was found that the coefficients of $a=0.755$ and $b=1.434$ were indeed optimum values, as the least-squares error between model and experimental temperature results could not be reduced.

The Nusselt numbers for the experimental results and the improved model (turbulent only) are presented in Figure 4.10.

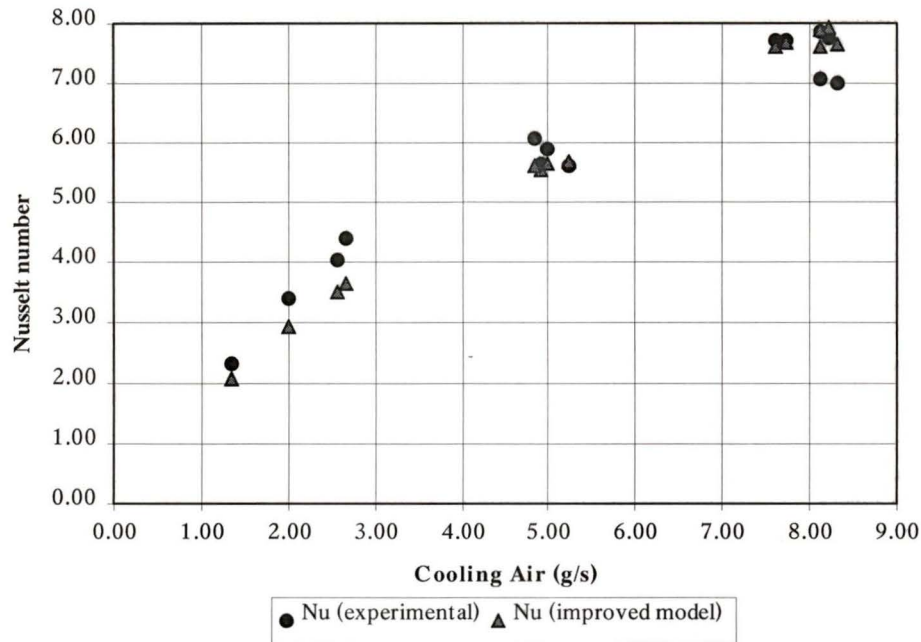


Figure 4.10: Nusselt Number versus Cooling Air Flow Rate

4.2.5 Pressure Drop

Equation 3.21 was used as a basis for pressure drop analysis.

$$\Delta P = \frac{f L Q \bar{u} (sf)^2}{2 D_{hyd}} \quad (3.21)$$

Where, for smooth triangular ducts, the friction factors are as follows

laminar:
$$f = \frac{13.333}{Re} \quad (4.11)$$

turbulent:
$$f = 0.158 Re^{-0.25} \quad (4.12)$$

These equations are for smooth continuous ducts with one inlet and one outlet. Due to the significant effects of the slots, and less critical consequences of manufacturing misalignment and error, a safety factor of 3 was thought reasonable. This effectively triples the constant coefficients given by Equations 4.11 and 4.12. Due to the required physical length of the panel, and the available, much shorter in length cooling fins, 3 rows of fins were required to span the panel length of 178 mm. The cooling panels were assembled by soldering the copper cooling fins in between 2 flat copper sheets. Due to

misalignment of the rows inside of the panel and differences between channels, the pressure drop was expected to be higher than for an ordinary channel. The initial model results and experimental results are shown in Table 4.3.

Table 4.3: Cooling Panel Experimental and Initial Model Pressure Drop Results

| Test # | Exp. Mass Flow (g/s) | Experimental Pressure Drop (Pa) | Model Pressure Drop (Pa) |
|--------|----------------------|---------------------------------|--------------------------|
| 1 | 1.34 | 13 | 5 |
| 2 | 2.02 | 25 | 7 |
| 3 | 2.57 | 25 | 9 |
| 4 | 2.67 | 25 | 10 |
| 5 | 4.85 | 112 | 41 |
| 6 | 4.92 | 112 | 33 |
| 7 | 4.99 | 112 | 36 |
| 8 | 5.22 | 112 | 34 |
| 9 | 7.61 | 212 | 77 |
| 10 | 7.72 | 212 | 77 |
| 11 | 8.11 | 212 | 72 |
| 12 | 8.12 | 237 | 84 |
| 13 | 8.22 | 237 | 83 |
| 14 | 8.32 | 237 | 74 |

As shown, the experimental pressure drop was still 300 percent higher than expected results. Curve-fitting the results was then done using the turbulent only Equation 4.12 as a basis. The safety factor of 3 was then removed by integrating it into the new equation. The new relation determined for the friction factor is shown

$$f = 1.512 \text{Re}^{-0.25} \quad (4.13)$$

The experimental, original model with laminar and turbulent considerations, and turbulent only model results are shown as a function of mass flow in Figure 4.11.

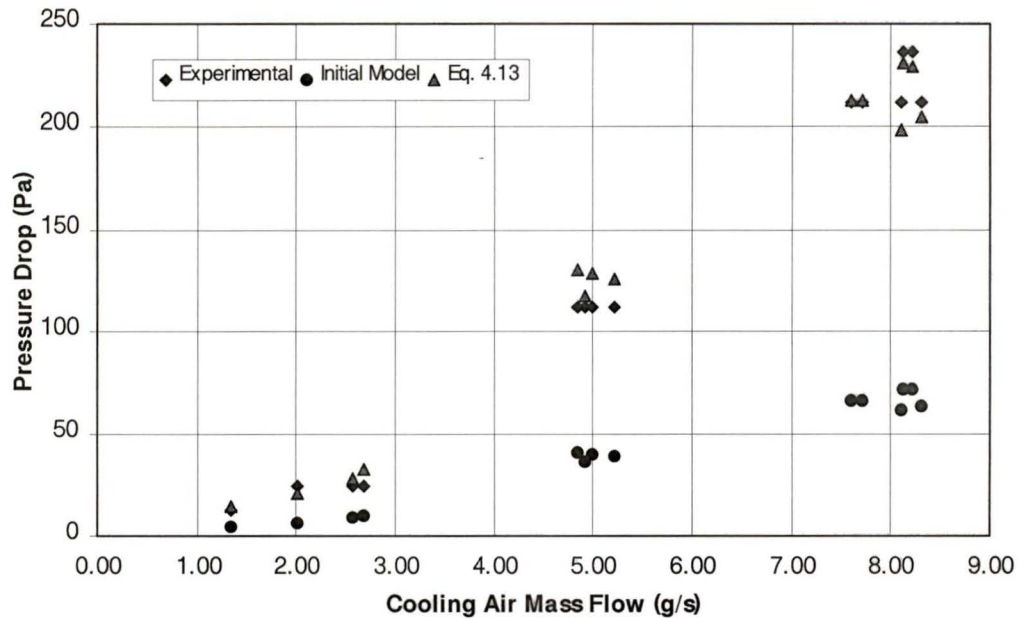


Figure 4.11: Cooling Panel Pressure Drop vs. Cooling Air Mass Flow

The coefficient in Equation 4.13 is considerable different from Equation 4.12. Equation 4.13 is to be used in the construction of the prototype. However, Equation 4.12 should be used for new fins without slots in future iterations.

4.2.6 Cooling Panel Temperature Gradients

One of the concerns in utilizing an air-cooled stack is a large temperature gradient. In the TERS97 design, temperature gradients are present in the direction of cooling air flow. The test set-up gave an excellent opportunity to review this issue.

As shown in Figure 4.6, four thermocouples were used to record the temperature of the cooling panels upper plate surface. The results are shown in Figure 4.12.

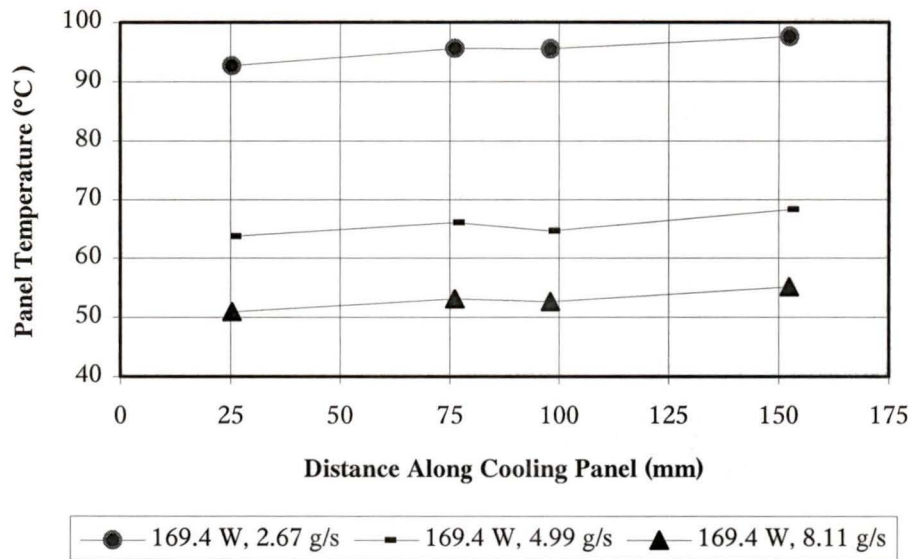


Figure 4.12: Cooling Panel Temperature Gradient for Rejecting 169.4 W

The maximum temperature difference, from inlet to outlet, for the 3 tests at 169.4 W, was 4.9 °C. The experimental results shown have an accuracy of +/- 0.5°C. Aluminum was chosen to house the electric heaters because of its high thermal conductivity and good-machinability. This conductivity is beneficial in that it helps evenly distribute the heat flux to a large portion of the cooling panel surface, thus simulating heat removal in an operating fuel cell. Figure 4.13 shows the average temperature difference in the panel using $T_5 - T_2$ as a function of the amount of heat rejection.

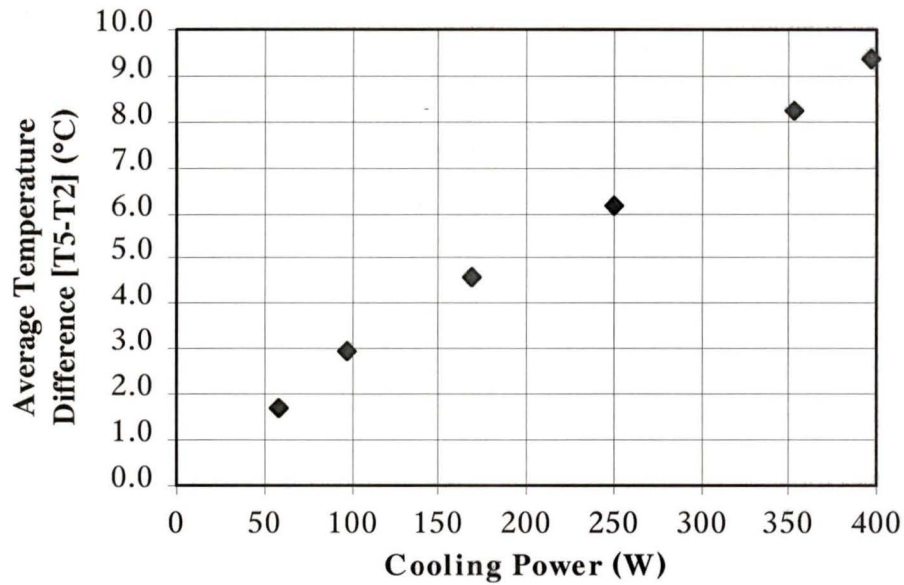


Figure 4.13: Average Temperature Difference (T_5-T_2) for Various Cooling Powers

The current fin construction likely increases the temperature gradient in the direction of cooling air flow due to three rows of short cooling fins. This makes conduction of heat from warm to cool front regions difficult due to a lack of thermal communication. Heat conduction can only take place in the thin top and bottom copper plates and the aluminum blocks in the case of the test set-up. Using a longer one-piece fin, would help reduce temperature gradients. Temperature gradients in the stack are a concern because of uneven operation over the active area. For instance, water vapor in the cell may condense in cooler regions causing flooding and poor performance in that area.

4.2.7 Surface Roughness

To help combat the effects of temperature gradients, surface roughness was considered an option to improve local heat transfer. This improved heat transfer performance comes at the expense of pressure drop [21].

Duct wall roughness has little effect on laminar flow. However, it has a strong effect on turbulent flow. Re_ϵ is the most convenient parameter to identify various flow regimes from the standpoint of the roughness influence, and is defined as

$$\text{Re}_\varepsilon = \frac{\varepsilon u}{\nu} \quad (4.14)$$

where ε is the average roughness height, u is the friction velocity [21], and ν is the kinematic viscosity. The completely rough regime occurs with $\text{Re}_\varepsilon > 70$. This translates to a surface roughness *element* height of 0.11 mm for the cooling panel design's flow conditions.

Surface roughness has two distinct influences on heat transfer. First, the duct surface area is increased, and second, the heat transfer coefficient is increased. The latter effect occurs because of the change in turbulent pattern close to the wall. This increase in the heat transfer coefficient is accompanied by a proportionally larger increase in the friction coefficient. This results in the heat transfer per unit power consumption being lower for rough surfaces. Norris suggested the following empirical correlation

$$\frac{Nu}{Nu_s} = \left(\frac{f}{f_s} \right)^n \quad \text{for } \frac{f}{f_s} < 4 \quad (4.15)$$

where $n = 0.68 \text{Pr}^{0.215}$ for $1 < \text{Pr} < 6$. For $f / f_s > 4$, heat transfer was no longer improved [21]. However, the Prandtl number for air in our cooling temperature range is 0.7. Thus, the validity of the equation is questionable.

4.2.7.1 Surface Roughness Findings

Surface roughness was examined using the TERS97 performance model. Its influence was as anticipated. It improved heat transfer and increased pressure drop. The improved heat transfer manifested itself in a higher outlet temperature for the cooling air. Thus, less cooling air is required and the channel air velocity is decreased [38].

4.3 System Analysis of Tri-Stream External Manifold RSA Design (TERS97)

A good method of examining a fuel cell system performance is to look at a complete breakdown of all energy flows. This includes the gross raw power output, and the power

used to power ancillaries. Also, cooling mechanisms should be examined thoroughly. Figure 4.14 shows the results for the TERS97 design.

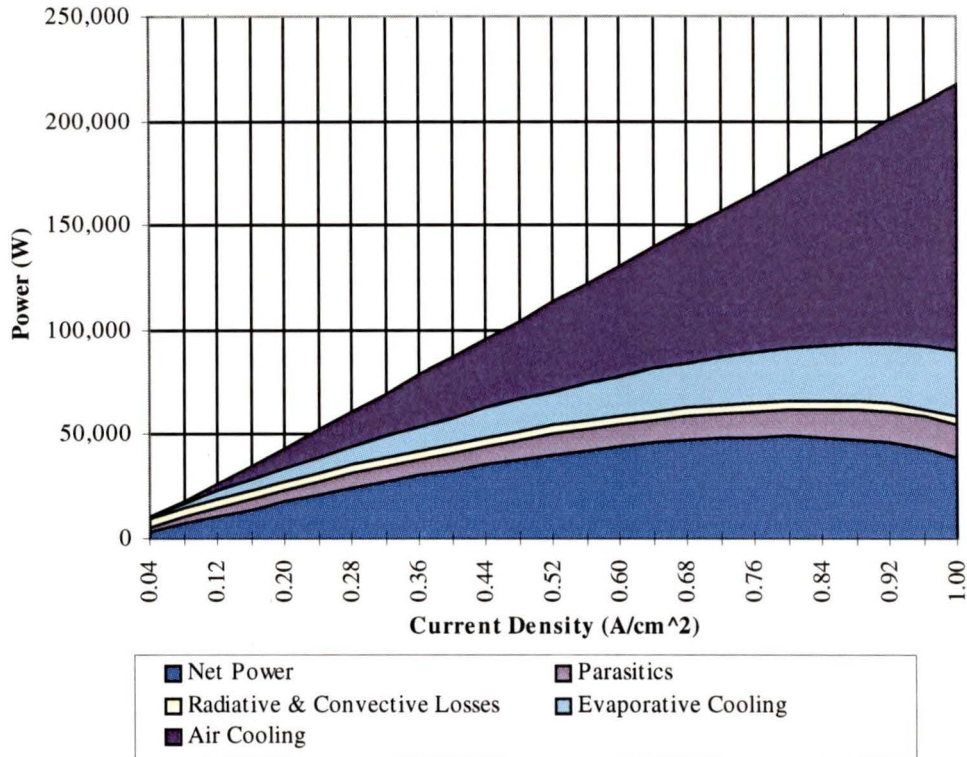


Figure 4.14: Energy Flows as a Function of Current Density

The bottom shaded area represents net stack output power. The area above represents the power loss due to the parasitic loading of the air compressor, cooling fan and humidification water pump. Also represented, is passive cooling due to radiation and natural convection. This cooling power is relatively small when compared to the other cooling quantities. The higher heating value of the fuel cell reactions is used in the analysis. Therefore, it is assumed that the product of the reaction is liquid water. As most product water exits the stack in the vapour state, this is considered a cooling effect due to analysis convention. Because of water's large latent heat of vaporization, this is a significant effect. The remainder of the cooling load is satisfied by the cooling air through forced convection. The determination of the cooling load for the forced convection is the driving force for this analysis.

As shown, at lower current densities ($< 0.08 \text{ A/cm}^2$), the stack cooling load is satisfied by passive cooling mechanisms. Therefore, at these low current densities the stack temperature is not maintained.

The parasitic loads, combined in the previous figure, may be broken down by their respective components. The air compressor operates equally as in a water-cooled system, and is by far the largest parasitic load. The cooling air fan is a critical component to the effectiveness of the design. In water-cooled systems, a cooling fan is present to help move air over the large stainless steel radiator. Thus, a small allowance is available with the air-cooled option without exceeding the parasitic loading for the water-cooled option.

Additional performance curves are presented in Figure 4.15 for the ancillary equipment. As shown, the air compressor is by far the largest parasitic load consuming approximately 21 percent of gross power at peak power ($\sim 0.83 \text{ A/cm}^2$).

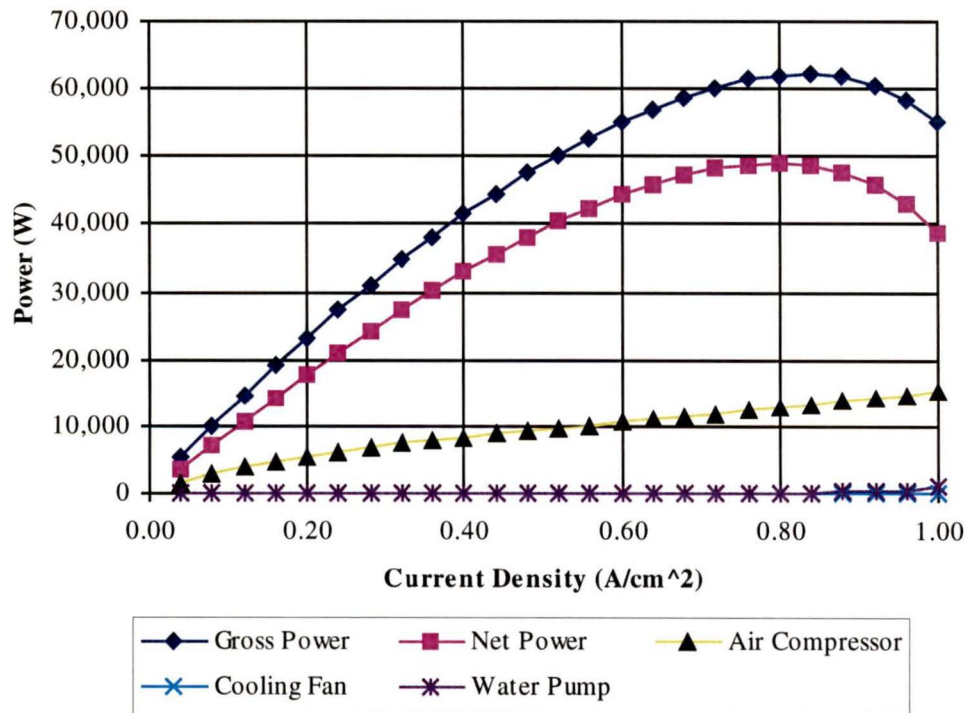


Figure 4.15: Performance of Ancillaries in TERS97

The cooling fan was found to have a relatively small electrical load, with less than 500 W consumed over desirable operating current densities. Due to cooling panel design, this parasitic load was kept relatively small. The humidification water pump was found to consume the least amount of power, less than 100 W over all current densities. This is due to the small water flow rates required.

4.4 Modeling of the Ballard - Daimler Benz NECARII System

In 1996, Germany's Daimler Benz presented *NECARII* based on the new Mercedes V-class mini-van. This was a follow-up to *NECAR* presented in 1993. These fuel cell systems were both developed through a joint venture between Ballard Power Systems and Daimler Benz.

NECAR was powered by Ballard's MK-5 stack, introduced in 1990. Operating at Ballard's standard conditions of 308 kPa_a for both hydrogen and the air, and a stoichiometry of 2.0 for air and 1.5 for hydrogen. A number of stacks, each producing 5 kW at an average cell voltage of 0.57 V were used as the power plant. This corresponds to a stack power density of 150 W/l or 130 W/kg, including an integral membrane humidifier.

The MK-7 stack was developed jointly by Ballard and Daimler Benz for *NECARII*. This stack occupies a volume of 31.9 l, produces a continuous power of 32 kW at an average cell voltage of 0.68 V[47]. Under similar high efficiency operating conditions, the stack delivers over 1000 W/l and over 700 W/kg [20]. Currently, this stack, along the GM "banded" stack, set the state-of-the-art power density targets for transportation PEM fuel cell technology. As such, it was important to model the *NECARII* system, so it could be used as a benchmark for the air-cooled designs.

The *NECARII* system (BD 95) is powered by 2 MK-7 stacks. Each stack has a length of 510 mm, a width and height of 250 mm, and contains 132 cells. This design was modeled using the same methodology developed for the air-cooled designs.

4.4.1 System Analysis

The energy flows for the *NECARII* system were also examined. The results are shown in Figure 4.16.

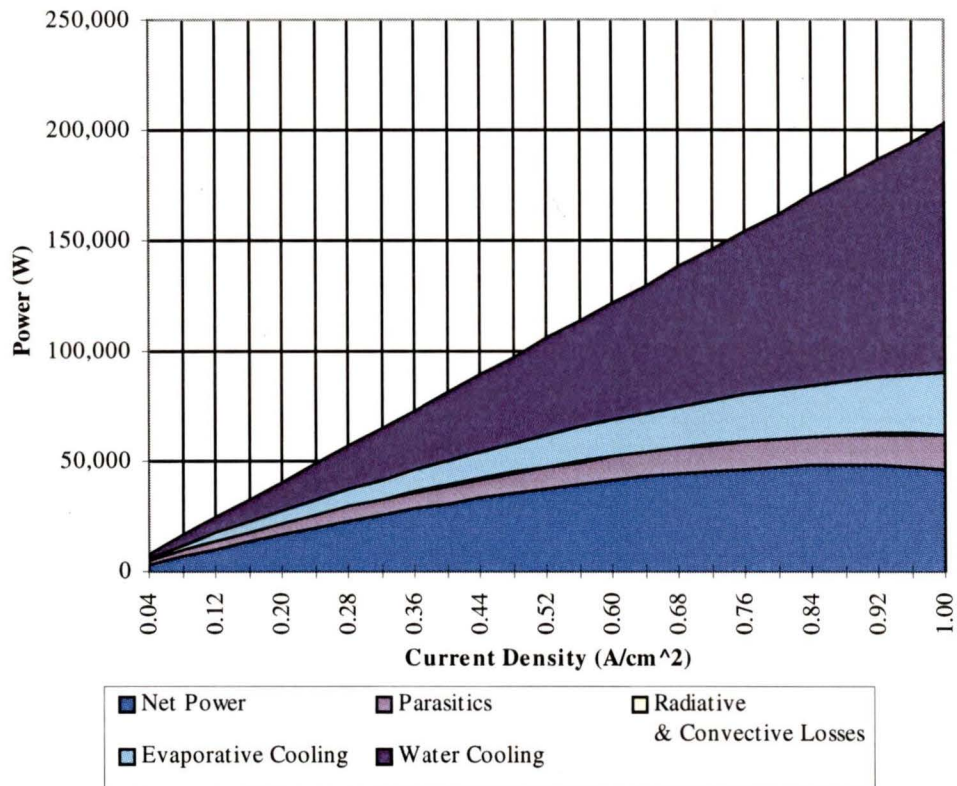


Figure 4.16: Energy Flows as a Function of Current Density

This plot is similar to the energy flow for the TERS97 design. The major difference is a smaller heat loss due to radiation and natural convection for the stack. The amount is approximately 1/10 of the value for the TERS97 design due to several reasons. The stack is approximately 1/6 of the size of the air-cooled design. Also, due to its location in the mini-van, under the back seat, the contribution of natural convection is much less.

The parasitic losses were found to be within 450 W of the TERS97 design for the complete range of current densities. The larger fan requirements for TERS97 were offset with the larger water pump requirements for BD 95. Still, the power requirements for each cooling fan and water pump component are less than 400 W, and much less significant than the compressor load which reaches close to 14 kW in both cases.

A specific area of interest was the power density for the membrane as results were not found in the literature. An area utilization of 83 percent was used for the Ballard-Daimler Benz design. This resulted in a power density of 467 mW/cm². This high utilization of cell area gives an active area of 519 cm². The TERS97 design, in its current form, has an active area of only 245 cm², total of 600 cells, and a power density of 423 mW/cm². Thus, the BD95 membrane has an output 10.6 percent higher than the TERS97 design. Due to the presence of higher temperature gradients, a longer current path, and more interfaces for the current to pass through in the air-cooled designs, a poorer polarization curve results as expected.

The parasitic loads for BD95, combined in the previous figure, may be broken down by their respective components. As shown, the air compressor is by far the largest parasitic load consuming approximately 21 percent of gross power at peak power (~ 0.96 A/cm²).

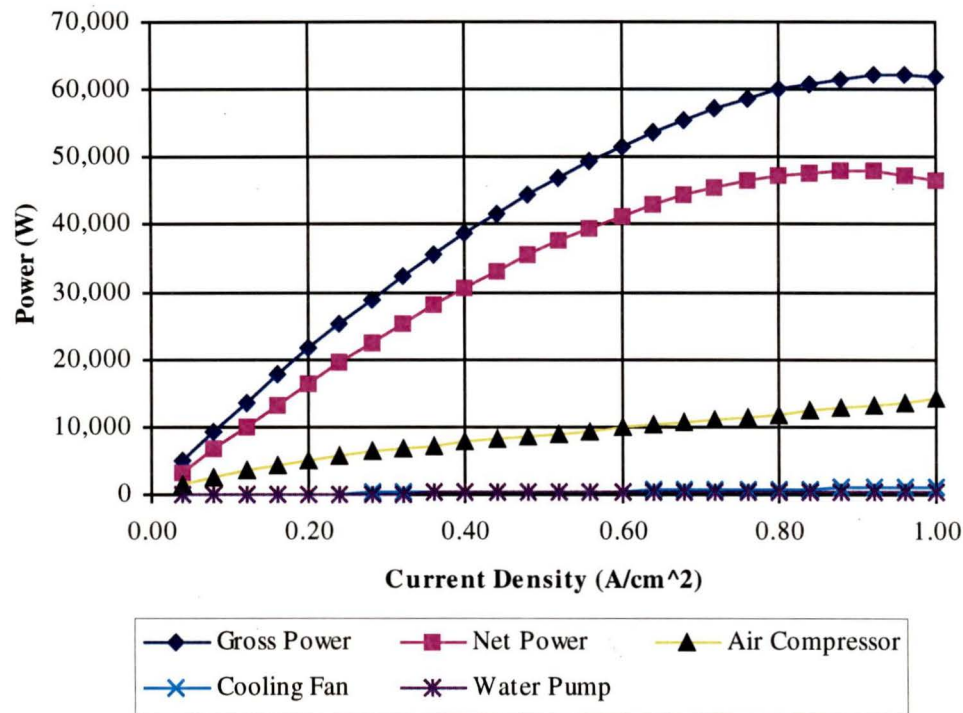


Figure 4.17: Performance of Ancillaries in BD95

The air compressor is by far the largest parasitic load. The radiator fan, used to move ambient air over the stainless steel radiator, was found to have a relatively small electrical load, with less than 400 W consumed over desirable operating current densities. It is assumed that the cooling water pump also provides make-up water for the humidification system.

4.5 Summary of Power Densities for Designs

All stacks and systems were compared having a gross stack output of 64 kW. In cases where a flat panel and waveboard design have been presented. The flat panel design is considered representative of the two designs. Data from Pasquill and Nahon [32] is used as a basis for some component masses and volumes. The issue of range of sizes available is not addressed as for mass production runs, required components could be manufactured. Therefore, linearized scaling is used where necessary.

All fuel cells require ancillaries for support. The fuel cell system may be broken down into: cooling system, reactant supply, stack, control system, drive, and miscellaneous. In the evaluation of the systems each area was considered individually.

4.5.1 Cooling System

For the ambient air designs the cooling and oxidant flows are satisfied by the same flow. For cooling of the air-cooled designs a 0.6 kW fan, external manifolding, and air filtering system have been included. Additional required items such as hosing and fittings are included in the miscellaneous section. Table 4.4 is a cooling summary.

Table 4.4: Cooling Summary

| <i>Cooling</i> | volume (L) | mass (kg) |
|-------------------------------|------------|-----------|
| Tube Bundle Heat Exchanger | 25 | 40 |
| Ambient Air Flat Panel | 25 | 40 |
| Tandem Air Flat Panel | 25 | 40 |
| TERS97 | 20 | 30 |
| Ballard - Daimler Benz (MK-7) | 103 | 94 |

Compared to the water-cooled Ballard - Daimler Benz system, the air-cooled systems are smaller in this area. However, a larger stack size results. Light-weight manifolding materials, such as Ultem®, are used to minimize the weight of the external manifolds.

4.5.2 Reactant Supply System

The reactant supply system provides humidified hydrogen and air to the stack. For the uni-pressure designs, the hydrogen pressure must be significantly reduced to near ambient stack oxidant pressure. As shown in Table 4.5, the tandem air and BD95 systems are the same. The system components included are: an air compressor, 2 water knockouts, hydrogen and air filtering systems, 2 humidifiers, and an ejector to allow the recirculation of hydrogen.

Table 4.5: Reactant Supply Summary

| <i>Reactant Supply</i> | volume (L) | mass (kg) |
|-------------------------------|------------|-----------|
| Tube Bundle Heat Exchanger | 95 | 88 |
| Ambient Air Flat Panel | 95 | 88 |
| Tandem Air Flat Panel | 114 | 110 |
| TERS97 | 114 | 110 |
| Ballard - Daimler Benz (MK-7) | 114 | 110 |

The ambient air systems do not have an air compressor. However, a larger humidifier is required. The air filtering system is included as a cooling system component. The details of hydrogen storage have not been included.

4.5.3 Stack (Electro-Chemical Engine)

The stack volumes and masses for a 64 kW output are shown in Table 4.6.

Table 4.6: Fuel Cell Stack Summary

| <i>Stack</i> | volume (L) | mass (kg) |
|-------------------------------|------------|-----------|
| Tube Bundle Heat Exchanger | 160 | 200 |
| Ambient Air Flat Panel | 570 | 955 |
| Tandem Air Flat Panel | 475 | 955 |
| TERS97 | 380 | 210 |
| Ballard - Daimler Benz (MK-7) | 64 | 91 |

As shown, the air-cooled designs are all larger than the water-cooled BD95 option. However, further global optimization will improve results.

4.5.4 Control and Drive Systems

Control systems are required for automatic operation. Normally, cooling and fueling systems require logic control of pumps, compressors, and hydrogen flow. Due to the relatively insignificant size and mass of this system, no notable changes are expected. An allowance of 5 litres and 10 kilograms is included for control equipment.

The drive system consists of a large electric motor. Power conditioning equipment is also required. In all cases the drive is expected to consume 115 litres and 73 kg.

4.5.5 Miscellaneous

Additional equipment for the powertrain and piping, ducting and bracketing are all required. For the BD95 system, an allowance of 1.2 kg/ kW was included for these components. For the RSS designs, this value was increased to 2.0 kg/kW due to the possibility of additional in-vehicle manifolding and other unknowns. The volume of these components was not considered.

4.5.6 System Power Densities

By summing the totals for the fuel cell sub-systems, and dividing these values by the gross stack output, the system power densities are attained. Table 4.7 gives an estimate on the total system size and system power densities.

Table 4.7: System Power Densities

| <i>System</i> | volume (L) | mass (kg) | W/l | W/kg |
|-------------------------------|------------|-----------|-----|------|
| Tube Bundle Heat Exchanger | 405 | 534 | 158 | 120 |
| Ambient Air Flat Panel | 815 | 1289 | 79 | 50 |
| Tandem Air Flat Panel | 739 | 1311 | 87 | 49 |
| TERS97 | 639 | 556 | 100 | 115 |
| Ballard - Daimler Benz (MK-7) | 406 | 450 | 158 | 142 |

4.5.7 Conclusions

Of the air cooled designs considered, the Tube Bundle architecture appears to have the best results. However, the large stoichiometries required with ambient air designs with high power densities make stable operation unlikely. The TERS97 design is the current focus of work, and has power densities within reach of the Ballard - Daimler Benz system. The volumetric and gravimetric system power densities need to be improved by 58 W/l and 27 W/kg, respectively.

The TERS97 system is shown to be a feasible alternative to the best existing technology. Future improvements through optimization of design variables, and options such as:

- thinner gas manifolds
- smaller support columns
- thinner end and bus plates
- smaller cooling panels

will help improve power densities and help close, or eliminate the gap. The results presented in Section 4.5 are expected to have an accuracy of +/- 25% due to estimated membrane performance, effects of contact resistance and sizing of components.

4.6 Software Implementation of the PEM Fuel Cell Performance Model

All system modeling was done in the FORTRAN programming environment. Details on the program modules and their interaction follow.

4.6.1 Function Modules of the Program

The program routines and their functions are shown in Table 4.8.

Table 4.8: Program Routines and Their Function

| Routine | Function |
|------------------|---|
| basepolarization | defines the base polarization curve based on operating conditions |
| dimensioning | defines stack architecture |
| findimensioning | defines geometry and frequency of the conducting and cooling elements |
| air_h2_plate | characterizes gas delivery plates |
| activearea | calculates cell active area |
| res_powerout | determines "extra losses" due the stack geometry - using bulk resistivity and geometry (contact resistance neglected) |
| approxcooling | determines an approximate cooling air flow rate to be used in future iterations / calculations |
| flowstreams | reactant and humidification water flows are calculated |
| energy_balance | energy balance for system is determined as shown in Chapter 3 |

| | |
|---------------|---|
| heat_transfer | air cooling heat transfer for cooling panel is solved by iteration |
| pressure_drop | pressure drop and fan power are determined for the cooling panel elements |
| weight | weight of stack determined (system weight determined independently) |
| powerdensity | stack power densities are determined using gross stack power output |
| output | output is arranged into a MATLAB file. |

Three subroutines also are involved. These are shown in Table 4.9.

Table 4.9: Program Sub-routines and Their Function

| Routine | Function |
|---------------|--|
| airproperties | calculates various air properties as a function of temperature |
| watertotal | calculates amount of water to completely saturate a given air flow rate at a temperature and total pressure |
| hwatertotal | calculates amount of water to completely saturate a given hydrogen flow rate at a temperature and total pressure |

The program variables are not included due to their number.

4.6.2 Program Structure Flowchart

The program structure with the main routines is shown in Figure 4.18.

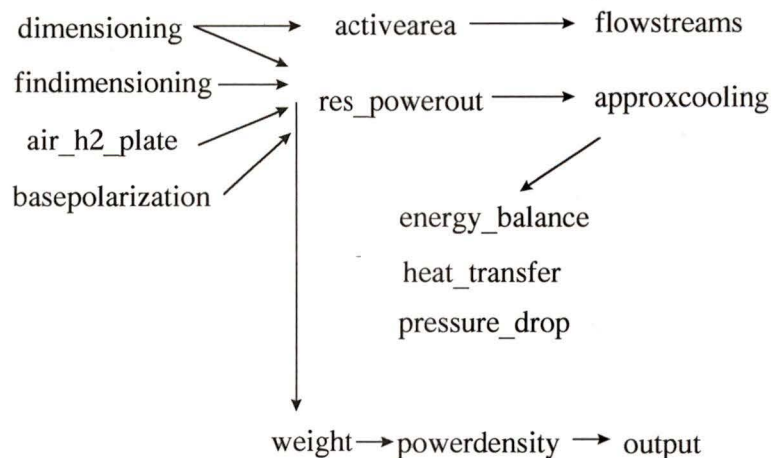


Figure 4.18: System Modeling Flowchart

The program is linear in nature, although all calculations are done over 25 different current densities. Iterations are necessary to find a solution in the *heat_transfer* routine

4.6.3 Comments on Program Use

The program is composed of three parts: stack definition, simulation of system operation, and output of key results. From a user's perspective, the various stack, gas delivery and cooling panel dimensions, and how they affect the system results, are of great interest. The system results presented in this thesis are for well-designed, but not optimal stack dimensioning.

The many designs presented in this thesis led to the creation of many independent programs. However, they all have a similar structure. Each program, specifically the stack definition section, defines a particular architecture. Where possible, variables are linked, thus creating dependent variables and a parametric tool. This allows the influence of the independent variables on the system to be easily monitored. In the case of examining the surface roughness (Section 4.2.7) of cooling panel fins, a supervisory program was constructed to step variables from minimum to maximum values in set increments. Expanding this further to include all independent variables leads to an optimum system design tool.

Chapter 5

Flow Field Design For Reactant Delivery Plates

5.1 Introduction to Flow Field Design

Flow field plates are generally solid graphite plates which represent most of the solid structure of today's PEM fuel cells. Traditionally, these separator plates direct the reactants and cooling water to the necessary parts of the fuel cell stack. For the Radiator Stack Architecture TERS97 design, oxidant and hydrogen delivery plates are required for use in physical and working prototypes.

Ballard Power Systems currently use high density graphite as a bipolar plate material. Other options such as metals and conductive plastics [53] may be available in the near future. Ballard utilizes a serpentine path for reactant flows which gives long path length and good plate coverage. These flow field patterns are machined using CNC machines. The cost of materials, pre-treatment of the graphite plates, and long and difficult machining makes up a significant portion of the cost of a fuel cell stack.

5.1.1 Screen Printing Manufacturing Technique

For the Radiator Stack Architecture group, screen printing is being examined as an innovative method for creating flow field plates by building up the flow field design. This technique is quite different from machining, as it offers a build up, rather than

sculpting, approach. Screen printing is a low-cost manufacturing technique. Conservative estimates of less than \$5 per plate have been obtained [41] for fuel cell ready plates.

One of the biggest advantages of screen printing is the benefit of design flexibility. No longer is the channel width and path constrained by the machining bit. Also, different materials with controllable conductivity and porosity can be laid in different areas of the plate. With the new-found flexibility, novel ideas have come out of the preliminary design work.

5.2 Flow Field Preliminaries

Flow field design is an integral part of fuel cell design. The motivation for studying this area is improved cell performance, particularly at high current densities.

The dimensions of the flow field are set mainly by mass transfer concerns. Complicating factors such as inherently low oxygen concentration in the reactant air stream, and water production and movement inside each cell requires a good design to achieve acceptable performance.

5.2.1 Mass Transfer Issues

Flow fields are required to get the reactants to reaction catalyst sites and remove product water. The rate of diffusion to the catalyst layer from the flow channel is a function of both convection and diffusion mass transfer coefficients [50]. These coefficients are a function of stoichiometry, pressure, Reynolds number and current density. The consumption of a reactant species sets up a concentration gradient that drives the mass transfer process. When air is used as the oxidant, the cathode reaction represents the rate-limiting step due to reduced mass diffusion (concentration dilution). At the same time, the production of water of the cathode causes another diffusion impediment. Thus, effective water management is important.

5.2.2 Water Management

There are two water sources for PEM fuel cells. Due to the humidification of reactants, water vapour enters the cell with both hydrogen and air. Product water is also produced at the cathode catalyst layer. However, due to electro-osmotic drag and back diffusion, it can manifest itself at the anode, cathode, or a combination of both. Figure 5.1 schematically depicts the modes of water transport and uptake in a PEM fuel cell.

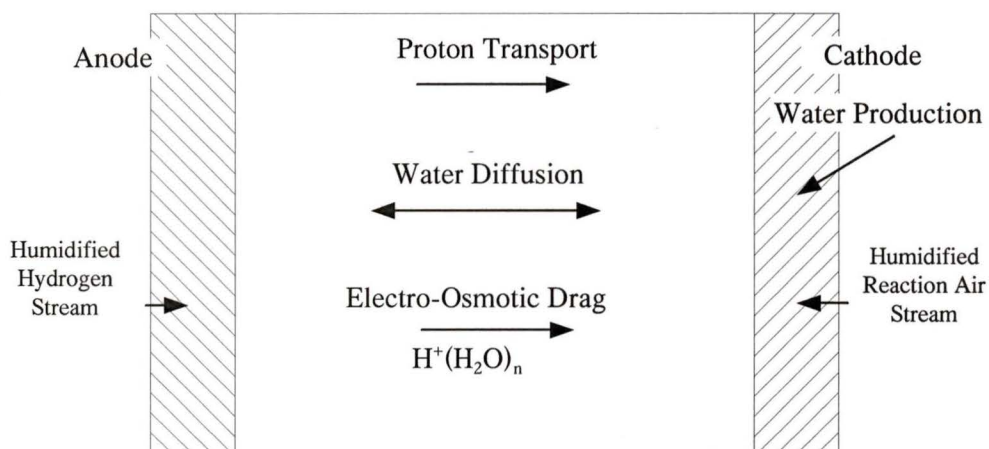


Figure 5.1: Modes of Water Transport in a PEM Fuel Cell

The net flux of water through the membrane electrode assembly is known to be a function of current density [57]. Accumulation of water at the cathode is problematic for several reasons. If the water is not removed, it reduces the accessibility of the catalyst to the reactants. Secondly, the accumulation of liquid water interferes with the permeation of reactants through the cathode to the catalyst layer. In addition, the accumulation of liquid water can impart changes in the membrane, causing localized expansion and swelling of the membrane [29]. The movement of gases in the channels and water vapor concentration gradients help remove water. Additional methods are discussed in Section 5.2.3.

5.2.3 Water Removal Mechanisms

5.2.3.1 Reduced Reactant Inlet Relative Humidity

An important concept in water management is relative humidity. Relative humidity (ϕ) is a measure of the water vapour content in a gas compared with the saturated water content at the same temperature and pressure. The saturation pressure for water vapour is only a function of temperature, and can be defined as shown in Section 3.4.

$$\ln(P_{sat}) = 70.434643 - \frac{7362.6981}{T} + 0.006952085T - 9.0000 \ln T \quad (3.9)$$

To help control the amount of liquid water present, the reacting hydrogen and air can be introduced into the flow channels at relative humidities less than 100 percent. This increases the amount of water vapor the reactant stream can absorb, and helps draw liquid water out of the cell. The increased ability to remove water must be balanced with the detriment of possible localized membrane drying.

5.2.3.2 Temperature Gradients

A temperature gradient along the length of a flow channel increases the saturation vapor pressure of the gas stream. This is difficult to induce due to the length of the flow paths and the close contact of the fuel cell components. Generally, in fuel cells it is desirable to maintain a uniform temperature over the MEA surface for uniform operation. Introducing the reactant streams at a lower temperatures decreases performance in some areas. Very high temperatures, such as greater than 95°C, are undesirable due to the substantial increase in saturation vapor pressure, which effectively dilutes the reactant species and further reduces power output.

5.2.3.3 Pressure Drop

A pressure drop develops as a gas flows along the flow field channels due to friction and changes in direction. This pressure drop in the gas increases its water carrying capacity as the total pressure is reduced. This occurs on both sides of the cell in oxidant and fuel flow fields. This fact can be used to remove liquid water from the fuel cell, preferably on

the anode side. The pressure drop is controlled by various parameters. These include channel geometry, length, roughness, operating stoichiometry, number of channels and number and types of bends.

5.3 Flow Field Model Formulation

A flow field model was developed to examine basic inputs and outputs of flow field design. The outputs examined include pressure drop, flow conditions (Reynolds number and flow velocity), gas uniformity between the channels and also, the overall flow path.

5.3.1 Inputs

There are many inputs to consider in terms of flow field design. The active area of the design, range of current densities expected, and stoichiometry, set the mass flow requirements. The operating temperature and pressure should also be chosen before the design process begins. For example, significant differences in design would be apparent between a PEM fuel cell operating at 400 kPa_a and 130 kPa_a. The operating temperature and pressure desired determines reactant gas properties.

Physical parameters are also very important. The channel cross-section, which includes channel width, depth and angle of side walls influences flow and pressure drop.

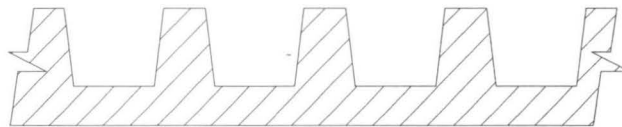


Figure 5.2: Flow Field Plate Cross-Section

The number of channels is also meaningful, as it determines the cross-sectional area for the flow. The individual channel flow is affected, as the active area, and thus, mass flow requirements remain unchanged. The rib width is important in terms of electrical conduction. The ribs must have sufficient contact with the MEA to ensure minimal contact losses from the cathode, through materials and any interfaces, to the anode. The

angle of side walls is usually a parameter determined by the method of manufacturing the flow field plate. In the case of machining and molding, the angle is determined by requirements for tool or die-release. For screen-printing, the number of layers required, as well as viscosity and composition of ink play an important role. Figure 5.2 shows a typical cross-section of a flow field plate.

The basic physical parameters have been shown. However, the flow fields must also be looked at from a higher level. The flow fields must fit on the plate footprint, with gases entering at inlet and exiting at outlet, having the ability to cover the assigned active area.

5.3.2 Pressure Drop

Pressure drop is considered one of the critical parameters in flow field design due to its importance to water management. The pressure drop along the channels is imparted due to the frictional losses along the channel. The pressure drop can be considered as the summation of the pressure drop due to physical channel length and the contribution due to each bend. In the case of bends, bend loss coefficients are dependent on bend type. The total pressure drop in a bend is the sum of the following components: frictional head loss due to the length of the bend, head loss due to curvature, and head loss due to excess pressure drop downstream due to profile distortion [21]. The pressure drops, other than frictional loss, are combined and expressed as a loss coefficient.

Limited results are available for fluid flow through bends having a rectangular cross section. As such, correlations for circular ducts are used. Correlations for channel flow are extended for use with non-circular geometries by introducing the hydraulic diameter, defined by

$$D_{hyd} \equiv \frac{4A}{P} \quad (5.1)$$

where A is the cross sectional area, and P is the length of wall in contact with the flowing fluid at any cross section. The hydraulic diameter concept is valid for aspect ratios ranging from $\frac{1}{4}$ to 4.

Gas flow in channels of typical size (1-9 mm²) have gas flows which are laminar. This can be shown using Equations 3.6 and 3.7 to determine mass flows, and using

$$Q = \frac{\dot{m}}{\rho} \quad (5.2)$$

$$\bar{u} = \frac{Q}{\frac{\pi}{4} D_h^2 N_c} \quad (5.3)$$

and Equation 5.4 to determine the Reynolds number.

$$Re = \frac{\bar{u} D_{hyd}}{\mu} \quad (5.4)$$

The following definitions are used. Q is the volumetric flow, \bar{u} is the average flow velocity, and μ is the absolute viscosity.

The basic equation used to determine pressure loss is

$$\Delta P = fQ \left(\frac{L_e}{D_h} + N_{bends} \psi^* \right) \frac{\bar{u}^2}{2} \quad (5.5)$$

This ignores potential and kinetic terms which are negligible compared to the losses due to friction and bends. For fully developed laminar flow in horizontal pipes (constant pressure gradient), f , the Darcy friction factor, can be determined analytically [16] to be

$$f = \frac{64}{Re} \quad (5.6)$$

An exact expression was obtained for the same flow in rectangular ducts [21]. This is shown in Equation 5.7.

$$f Re = \frac{96}{\left(1 + \frac{1}{a^*}\right)^2 \left(1 - \frac{192}{\pi^5 a^*} \sum_{n=1,3,\dots}^{\infty} \frac{\tanh(n\pi a^* / 2)}{n^5}\right)} \quad (5.7)$$

where a^* is the duct aspect ratio. For the aspect ratios considered, Equation 5.7 predicted friction factors 8 percent higher than Equation 5.6. Due to computational ease, and the magnitude of the difference, Equation 5.6 was favored for use.

Again from Equation 5.5, the actual lengths, hydraulic diameter and number of bends were calculated from the model data. ψ^* is a dimensionless length/diameter which models the pressure drop due to a 90° bend. A value of 30 was used for this parameter [16].

The effects of the “slip” velocity of the gas in the carbon paper layer has not been taken into account. Thus, it is assumed that this has a minimal effect on the results. This is examined in Section 5.5.

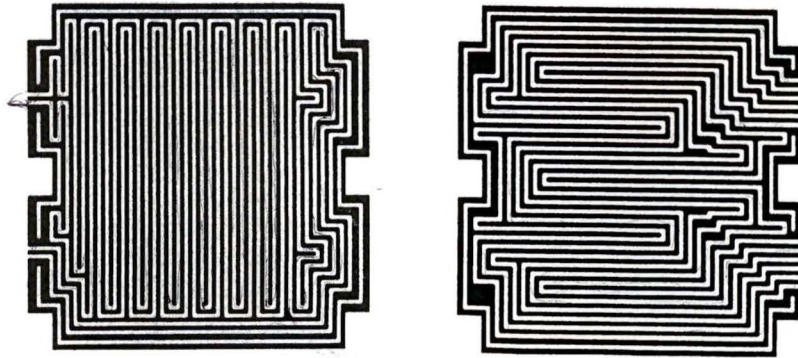
5.4 Flow Field Plate Designs

For the TERS97 design, plates were required for a working prototype. The architecture and footprint for the design were set by the RSA group. This located the inlet and outlet. The plate was to have an active area of approximately 250 cm^2 and a maximum output power at 0.84 A/cm^2 . This ensures the generation of adequate current to drive an automobile.

The reactant delivery plates were created using a screen printing manufacturing technique. Because the final ink composition was undetermined, relatively large flow channel and rib widths were desired. Also, it was desired not to test the registration for the printing on the first run of printed plates. As expertise in the printing is built-up, smaller channels will be sought.

Data about flow characteristics in flow field plates was acquired from patents [67,68,70,74,75,77], literature [69] and studied existing designs. For a first run, no radical departures from known working parameters were desired, especially with the new manufacturing technique. Thus, flow characteristics were engineered to near similar

values for average flow velocities, Reynolds numbers, and pressure drops as with Ballard's MK-5 design. The initial hydrogen and air flow field plates for the TERS97 stack (Design 5) are shown in Figure 5.3.



(a) Hydrogen Flow Field Plate

(b) Air Flow Field Plate

Figure 5.3: Flow Field Designs for TERS97 Stack

The inlet and outlet were placed on the same side of each plate, so a common manifold with 2 reservoirs could be used to contain like gases. Table 5.1 shows the operating parameters.

Table 5.1: Fuel Cell Operating Parameters

| | Ballard MK-5 | TERS97 |
|---|-----------------|--------|
| Active Area (cm ²) | 218.5 | 248.1 |
| Design Current Density (A/cm ²) | 0.6 | 0.6 |
| Fuel Stoichiometry | 1.5 | 1.5 |
| Air Stoichiometry | 2.0 | 2.0 |
| Operating Pressure (kPa _a) | 304 | 304 |

The flow and pressure drop parameters for the design at the specified operating point are shown in Table 5.2. Existing Ballard MK-5 plates were reverse-engineered as a basis for comparison.

Table 5.2: Design Parameters for Ballard MK-5 and TERS97

| | Ballard MK-5 | TERS97 |
|--|-----------------|------------|
| # of Fuel Channels | 2 | 2 |
| # of Oxidant Channels | 10 | 6 |
| <i>Fuel Flow Field Plate</i> | | |
| Channel Width / Depth (mm) | 1.0 / 1.0 | 2.07 / 0.9 |
| Rib Width (mm) | 1.0 | 2.07 |
| <i>Oxidant Flow Field Plate</i> | | |
| Channel Width / Depth (mm) | 1.0 / 1.0 | 2.31 / 0.9 |
| Rib Width (mm) | 1.0 | 2.31 |
| Mean Velocity (m/s) / Reynolds Number | | |
| Fuel (H ₂) | 6.2 / 130 | 4.4 / 120 |
| Oxidant (Air) | 4.0 / 580 | 4.5 / 840 |
| Total Pressure Drop (Pa) | | |
| Fuel (H ₂) | 20,000 | 6,300 |
| Oxidant (Air) | 6,700 | 4,900 |

As shown in Table 5.2, due to the larger channel diameter, particularly in the case of the fuel flow field plate, a lower pressure drop results. This limits the facilitation of anode water removal. The solution to this problem is to use a single fuel supply channel. However, this greatly increases the flow velocity and Reynolds number. For the TERS97 designs, the channel and rib thickness were picked to allow the flow path to “fit” the design footprint for the design, and still have suitable dimensions for screen printing.

5.5 Pressure Drop Validation

5.5.1 Test Apparatus

Due to the importance of pressure drop to water management, the pressure drop in the two flow fields, as shown in Figure 5.3, was studied. The purpose was to validate the pressure drops calculated by the model. For the testing, an operating single cell was not used. Both, hydrogen and air delivery flow field designs were printed onto a solid

impermeable backing. A picture of a hydrogen flow plate, with a copper backing and half of the $\frac{3}{4}$ " aluminum test support apparatus is shown in Figure 5.4.

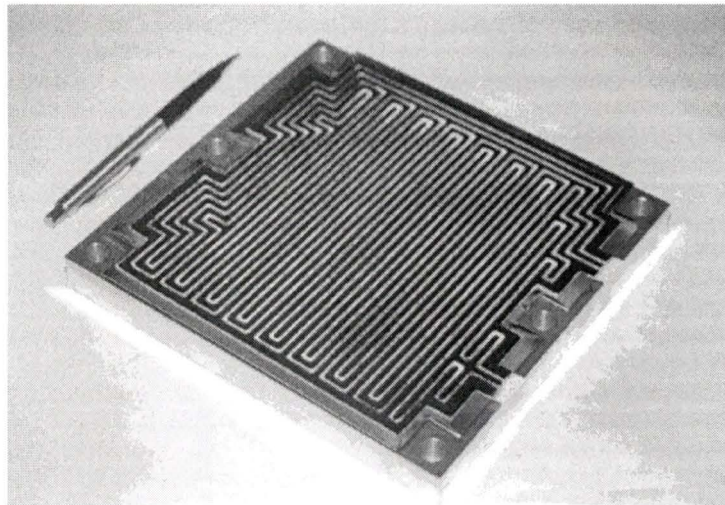


Figure 5.4: Hydrogen Flow Field Plate

The hydrogen flow field was printed on a hard plastic backing. The air flow field was printed on grafoil. The final assembly consisted on the following successive layers: aluminum support plate - copper backing - flow field plate - carbon paper - copper sheet - aluminum support plate. The basic cell assembly was edge-sealed using epoxy.

A schematic of the experimental apparatus is shown in Figure 5.5. Unhumidified air was used as a working medium in both the hydrogen and air delivery plates due to availability.

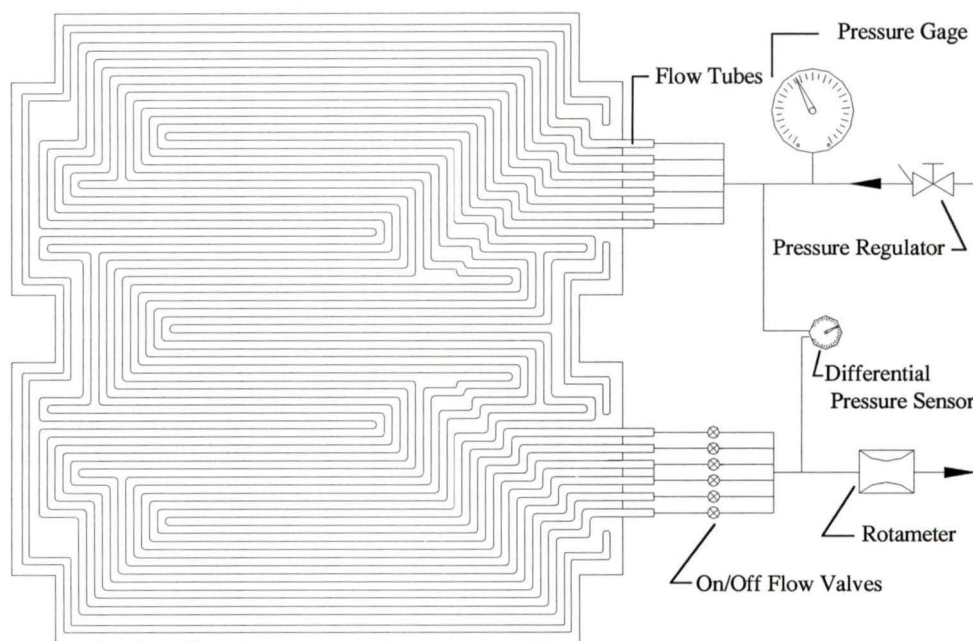


Figure 5.5: Schematic of Pressure Drop Testing Arrangement

Pressure drop was measured for various inlet pressures and flow rates. The inlet pressure was controlled by a pressure regulator. Tests were conducted at 21°C, with pressures ranging from 70 kPa_g (10 psig) to 207 kPa_g (30 psig) in increments of 34.5 kPa (5 psi). The volumetric air flow rate was adjusted from 0 to 8.7 SLPM using an Omega 150 mm rotameter (FL-3439G). Two different arrangements were tested. The first arrangement was with all the flow channels open. This simulates a “normal” fuel cell as equal pressure drops in all channels result. The second arrangement was single channel testing. For the hydrogen plate two channels were tested. All six were tested for the air flow field plate. In all cases the rotameter vented to atmosphere. Pressure drop measurements were also taken to correct for header losses. This was done for test conditions.

A Motorola MPX50DP sensor was used to sense the differential pressure between inlet to outlet. The sensor gave an output voltage proportional to pressure differential. Calibration of the sensor was accomplished using a more precise pressure differential measuring device. The calibration curve for the MPX50DP is shown in Figure 5.6.

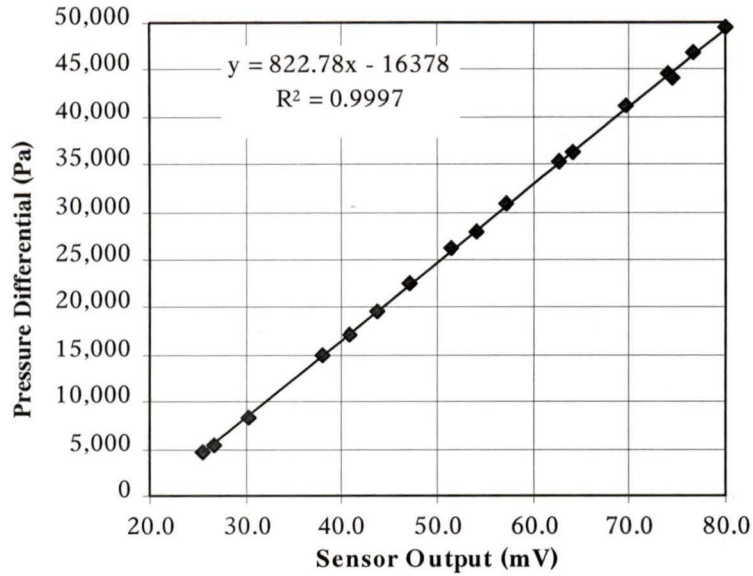


Figure 5.6: Calibration Curve for Motorola MPX50DP

The output voltage was found to be very linear with changes in pressure. For the calibration process, a needle valve was used to change pressure differential.

5.6 Pressure Drop Results

The specific details for the designs tested as manufactured, **both using air**, are shown in Table 5.3.

Table 5.3: Flow Field Data for Pressure Drop Testing

| | H ₂ Plate | Air Plate |
|--|----------------------|-----------|
| Rib Height (mm) | 0.72 | 0.72 |
| Channel Width (mm) | 2.1 | 2.2 |
| Channel Lengths (mm) / (Number of Bends) | | |
| 1 | 2998 (67) | 958 (26) |
| 2 | 2940 (65) | 890 (22) |
| 3 | | 872 (22) |
| 4 | | 911 (24) |
| 5 | | 893 (26) |
| 6 | | 923 (30) |

5.6.1 Hydrogen Flow Field Plate

Experimental results for tests at 167 kPa_a and 308 kPa_a are shown in Figures 5.7 and 5.8 respectively. These are the two extremes of the data collected.

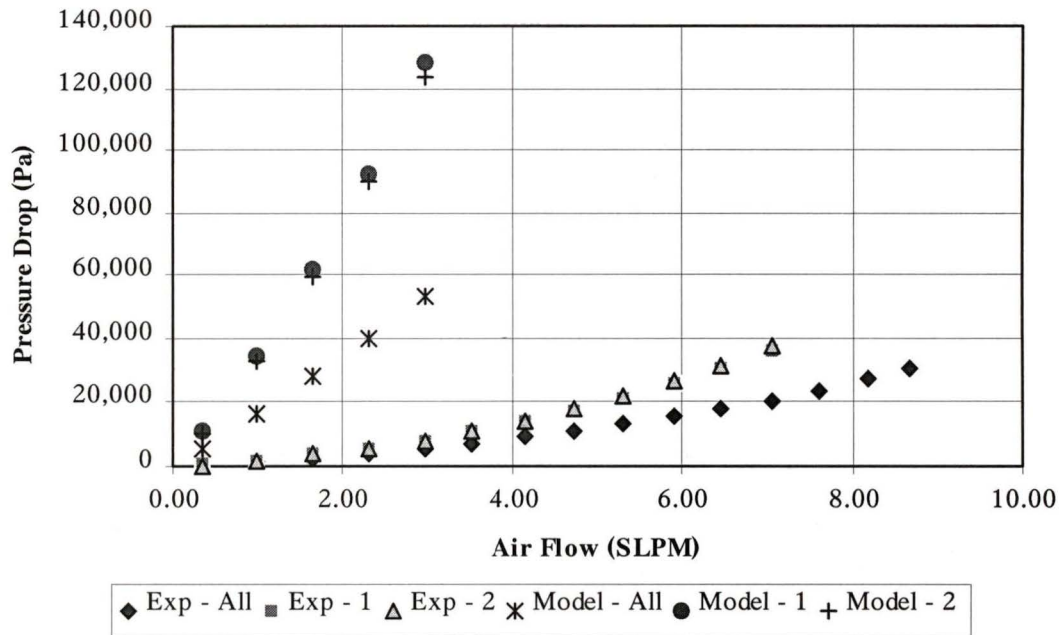
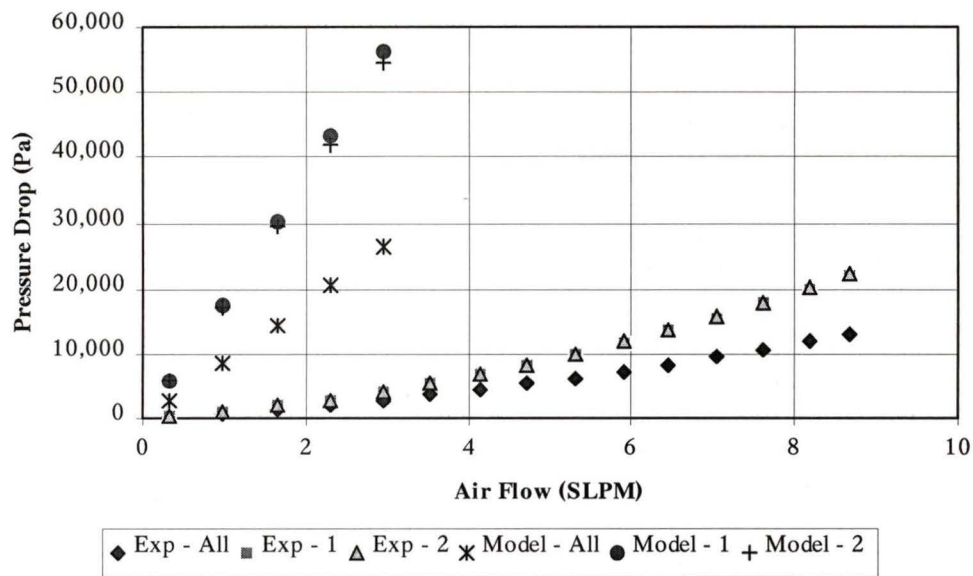


Figure 5.7: Hydrogen Flow Field Plate at 167 kPa_a

Figure 5.8: Hydrogen Flow Field Plate at 308 kPa_a

“Exp” refers to experimental results, and the numbers correspond to the individual channels. Tests done at higher total pressures led to lower pressure drops due to smaller volumetric flows and lower average flow velocities. This change was seen in the experimental data, and is proportional to the change in absolute pressures.

When switching from the all channel case, to the single channel test, Equations 5.1-5.6 can be used to show that the expected pressure drop should be at least double the all channel test using 2 channels. For the experimental results, the pressure increased by only 150 percent. This issue was then further examined with the air plate.

The model results are shown for reference. The model results account for the decrease in pressure along the channel, and thus, the results are not quite linear with increasing mass flow. As an approximation, the pressure drop is calculated initially assuming a constant absolute pressure (pressure at inlet) in the channel. Next, the pressure drop is calculated a second time using the new *average* pressure value calculated using

$$P_{new} = P_{test} - \frac{\Delta P}{2} \quad (5.8)$$

5.6.2 Air Flow Field Plate

Experimental results for air tests at 167 kPa_a and 308 kPa_a are shown in Figures 5.9 and 5.10, respectively.

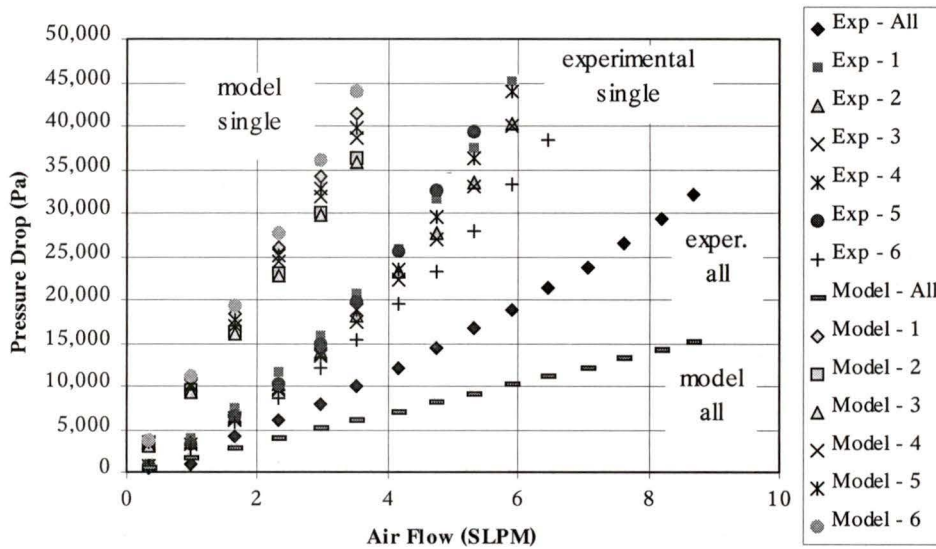


Figure 5.9: Air Flow Field Plate at 167 kPa_a

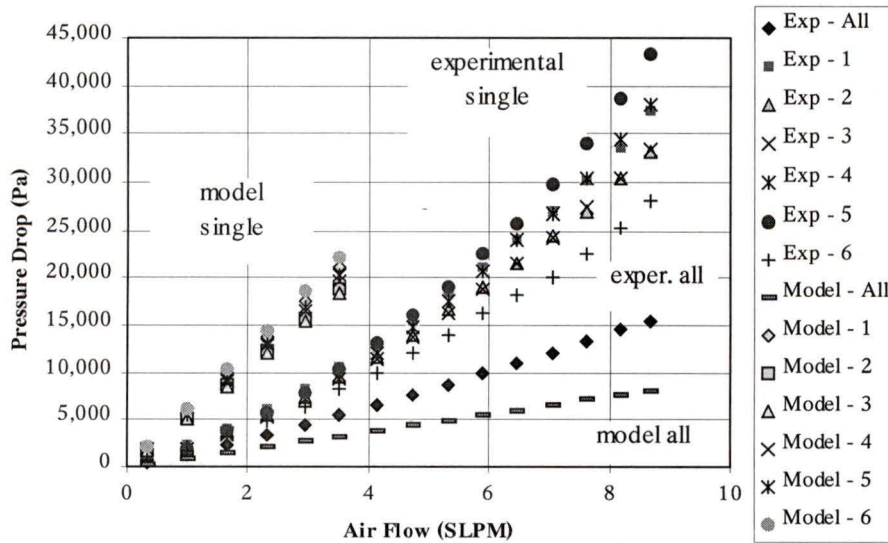


Figure 5.10: Air Flow Field Plate at 308 kPa_a

For the air flow field tests with the *all channels open* arrangement, the experimental pressure drop was 1.5 to 2.0 times larger than the predicted values. However, the results for the single channel tests were 2.5 to 2.8 times lower.

5.6.3 Summary

The results from the flow field pressure drops raised some concerns with the initial flow field designs. The single channel tests for the air flow field plates were much lower than expected, especially compared to the experimental *all channel* tests. This raised the curiosity that gas cross-over between the channels was occurring.

With the original test set-up, on/off valves on only outlets were used to control the air flow. For the single channel tests, all inlets remained open, and all valves except one (the channel to be tested) were closed. Assuming no cross-over, this leaves all closed channels stagnant at a pressure equal to the inlet pressure. It was realized that a sizable pressure differential (up to 100 kPa) would be created between neighboring flowing and non-flowing channels during testing due to the arrangement. However, It was hoped that the amount of communication between channels would not significantly affect results.

To investigate amount of cross-over, the hydrogen flow plate was retested. This time valves were added to *both outlets and inlets*. If cross-over was occurring, the hydrogen flow plate would have the most due to the very long serpentine channels. Tests concluded that gas cross-over was significant, and even possibly the dominant mass transport path for the design flow fields. Tests were conducted at high and low pressures and flow rates, but trends were the same. Sample results are shown in Table 5.4 for testing at 3.52 SLPM and 308 kPa_a.

A contributor to the significant gas diffusion is the carbon paper. This was included to simulate “real” fuel cell flow conditions. To help increase pressure drop, future flow

fields should always have inlets and outlets as far apart as possible. The results would have been even more magnified using hydrogen gas, as its viscosity is 2.2 times lower than air, and has an affinity for leaking.

Table 5.4: Pressure Drop Results Confirming Gas Cross-over

| Inlet(s) Open | Outlet(s) Open | ΔP (Pa) |
|---------------|----------------|-----------------|
| ALL | ALL | 7,500 |
| 1 | ALL | 11,000 |
| 2 | ALL | 10,900 |
| 1 | 1 | 14,900 |
| 1 | 2 | 12,800 |
| 2 | 1 | 14,900 |
| 2 | 2 | 12,700 |

It would be expected that the 1-1 and 2-2 combinations would have dramatically smaller pressure drops than the 1-2 and 2-1 combinations, as the gas must cross at least 1 rib to exit by a neighboring channel. The data, when viewed in combination with the locations of the inlet and outlet of the channels, seems to correlate better with absolute (straight-line) distance between inlets and outlets, than with flow path distance. Channel 1 inlet and outlet were farthest apart, with the Channel 2 inlet and outlet closest together.

The effect of increased clamping pressure on the flow fields was also investigated. The results are shown in Figure 5.11. The clamping force was not recorded, but increased linearly.

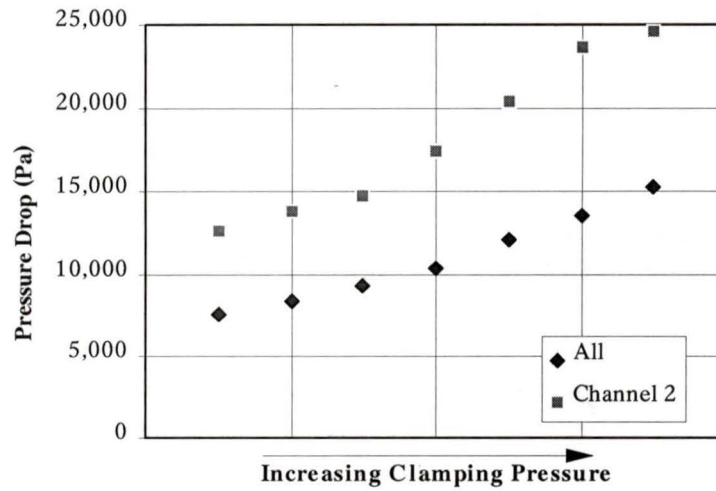


Figure 5.11: Effect of Clamping Pressure on Pressure Drop for Hydrogen Flow Field at 308 kPa_a and 3.52 SLPM

Increased clamping pressure was found to increase pressure drop. However, this is likely not due to decreased diffusion, but rather rib deformation, as the tendencies shown in Table 5.4 were always present.

As a result of these findings, new flow fields were developed. These are shown in Figure 5.12. Details on these designs have been excluded.

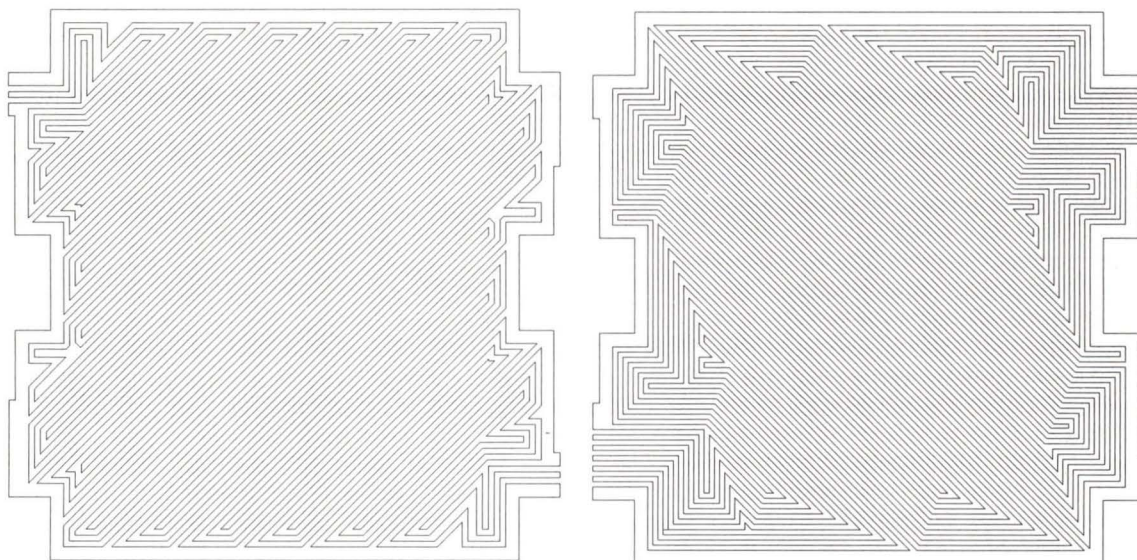


Figure 5.12: Second Generation Flow Field Designs

5.7 Development of Flow Field Alternatives

Screen printing of reactant delivery plates offers the benefit of design flexibility. No longer is the channel width and path constricted by the machining tool. Three new ideas have come out of the preliminary work in flow field design with screen printing.

The first new concept is waved flow channels. A section of a sample flow field is shown in Figure 5.13. The actual implementation of this design will likely have channels that are the same size. The figure shown was also used to test the ability to screen print small channels.

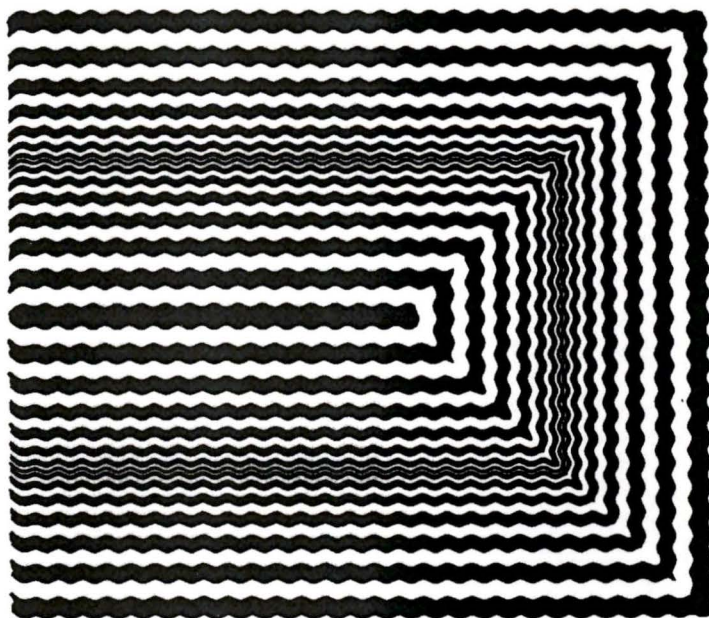
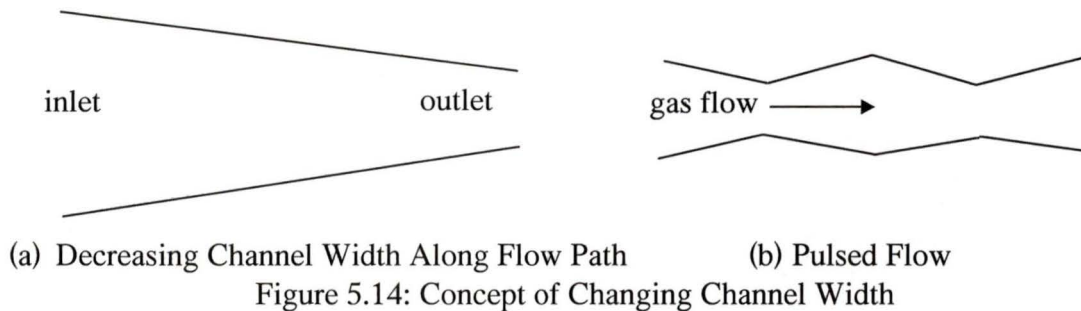


Figure 5.13: Waved Flow Field Concept

The waved channel concept will increase pressure drop for a given channel length, and promote gas mixing in the channels which both should improve fuel cell performance, particularly at higher current density. The amplitude and wavelength of the wave are the controlled parameters. Currently, many flow field designs have long straight paths. This localizes much of the pressure drop in the flow fields to the sharp corners. A waved channel will allow for even distribution and control of pressure drop.

The second new concept is a changing channel width along the length of the flow path. This is easily incorporated with screen printing. Due to the fuel cell reaction, the amount of hydrogen, air and water (both liquid and vapour) in the flow channels change as reaction gases proceed along the flow path. This changes the density, viscosity, and species concentrations of the channel's contents. Due to the changing composition, it may be desirable, for water management reasons, to decrease the channel width (Figure 5.14 (a)). A twist on this, is the combination of increasing and decreasing channel widths to create pulsed flow (Figure 5.14 (b))



Another new concept [45] involves the use of sharp corners in flow channels to provide flow separation and increase mixing. Also, with the addition of obstacles in the flow path, higher, and more importantly, controlled pressure drops result. Figure 5.15 shows a representation of this concept.

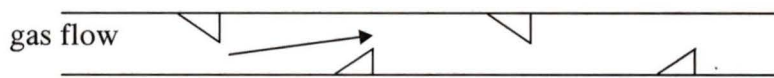


Figure 5.15: Imparting Flow Obstacles

These new concepts are made possible by the elimination of the tool bit, and the design flexibility of screen printing. It is hoped that testing of these new, patentable concepts, can validate improved performance.

Chapter 6

Rapid Prototyping of Hydrogen and Air Delivery Plates

6.1 Motivation for Rapid Prototyping

The traditional method for producing fuel cell flow field plates involves a laborious design process. After the design parameters are selected, dimensions and drawings of the plates are passed to a manufacturing team. The flow field design is then carefully machined into prepared graphite blanks with a CNC machine. Due to the fine dimensions of flow channels and the poor machinability of the graphite, the process is costly. The generation of CNC codes is also less cost-effective for small runs of plates.

The precise modeling of fluid interactions in fuel cells is difficult due to two-phase flow, number of processes taking place, stack temperature gradients, and physical size. As such, testing with various parameters is usually done with each flow field design in single cell and stack configurations. Due to long lead times in the design, manufacturing and testing stages, progress is limited.

With rapid prototyping to automate design, and some of the manufacturing stage, production times can be greatly reduced.

The process (*rapid production of stencils*) proposed is presented using screen printing as the targeted production/manufacturing method for flow field plates. For screen printing, the required output from the design stage is a high quality stencil of the design on a transparent material, such as acetate. Opaque areas on the stencil represent areas that require build-up. Using a rapid production procedure for the generation of stencils, and a quick low-cost manufacturing method to create the plates, the lead times for getting flow field plates to testing is greatly reduced.

6.2 Computer-Aided Flow Field Design

The critical design parameters in flow field design have been identified as pressure drop, flow velocity and Reynolds number. Computer code, using many of the equations of Chapter 5, can be used to successfully design flow fields.

The automation of the design process can be broken into two distinct steps. First, the determination of the geometry and values for parameters, and second, the generation of the model. A computer program can be used to direct efforts, with the level of complexity, such as in the geometry of the plate or other variety allowed, controlled by the ability of the programmer.

6.2.1 Design Process

Fuel cells are designed distinctly for different applications, as each has specific requirements, such as needed power output. Electric motors and power conditioning systems typically have desired ranges for input voltage and current expected from the fuel cell engine. With this knowledge the stack configuration and active area can be set. This “high-level” design process, combined with general design architecture, sets the layout of the flow field plate.

After this process has taken place, the flow field plates can be parameterized for analysis. For instance, a rectangular plate would require that the length, width and depth be

specified as base dimensions. Other important informations include the geometry of the flow field design, and sealing requirements, such as a gasket width and location.

This process was implemented for Ballard's MK-5 bipolar plate design. The inputs for physical dimensions included the plate length and width, "side inset on edges" (sw), side length, gas header length are shown in Figure 6.1.

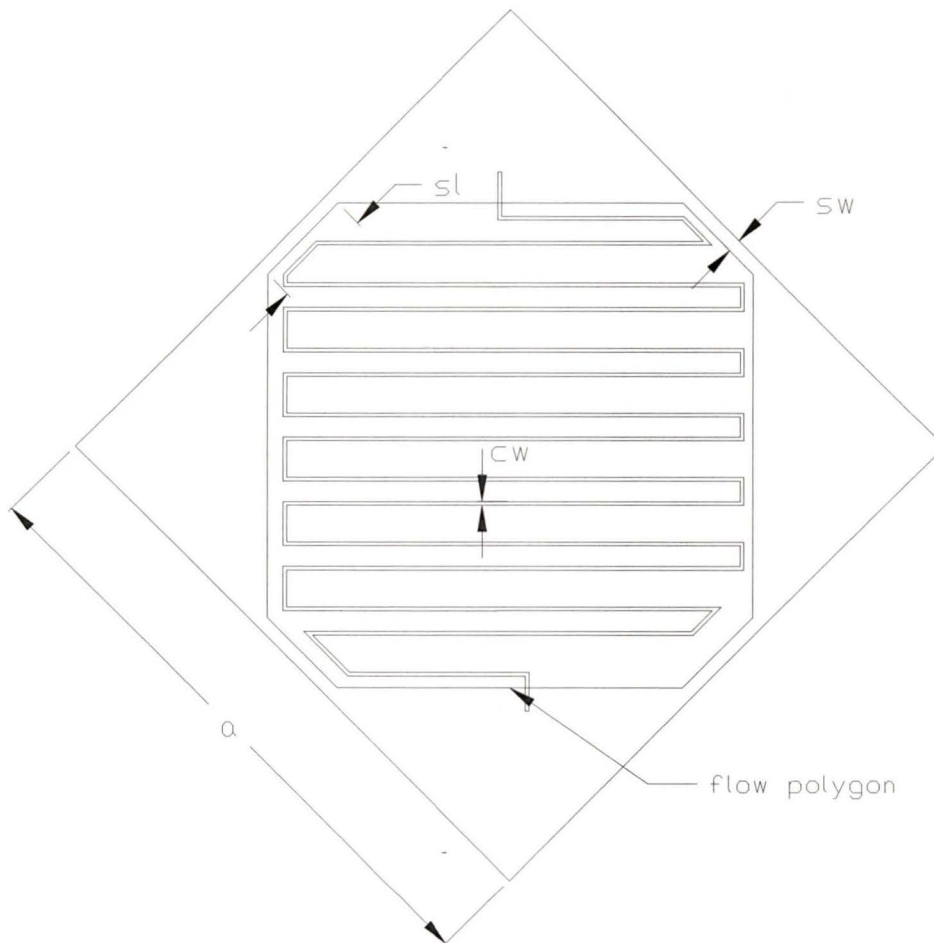


Figure 6.1: Sample Flow Field Plate Parameterization

With this implementation, the next step is to specify the operating conditions and design criteria. The operating conditions include temperature, pressure and reactant stoichiometries. In general, design criteria may include certain pressure drops, or a

number of channels, or possibly a channel width and depth for each of the reactant delivery plates.

For the case implemented, it is assumed that the channel cross-section is invariant. This included the channel width, depth and wall angle. The channels were expected to follow a serpentine path and have a series of straight channel sections. At this point the calculations began. The flow field design must fit the bounding polygon allowed for by the stack. If not, the flow channels may pass into an areas required for sealing, or leave the plate entirely. An important parameter in ensuring a good fit is *spanwidth*. This is defined as the width of the channels serpentineing through the flow field. The width is calculated using

$$\text{spanwidth} = N_c (C_w + R_w) \quad (6.1)$$

where the number of channels (N_c), channel width (C_w) and rib width (R_w) are the important variables. The number of times (spans) the serpentine crosses the flow plate must be an integer value to ensure a through path for all channels. The location of the inlets and outlets determined if the number of spans is even or odd. The first and last spans are slightly different from the normal spanwidth. This width can be determined using

$$\text{first \& last spanwidth} = N_c C_w + \left(N_c - \frac{1}{2}\right) R_w \quad (6.2)$$

Much of the calculations from here on are dependent on the geometry of the flow field, and are therefore not introduced. The general flow of steps can be broken into the methodology shown in Figure 6.2.

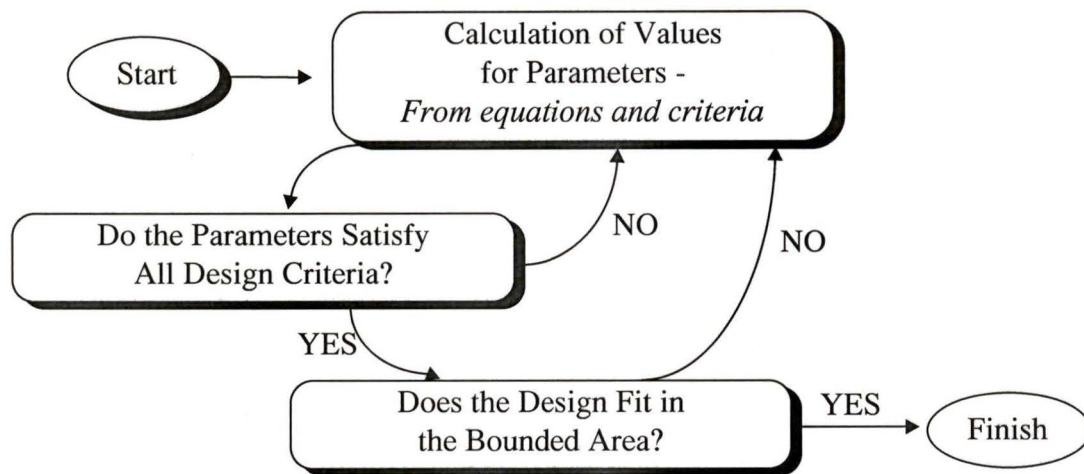


Figure 6.2: Flow Field Design Methodology

The physical parameters such as number of channels, channel width, channel depth, length of channel are to be determined. In addition, transport data such as mass flow rates, flow velocity, Reynolds number, and pressure drop are next to be calculated. After several iterations, a suitable design is found.

6.2.2 Model Creation

The next step is to create a representation of the design in a virtual environment. Many CAD packages allow for programming interfaces. Thus, the program is able to finalize the design, and direct the creation of the model. The requirements for the model are case dependent. For the implementation for the MK-5 design, C code was used to help design and then, automatically create a 2-D model in AutoCAD Release 12. Control points and offsets were used in the generation of the model.

For analysis, it may be desirable to create a 3-D solid model, to allow for additional computer-aided engineering. For instance, structural analysis with different compressive loadings could be accomplished using PRO/Engineer to simulate stack loadings.

6.3 Interface to Automated Stencil Making

Output from the design process varies depending on the manufacturing method used. As flow fields generally involve intricate patterns, CNC machining is usually used. In this case, the output from the design stage is cutting path coordinates (tool path). For screen printing, a high quality, high contrast representation of the design is required. It is printed on a clear film, such as an acetate. A photographic technique is then used to pass the pattern from the acetate to a light sensitive polymer film. In a dark room, the first step is to mount the stencil on a screen. The screen backing gives the stencil support and integrity. The next step is to place the acetate over the stencil, and subject the “sandwich” to high power light. After which, the stencil is washed, and the appropriate areas of it are removed. The acetate required must be to-scale because it is directly transferred to the stencil, and have high contrast to protect light sensitive stencil areas that must remain.

6.4 Summary of Rapid Prototyping for Flow Field Design

With the process presented, numerous well-designed flow field designs can be created quickly. When combined with a rapid and flexible manufacturing method, such as screen printing, numerous designs can go from concept to laboratory testing in 2 to 3 days. With test results able to improve modeling through feedback, new and improved designs will be generated in future iterations.

A summary of the process is shown in Figure 6.3

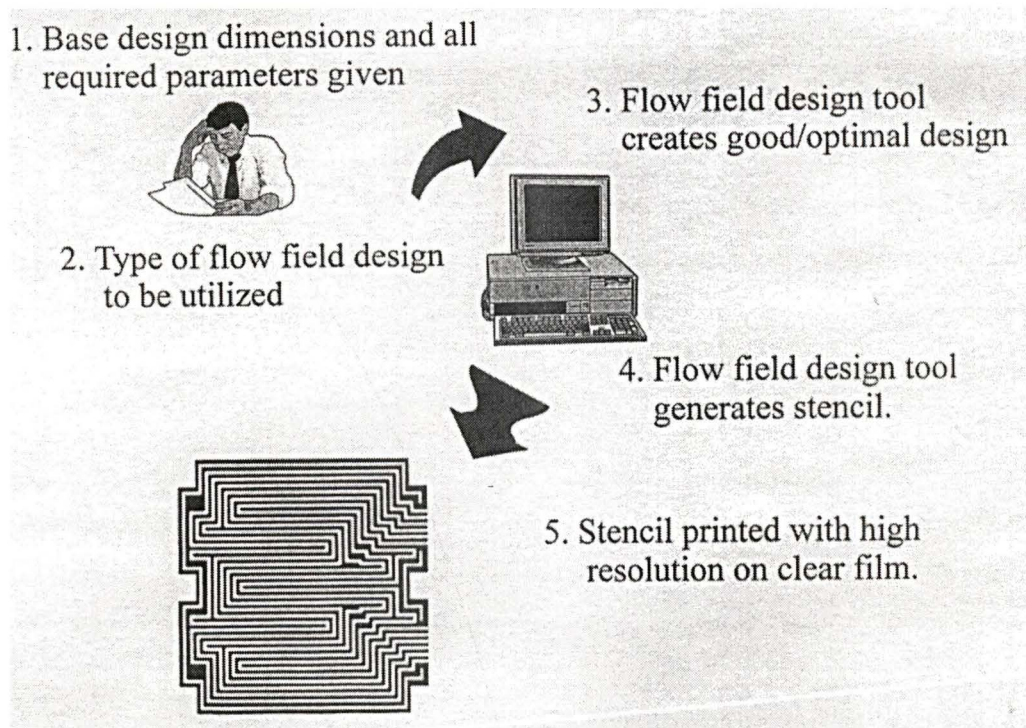


Figure 6.3: Rapid Production of Stencils for Screen Printing

With current techniques, this process takes on the order of weeks to complete.

6.5 Prototype Software Design Tool

Section 6.2 discusses some of the details of the C program that creates various computer models based on Ballard's MK-5 bipolar plate design. The program does not perform all requirements for a rapid prototyping tool as described. This program focuses on the feasibility of rapidly creating various computer models based on user information. It also does engineering calculations related to *mass flows, flow conditions and pressure drop*. Reference 40 contains a very detailed description of program operation that cannot be included here due to its length.

6.5.1 Input Variables

The input variables for the program include the physical variables shown following. The program variable name and typical dimension size are also given.

- *plate length/width* (a) <23.0 cm>: the plates are typically square, thus the length and width are identical.
- *side inset on edges* (sw) <0.5 cm>: this is the nearest distance the gas flow channels get to the edge of the plate.
- *gas area side length* (sl) <3.7 cm>: the basic flow area forms an octagon. This variable is the length of the shortest side of the octagon.
- *number of channels* (nc) <4>: the number of flow channels.
- *channel width* (cw) <0.10 cm>: the width of the flow channel.
- *gas header length* (hl) <1.0 cm>: the length of the header from the “flow octagon” to the manifold. The manifolds were not drawn.
- *channel depth* <0.9 cm>: the depth of the flow channel.
- *current density* <0.500 A/cm²>: this is the operating condition of the fuel cell. The current density is the average current output for the area which makes up the “flow octagon”. This condition directly specifies the reaction air requirements. An air stoichiometry of 2.0 is used for all calculations.

6.5.2 Comments on Program Use

The user is prompted for the following pieces of information (all dimensions in cm)

“Enter the length and width of the plate <23.0>:”

“Enter the side inset on edges <0.5>:”

“Enter the gas area side length <3.7>:”

“Enter the number of channels <4>:”

“Enter the channel width <0.10>:”

“Enter the gas header length <1.0>”

The plate is then created. This may take 30-120 seconds depending on the hardware.

The user is then prompted for two additional pieces of information to complete the engineering calculations.

“Enter the channel depth <0.9>mm:”

“Enter operating current density <0.500>A/cm²:”

After which the engineering calculations are completed and the results are directed to the AutoCAD text window.

6.5.3 Program Summary

The geometry requirements of the serpentine flow pattern were found challenging. During the course of this work it was realized that the code must be similar to machine code required to cut the flow channels. Only in this case, the program had to cover all dimensional possibilities. There is still some work to be accomplished to cover all possible cases, but on a whole the program is working to a high level. The code does not place limits (a range) on the user specified values. This gives the user maximum freedom, however, nonsense results will be created if the channel width is, for example 1000 metres.

The initial manual drawing of a sample plate design took approximately 5 hours. The program does the same task including calculations, which could not be done by standard AutoCAD commands, in less than 2 minutes.

Chapter 7

Concluding Remarks

Air-cooled proton exchange membrane (PEM) fuel cells have been shown to be a feasible alternative to the more prevalent water-cooled designs. Combining the previously separate fuel cell and radiator devices leads to a larger stack design, but offers the system benefits of increased simplicity, and potentially improved reliability and lower cost. Air-cooled systems eliminate an intermediate cooling medium, have fewer components, and with effective integration as shown, can use materials well-suited for heat rejection. Performance goals for the six new Radiator Stack Architectures (RSA), developed by *Next-Generation Fuel Cells for Transportation* (NGFT), were based on the best existing (1995) PEM fuel cell technology, New Electric Car II (*NECARII*). Modeling of *NECARII* was done to obtain necessary stack and system performance data.

System power density is one of the most important parameters in introducing an automotive fuel cell power plant. The TERS97 design was found to have volumetric and gravimetric power densities 37 and 19 percent lower, respectively, than *NECARII*. The modeling of ancillary equipment concluded that the air compressor consumed up to 21 percent of the total gross power in all tandem air cases. The small power consumers such as the cooling fan and water pump in all non-tandem air-cooled designs, were found to consume less than 400 W each from the total 64 kW gross stack output. A specific

interest with the *NECARI* system was membrane power density. It was determined to be 467 mW/cm^2 . This is 10.6 percent greater than was found for the TERS97 design.

Both ambient and tandem air systems were examined. It was revealed that tandem air systems, with independent reaction and cooling air, are better suited to the high power density automobile application with existing membrane technology. This is due to better reliability and performance. With the ambient air designs, more water vapour is required to fully saturate the reactant streams due to low pressure. This, combined with very high stoichiometries required for cooling, and large temperature gradients in the reactant air as it passes through the stack, makes proper humidification and the maintenance of membrane water content difficult.

The TERS97 design was a focus due to its potential for low cost, high power density and good manufacturability. This stack is a compilation of fuel cells and radiator-like cooling panels arranged in series. Two fuel cells are interspersed between each cooling panel that provides a current path, ensure adequate stack cooling, and maintains stack integrity by compensating for thermal expansion. The thermal compensation allows the use of external manifolding. Modeling and experiments concluded that the low-grade heat produced could be rejected with acceptable parasitic losses, using a variable speed fan. Heat rejection tests were found to match closely with model results, with a maximum outlet temperature deviation of 5.6°C . Experimental heat transfer and pressure drop results were then used to improve the model. Temperature gradients in the stack along the direction of air flow were an area of concern due to their effect on water management. The magnitude of the temperature differential across the panel was found to be a linear function of heat rejection. For the design point of approximately 175 W of heat rejection, a temperature difference of 5°C was experimentally found.

Examination of energy flows for the various designs was accomplished. The thermal characterization included the theoretical energy released by the reaction, evaporative

cooling effects of the product water, natural convection, radiation, and most importantly, forced convection due to the cooling air. Results show that air-cooling must satisfy the majority of the cooling requirements. Cooling due to radiation and natural convection was included for completeness. These passive cooling mechanism made up 3 to 10 percent of the total heat rejected for current densities greater than 0.3 A/cm^2 .

Rapid Prototyping

The gas delivery plate for the PEM fuel cell stack is the second most important cost contributor next to the MEA. Thus, cost and manufacturing complexity reduction is critical to the future development of the technology. A method of rapid prototyping gas delivery plates was explored using CAD/CAM and screen printing or CNC machining as target manufacturing methods. The feasibility of the rapid prototyping method was proven through a two part process, one which examined general flow field design, and another which generated various computer models suitable for direct manufacturing use.

The gas delivery plate was shown to be a very integral part of fuel cell design. The important areas of mass transfer and water management were modeled. Pressure drop along the reaction flow channels was identified as an important design parameter, and a pressure drop model was constructed based on pipe flow. Through testing of the screen printed TERS97 flow field designs, the importance of the inlet and outlet locations was realized. Air flow, in locations other than the channels, was found to be significant. This did not allow for model validation. Significant gas cross-over between channels resulted in poor cell coverage. Thus, the design was changed to have the inlets and outlets as far apart as possible.

The second part of the process, the generation of the model, was implemented for a geometry based on Ballard Power Systems' MK-5 plate. The implementation was written in C code and interfaced with AutoCAD to generate the model based on characteristic gas delivery plate dimensions.

7.1 Recommendations for Future Work

Design, modeling and experimental efforts have brought the TERS97 air-cooled design to the prototyping stage. Current efforts should focus on testing 8 to 10 cell prototypes. After hours of continuous testing, valuable informations will result, and truly validate expected performance.

The current gas delivery plates are manufactured by screen printing. This method is still in the preliminary stage, and future independent traditional stack tests should be done. This will investigate to see if performance is at least equivalent to that obtained using CNC machined graphite plates.

Screen printing has inherent design flexibility. This allowed for the development of three new channel concepts. Testing of these new concepts to investigate improved performance at high current densities is also future work.

References

1. Amphlett, J., et al., A Model Predicting Transient Response of Proton Exchange Membrane Fuel Cells, *Journal of Power Sources* 61 (1996) pp. 183-188.
2. Amphlett, J.C. et al., Performance Modeling of the Ballard Mark IV Solid Polymer Electrolyte Fuel Cell - II. Empirical Model Development, *Journal of Electrochem. Society*, Vol 142, No. 1, January 1995.
3. Amphlett, J.C. et al., Performance Modeling of the Ballard Mark IV Solid Polymer Electrolyte Fuel Cell, *Journal of Electrochem. Society*, Vol. 142, No.1, pp. 1-6, January 1995.
4. Appleby, A.J., Foulkes, F.R., *Fuel Cell Handbook*, Krieger Publishing Company, reprint edition 1993.
5. Ballard Power Systems Inc., *Fuel Cell Operating Guidelines and Fuel Cell Performance Variables (Dow)*, 710.742.010.
6. Bernardi, D.M., and Verbrugge, M.W., A Mathematical Model of the Solid-Polymer-Electrolyte Fuel Cell, *Journal of the Electrochem. Society*, Vol. 139, No.9, September 1992, pp. 2477-2491.
7. Bernardi, D.M., Verbrugge, M.W., Mathematical Model of a Gas Diffusion Electrode Bonded to a Polymer Electrolyte, *AIChE Journal*, August 1991, Vol. 37, No.8, pp. 1151.
8. Blomen, L.J.M.J., and Mugerwa, M.N (editors), *Fuel Cell Systems*, Plenum Press, 1993, pp 358.
9. Buchi, F.N., et al., Study of Radiation-Grafted FEP-g-Polystyrene Membranes as Polymer Electrolytes in Fuel Cells, *Electrochimica Acta*, Vol. 40, No. 3, 1995, pp. 345-353.
10. Cheremisinoff, N.P., and Cheremisinoff, P.N., *Pumps / Compressors / Fans - Pocket Handbook*, Technomic, 1989.
11. Cownden, R., A Performance Model for Hydrogen Fuel Cell Power Systems for Transportation Applications - Work Term Report, NGFT, IESVic, University of Victoria, 1995.

12. Department of Energy, Fuel Cells A Handbook (Revision 3), DOE/METC-94/1006 (DE94004072), January 1994
13. Dong, Z, Invention Memo - Concept Design and Tentative Manufacturing Process of Packed Pipe Heat Exchanger (PPHE) PEM Fuel Cells, NGFT, IESVic, University of Victoria, October 5, 1995.
14. Dong, Z, Sub-Stack Design and Manufacturing/Assembly Process (Flat Panel Ambient Air Radiator Stack Fuel Cell, NGFT, IESVic, University of Victoria, March 25, 1996.
15. Doolittle, J.S., Thermodynamics for Engineers, John Wiley and Sons, Inc., 1984.
16. Fox, W.R, and McDonald, A.T. Introduction to Fluid Mechanics (Fourth Edition), John Wiley & Sons, Inc., 1992.
17. Gibb, Peter, et al., Electrochemical Fuel Cell Stack with Compression Mechanism Extending Through Interior Manifold Headers, US Patent Number 5,484,666, Ballard Power Systems, January 1996.
18. Government of Canada - Department of Energy, Mines and Resources, Fans and Pumps, Government of Canada, 1987
19. Holger, Martin, Heat Exchangers, Hemisphere Publishing Corporation, 1992.
20. Hydrogen and Fuel Cell Letter : The Energy Alternative - Renewable Fuels, October 1995, Vol. X, No. 10, ISSN 1080-8019.
21. Kahac, S., Ramesh, K.S., and Aung, W., Handbook of Single-Phase Convective Heat Transfer, John Wiley and Sons, Inc., 1987.
22. Kim, J., Lee, S., and Srinivasan, S., Modeling of Proton Exchange Membrane Fuel Cell Performance with an Empirical Equation, Journal of Electrochem. Society, Vol. 142, No. 8, August 1995, pp. 2670-2674.
23. Kolde, J.A., et al, Advanced Composite Polymer Electrolyte Fuel Cell Membranes, Electrochemical Society Proceeding Volume 95-23, 193-199.
24. Kordesh, K., and Simader, G., Fuel Cell Systems.
25. Li, X., Mech 590: Fuel Cells - Course Notes, Mechanical Engineering, University of Victoria, January 1996.

26. Marr, C., Performance Modelling of a Proton Exchange Membrane Fuel Cell, M.A.Sc. Thesis, University of Victoria, Victoria, BC 1996.
27. McKetta, J.J. (editor), Heat Transfer Design Methods, Marcel Dekker, Inc., 1988.
28. Metals Handbook, Ninth Edition - Volume 3: Properties and Selection of Stainless Steels, Tool Materials and Special Purpose Metals.
29. Method and Apparatus for Removing Water from Electrochemical Fuel Cells, Ballard Power Systems, U.S. Patent 5,260,143, November 9, 1993.
30. Moran, M.J., Fundamentals of Engineering Thermodynamics, John Wiley and Sons, Inc., 1988.
31. Mulder, M., Basic Principles of Membrane Technology, Kluwer Academic Publishers, Norwell, MA, 1991.
32. Nahon, M., and Pasquill, D., Feasibility Analysis of a Fuel Cell Test Platform, NGFT, IESVic, University of Victoria, December 1995.
33. Nguyen, T.V., White, R.E., A Water and Heat Management Model for Proton-Exchange-Membrane Fuel Cells, Journal of the Electrochem. Society, Vol. 140, No. 8, August 1993, pp. 2178-2186.
34. Okada, T., et al, Membrane Characteristics and Water Management in Polymer Electrolyte Fuel Cells, Proceedings of the 2nd Annual International Fuel Cell Conference, Kobe, Japan, 1996, pp. 339.
35. Ozisik, M.N., Heat Transfer - A Basic Approach, McGraw-Hill, 1985, pp. 388-390.
36. Pastula, M. E., Tube Bundle Heat Exchanger PEM Fuel Cell - Design Calculations 1, NGFT, IESVic, University of Victoria, December 1995.
37. Pastula, M. E., Tube Bundle Heat Exchanger PEM Fuel Cell - Design Calculations 2, NGFT, IESVic, University of Victoria, December 1995.
38. Pastula, M.E., Dimensioning for TERS8 - Tri-Stream Externally Manifolded Radiator Stack (8 Cell Prototype), NGFT, IESVic, University of Victoria, 1996.
39. Pastula, M.E., Tube Bundle Heat Exchange PEM Fuel Cell - Preliminary Calculations", IESVic, University of Victoria, November 27, 1995.
40. Pastula, M.E., Bi-Polar Plate Design Tool for Fuel Cells, IESVic - University of Victoria, August 1996.

41. Perry, Martin, Screen Printing of Hydrogen and Oxidant Delivery Plates for PEM Fuel Cells - A Low Cost Manufacturing Alternative, M.A. Sc. Thesis, Department of Mechanical Engineering, University of Victoria, June 1997.
42. Personal Communication with Joel Ronne, NGFT, IESVic, University of Victoria, February 1996.
43. Personal Communications with Henry Voss, Ballard Power Systems, April 1996.
44. Personal Communications with Keith Prater, Ballard Power Systems, 1996.
45. Personal Communications with Ken Kratschmar, NGFT, IESVic, University of Victoria, 1997.
46. Personal Communications with Simon Fraser University NGFT Group (Steve Holdcroft), IESVic, August 13, 1996
47. Pow, R., Reindl, M., and Tillmetz, W., High Power Density Fuel Cell Stack Development For Automobile Applications, Fuel Cell Seminar 1996, pp. 276-280.
48. Prater, K., Solid Polymer Fuel Cells for Transport and Stationary Applications, Journal of Power Sources, (61), pp. 105-109, 1996.
49. Prater, K.B., Solid Polymer Fuel Cell Developments at Ballard, Journal of Power Sources, 37 (1992) 181-188.
50. Reid, C., Flow Field Design and Stack Dimensioning - A Review For Novel Prototype Design, NGFT, IESVic, University of Victoria, July 10, 1997.
51. Rho, Y.W., et al., Mass Transport Phenomena in Proton Exchange Membrane Fuel Cells using O₂/He, O₂/Ar, and O₂/N₂ Mixtures, Journal of Electrochem. Society, Vol. 141, No. 8, August 1994, pp. 2084-2088.
52. Ronne, J, and Podhorodeski, R., An Integrated Cost Performance Model of a Transportation Fuel Cell System, NGFT, IESVic, University of Victoria, March 1995.
53. Ronne, J., Cost Reductions of Bi-Polar Plates for SPFCs", NGFT, IESVic, University of Victoria, 1995.
54. Sakai, T.S., et al., Gas Diffusion in the Dried and Hydrated Nafions, Journal of Electrochem. Society, pp. 88-95, January 1986.
55. Schmidt, E. (translated by J. Kestin), Thermodynamics, Dover Publishing, 1966.

56. Simader, G., Influence of Temperature and Pressure to RSS, NGFT, IESVic, University of Victoria, June 1996.
57. Singh, D., Lu, D.M., Djilali, N., Two-Dimensional Modeling of Mass Transport in Proton Exchange Membrane Fuel Cells, NGFT, IESVic, University of Victoria, January 9, 1996.
58. Smith, W.F, Principles of Materials Science and Engineering, McGraw-Hill, 1990.
59. Springer, T.E., et al., Polymer Electrolyte Fuel Cell Model, Journal of Electrochem. Society, Vol. 138, No. 8, August 1991, pp. 234-2342.
60. Tachtler, J., and Bourne, Carl, Fuel Cell Systems for Passenger Cars - Opportunities and Requirements, Proceedings of Fuel Cell Seminar 1994.
61. Task Force on Cleaner Vehicles and Fuels - Report to Canadian Council of Ministers of the Environment, October 1995.
62. Teachman, M., A Techno-Economic Comparison of Spark Ignition Engine Versus Solid Polymer Fuel Cell Power Systems for Utility Vehicles, M.A.Sc. Thesis, Department of Mechanical Engineering, University of Victoria, 1992.
63. Ticianelli, E.A., Derouin, C.R., Redondo, A., Srinivasan, S., Methods to Advance Technology of Proton Exchange Membrane Fuel Cells, Journal of Electrochem. Society, Vol. 135, No. 9, September 1988.
64. Tsou, Y., Hydrogen Diffusion, Solubility, and Water Uptake in Dow's Short-Side-Chain Perfluorocarbon Membrane, Journal of Electrochem. Soc., Vol. 139, No. 7, July 1992, pp. 1913-1917.
65. Vanderborgh, N. E., Kimble, M.C., Huff J.R., and Hedstrom, J.C., PEM Fuel Cell Stack Heat and Mass Management, Proceedings at the 27th Intersociety Energy Conversion Engineering Conference, Volume 3, p. 3.407-3.411, 1992.
66. Verbrugge, M.W., and Hill, R.F., Analysis of Promising Perfluorosulfonic Acid Membranes for Fuel-Cell Electrolytes, Journal of the Electrochem. Soc., Vol. 137, No.12, December 1990, pp. 2209.
67. Voss, H. et al., Coolant Flow Field Plate for Electrochemical Fuel Cells, Ballard Power Systems, U.S. Patent 5,230,966, July 27, 1993.
68. Voss, H. et al., Method and Apparatus for Removing Water from Electrochemical Fuel Cells, Ballard Power Systems, U.S. Patent 5,260,143, November 9, 1993.

69. Voss, H., et al., Anode Water Removal: A Water Management And Diagnostic Technique for Solid Polymer Fuel Cells, *Electrochimica Acta*, Volume 40, No. 3, 1995, pp. 321-328.
70. Voss, H., et al., Method and Apparatus for Removing Water from Electrochemical Fuel Cells by Controlling the Temperature and Pressure of the Reactant Streams, Ballard Power Systems, U.S. Patent 5,441,819, August 15, 1996.
71. Wakizoe, M. et al., Analysis of Proton Exchange Membrane Fuel Cell Performance with Alternative Membranes, *Electrochimica Acta*, Vol. 40 No. 3, 1995, pp. 335-344
72. Wakizoe, M., et al., Fundamental Study of Asahi Chemical Aciplex(-S Membrane for Polymer Electrolyte Fuel Cell (PEFC), Proceedings of the 2nd Annual International Fuel Cell Conference, Kobe, Japan, 1996, pp. 331.
73. Walker, G., *Industrial Heat Exchangers - A Basic Guide (2nd Edition)*, Hemisphere Publishing Corporation, 1990.
74. Washington, K.B., et al., Laminated Fluid Flow Field Assembly for Electrochemical Fuel Cells, Ballard Power Systems, U.S. Patent 5,300,370, April 5, 1994.
75. Watkins, D.S., et al., Fuel Cell Fluid Flow Field Plate, Ballard Power Systems, U.S. Patent 5,108,849, April 28, 1992.
76. Watkins, D.S., et al., Novel Fuel Cell Fluid Flow Field Plate, Ballard Power Systems, U.S. Patent 4,988,583, January 29, 1991.
77. Wilkinson, D.P., et al., Method of Fabricating an Embossed Fluid Flow Field Plate, Ballard Power Systems, U.S. Patent 5,527,363, June 18, 1996.
78. World Highways/Routes Du Monde, September 1996, pp.22
79. Xue, D., and Dong, Z., Optimal Fuel Cell System Design Considering Functional Performance and Production Costs, Proceedings of DETC'97, 1997 ASME Design Engineering Technical Conferences, Sacramento, California, September 1997.
80. Zawodzinski, T.A., et al., The Water Content Dependence of Electro-Osmotic Drag in Proton-Conducting Polymer Electrolytes, *Electrochimica Acta*, Vol. 40, No. 3, 1995, pp. 297-302.

VITA

Surname: Pastula

Given Names: Michael Edward

Place of Birth: Duncan, British Columbia, Canada

Educational Institutions Attended:

University of Victoria

1996 to 1998

University of Victoria

1990 to 1995

Degrees Awarded:

B. Eng (First Class) University of Victoria

1995

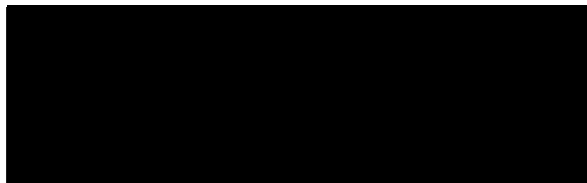
PARTIAL COPYRIGHT LICENSE

I hereby grant the right to lend my thesis to users of the University of Victoria Library, and to make single copies only for such users or in response to a request from the Library of any other university, or similar institution, on its behalf or for one of its users. I further agree that permission for extensive copying of this thesis for scholarly purposes may be granted by me or a member of the university designated by me. It is understood that copying or publication of this thesis for financial gain shall not be allowed without my written permission.

Title of Thesis:

Radiator Stack PEM Fuel Cell Architecture, System Modeling and Flow Field Design

Author:



Michael Edward Pastula
January 14, 1998